Simulation of rotor-stator interaction in a high-speed low-pressure turbine cascade using a high order discontinuous Galerkin method

Auteur : Thys, Mars
Promoteur(s) : Hillewaert, Koen
Faculté : Faculté des Sciences appliquées
Diplôme : Master en ingénieur civil physicien, à finalité approfondie
Année académique : 2023-2024
URI/URL : http://hdl.handle.net/2268.2/21088

UNIVERSITY OF LIÈGE - FACULTY OF APPLIED SCIENCES

SIMULATION OF ROTOR-STATOR INTERACTION IN A HIGH-SPEED LOW-PRESSURE TURBINE CASCADE USING A HIGH ORDER DISCONTINUOUS GALERKIN METHOD

MASTER THESIS PRESENTED BY
MARS THYS
IN PARTIAL FULFILLMENT OF THE REQUIREMENTS FOR THE DEGREE OF MASTER OF SCIENCE IN PHYSICS ENGINEERING

THESIS SUPERVISORS
ACADEMIC: PR. KOEN HILLEWAERT
INTERNSHIP: DR. MICHEL RASQUIN

JURY MEMBERS
PR. KOEN HILLEWAERT
DR. MICHEL RASQUIN
PR. SERGIO LAVAGNOLY
PR. VINCENT TERRAPON

LIÈGE, ACADEMIC YEAR 2023-2024

Abstract

Numerical simulation of the air flow in a high-speed low-pressure turbine using a high order discontinuous Galerkin method. The computational domain as well as the flow conditions are based on the SPLEEN experimental campaign conducted at the von Karman institute. The setup is compose of a wake generator upstream of a linear blade cascade. In the numerical simulation, the wake generator is represented by a translating cylinder while the blade cascade is static. with moving wake generators upstream. The flow around the blade is therefore influenced by the incoming wakes and the blade loading are modified as well as the turbomachinery loss. Quantitatively, the present report gives results made on averages for the wake generator part. For the blade cascade part, a quantitative discussion is made, with the illustrative support of multiple self-made pictures.

Acknowledgement

I would like to thanks my advisor Professor Koen Hillewaert for willingly sharing his knowledge with passion.

I would like to express my sincere thanks to Michel as well as Margaux, research engineers at Cenaero, for their presence and support throughout this work.

Finally, I would like to thanks my family and my friends for their encouragements and unconditional support.

A special thanks to Mayana for her thoughtful proofreading and her support throughout this year.

The present research benefited from computational resources made available on Lucia, the Tier-1 supercomputer of the Walloon Region, infrastructure funded by the Walloon Region under the grant agreement n°1910247.

Contents

1 Introduction

1.1 Context and motivation

Aircraft engines efficiency has improved a lot since their invention in the 1930s. Today, the aircraft engines thermodynamic efficiency has reach a peak. The only remaining room for improvement concerns the propulsive efficiency which can be achieved by increasing the bypass ratio [1].
However, enlarging the fan to increase the bypass ratio leads to faster rotating speed of the fan blades tip. This results in transonic flows with undesirable compressibility effects.
The solution to this problem has been introduced by Pratt & Whitney in 2008 with the geared turbofan, see Fig. 1.1.

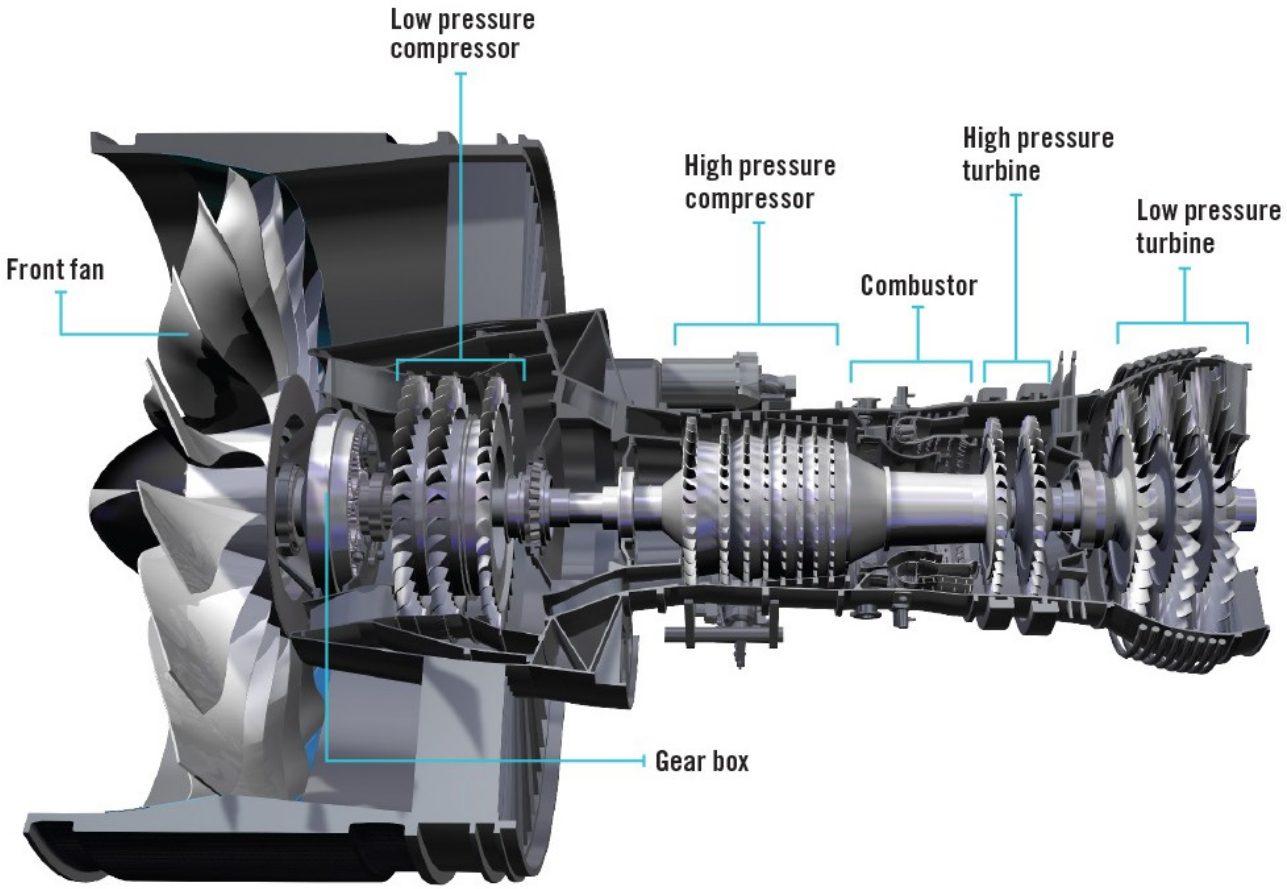

Figure 1.1: Pratt and Whitney's geared turbofan jet engine, taken from [2].

The idea of decoupling the fan from the shaft of the compressors and turbines using a planetary gearbox allows each part to rotate at its optimal speed: slower for the fan and faster for the compressors and turbines. In addition to the gain in bypass ratio, the higher rotating speed of the compressors and turbines allows to reduce the number of stages for each components, greatly reducing the engine weight. The stages reduction can be seen between Pratt and Whitney's geared turbofan in Fig. 1.1 and General Electric's turbofan engine without gearbox in Fig. 1.2.

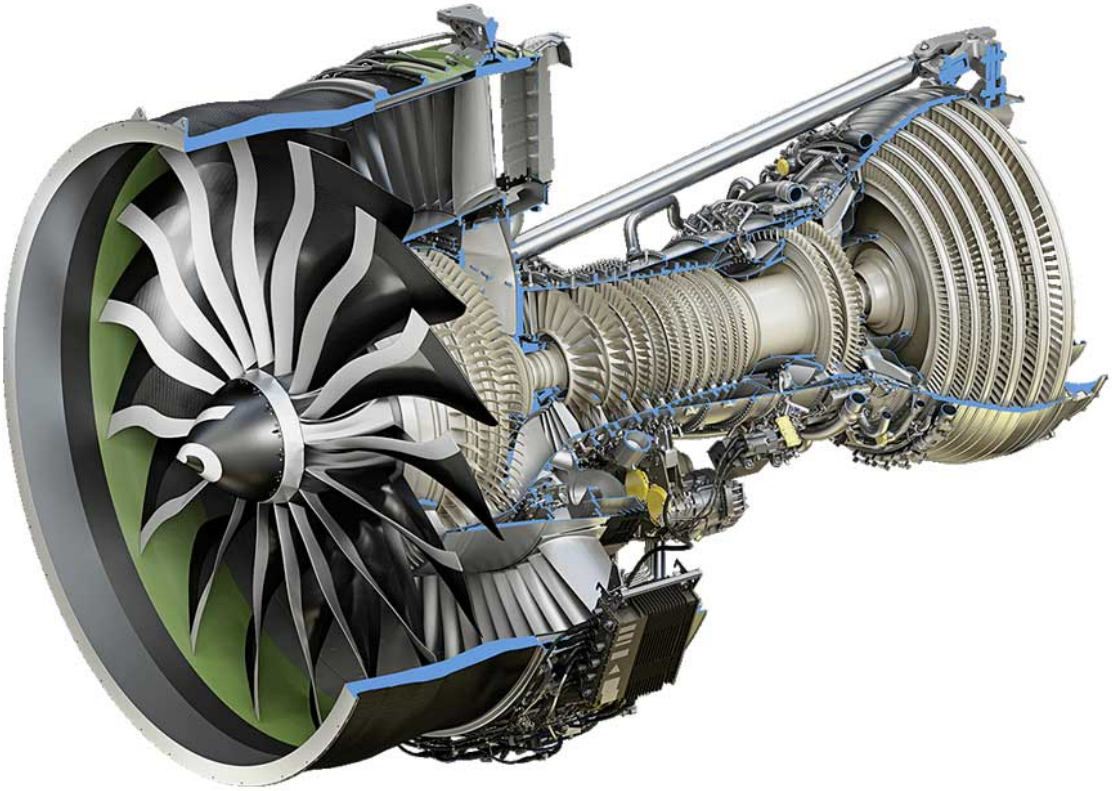

Figure 1.2: General Electric GE9X high-bypass turbofan without gear box, taken from [3].

The subject of this thesis is about the last part of the geared turbofan engine, the low-pressure turbine (LPT), which is now rotating at higher speed. In such high-speed LPT, the flow is transonic with important compressibility effects and laminar and turbulent coexisting structures. On the suction side in particular, the flow characteristics such as separation and laminar-turbulent transition are decisive for LPT efficiency [4]. One way to prevent separation is to use the rotor-stator interaction which is the interaction of upstage blade wake with the boundary layer of the down stage blade. This wake boundary layer interaction leads to early transition to turbulence which can improve LPT efficiency.
Multiple experimental and numerical studies of wake interaction in LPT can be found in the literature such as [5] and [6]. Hodson in particular, is one of the pioneers with numerous papers on the subject, see [7], [8], [9], [10] among others. The flow conditions or computational models vary from one study to the other offering a large panel of databases. In the experimental campaigns for example, tests have been conducted with different systems to generate the wake, using either transversely moving bars see [9] and [11], or rotating bars see [12]. In numerical studies, using different approaches such as RANS [13], LES [14], [15], [16], spectral/hp element methods [17].

The present work is part of this series of numerical studies on wake interaction in LPT. Its innovative aspect is the use of a high-order discontinuous Galerkin method (DGM) to solve the Navier-Stokes equations. This work is based on the recent experimental campaign conducted in the framework of the SPLEEN project at the von Karman Institute [12]. SPLEEN stands for Secondary and Leakage Flow Effects in High-SPeed Low-PrEssurE TurbiNes. It is funded by the European Union's Horizon 2020 research and innovation program.

The experimental SPLEEN project is already the subject of several numerical studies such as Borbouse using

high-order DGM [18] for the case without wake generator and Dombard [16] using FVM-LES for the case with wake generator. As the present work also concerns the numerical simulation of the SPLEEN project with wake generator, a brief comparison is made with Dombard's results in section 6.3.

1.2 Methodology and overview

In the SPLEEN project, the incoming wakes from the upstream rotor part of the turbine are produced from a so-called *wake generator*. This wake generator is composed of 96 bars, rotating at 3300 RPM. Behind those bars, the next turbine stage is composed of a *linear cascade* of 23 static blades.
To reproduce this experimental setup, the numerical simulation is divided into two domains:

- The **wake generator** domain composed of only one cylinder, translating at the same peripheral velocity than the rotating bars.
- The **blade cascade** domain composed of only one static blade.

The numerical solution is first initialized on each domain separately. Then, the two domains are coupled. This method allows to initialize the blade cascade domain from the solution obtained by Borbouse [18] without the wake generator. As no solution exists for the wake generator, its initialization is done in this work.

The actual flow simulation is carried out using the software *ArgoDG* developed at the research center *Cenaero*. The parallel computations are performed using the supercomputer of the Walloon Region *Lucia*.

The general structure of this thesis consists in seven chapters:

- The theoretical background providing details about the considered flow. Additional theoretical concepts are described about the numerical tools used to simulate the flow.
- The experimental environment of the SPLEEN project, with the geometry parameters and operating conditions that will serve as the basis for the numerical simulation.
- The numerical environment with the numerical tools used and the definition of the computational domain and boundary conditions.
- The transient solutions of the wake generator and the coupling with the blade cascade.
- The analysis and discussion of the results.

2 Theoretical background

In this chapter, the key ideas and concepts addressed in this work are presented. They are arranged into two categories; the physics and the numerics.
The physics section gathers various phenomena that appear in a high-speed low-pressure turbine such as laminar-turbulent transition, losses and wake boundary layer interaction. An other section about the characteristics of the flow around a circular cylinder is also presented to have more insights about the physics of the wake generator.
The section about the numerics presents the general ideas at the core of computational fluid dynamics such as the Navier-Stokes equations, the spatial and temporal discretizations and the solving of the resulting system of non-linear equations. In particular, the discontinuous Galerkin method is briefly introduced with additional concepts such as the Riemann problem and Newton-GMRES solving method for a better understanding of some issues encountered during this work.

2.1 Physics

In the operating conditions of a high-speed low-pressure turbine (LPT), the flow is transonic with important compressibility effects and laminar and turbulent coexisting structures. LPT efficiency greatly depends on the characteristics of the flow, in particular along the suction side of the blades where unsteadiness, laminar-turbulent transitions and shock waves are determinant.

2.1.1 Operating conditions

The operating flow conditions in turbomachinery are usually defined using isentropic flow equations, as done in the experimental campaign [19]. In particular, the isentropic outlet Mach and Reynolds numbers are used to describe those operating conditions and the importance of compressibility and turbulence effects respectively. The expression of the outlet isentropic Mach number follows:

$$M_{\text{is,out}} = \sqrt{\frac{2}{\gamma-1}\left[\left(\frac{p_{0,\text{in}}}{p_{\text{out}}}\right)^{\frac{\gamma-1}{\gamma}} - 1\right]}, \tag{2.1}$$

with $p_{0,\text{in}}$ [Pa] the inlet total pressure, p_{out} [Pa] the outlet static pressure and γ [-] the heat capacity ratio.
The expression of the outlet isentropic Reynolds number follows:

$$\text{Re}_{\text{is,out}} = \frac{\rho_{\text{is,out}} U_{\text{is,out}} c}{\mu(T_{\text{out}})}, \tag{2.2}$$

with c the blade chord, the outlet isentropic density $\rho_{\text{is,out}}$ [kg/m^3], the outlet isentropic velocity $U_{\text{is,out}}$ [m/s] and the dynamic viscosity μ [kg/m s] The definition of those quantities follow with the outlet isentropic density (perfect gas law):

$$\rho_{\text{is,out}} = \frac{p_{\text{out}}}{R T_{\text{out}}}, \tag{2.3}$$

with R = 287.06 [J/kg K] the gas constant.
The outlet temperature follows:

$$T_{\text{out}} = T_{0,\text{in}}\left(1 + \frac{\gamma - 1}{2} M_{\text{is,out}}^2\right)^{-1}. \tag{2.4}$$

The outlet isentropic velocity follows:

$$U_{\text{is,out}} = M_{\text{is,out}} \sqrt{\gamma R T_{\text{out}}}. \tag{2.5}$$

The outlet isentropic dynamic viscosity follows Sutherland's law:

$$\mu_{\text{is,out}} = \frac{1.458 \times 10^6 T_{\text{out}}^{3/2}}{T_{\text{out}} + 110.4}. \tag{2.6}$$

2.1.2 Turbulence

A turbulent flow is characterized by chaotic changes in pressure and flow velocity and important mixing effects. In contrast, in a laminar flow, the fluid particles are very ordered.
Following the Reynolds decomposition technique, the flow can be decomposed into a main time averaged component $\bar{u}$ and a fluctuating component u'. The total flow U is expressed as:

$$U = \bar{u} + u'. \tag{2.7}$$

The level of turbulence in a flow can be viewed as the significance of the fluctuating component u'.
A more precise way to determine the level of turbulence is to introduce the Reynolds decomposition into the Navier-Stokes equations and average them to get the Reynolds averaged Navier-Stokes equations:

$$\rho \bar{u}_j \frac{\partial \bar{u}_i}{\partial x_j} = \rho \bar{f}_i + \frac{\partial}{\partial x_j}\Big[- \bar{p}\delta_{ij} + 2\mu \bar{S}_{ij} - \rho \overline{u_i' u_j'} \Big], \tag{2.8}$$

with $\bar{S}_{ij}$ the mean strain rate tensor. The term $\rho \overline{u_i' u_j'}$ is the turbulence contribution to the mean flow and is called the Reynolds stress tensor. The turbulence level of the flow can then be expressed as the variance of the Reynolds stress components which leads to the definition of the turbulent kinetic energy (TKE):

$$\text{TKE} = \frac{1}{2}\left(\overline{u'^2} + \overline{v'^2} + \overline{w'^2}\right), \tag{2.9}$$

with $\overline{u'^2}$, $\overline{v'^2}$ and $\overline{w'^2}$ the averages of the square of the velocity fluctuation in the x, y and z directions respectively.
Another important quantity in turbomachinery is the turbulent intensity of the flow (Tu) which has the following definition:

$$\text{Tu} = \frac{\sqrt{2/3\ \text{TKE}}}{U_\infty}, \tag{2.10}$$

where U_∞ is a characteristic velocity of the flow, such as the inlet or outlet, free stream or isentropic velocity. This turbulent intensity plays an important role in transition mechanisms. Those transition mechanisms from laminar to turbulent flows are now briefly introduced.

There are different paths from laminar to turbulent flows. In a boundary layer, those paths are summarized in Fig. 2.1. Those paths can be divided into two categories, the natural and by-pass transitions. In the natural transition, it starts from a small perturbation that is amplified linearly until the breakdown to turbulence. In the by-pass transition, it starts from a big perturbation that leads immediately to breakdown to turbulence.
Small or big perturbations come from the free-stream sound or turbulence, surface curvature, shape discontinuities, surface roughness, and others. That is why the determination of the turbulence intensity is

important.
As in the example of the golf ball, the transition in a boundary layer of a turbine blade is critical to its efficiency and therefore of great interest both from theoretical and practical points of view.

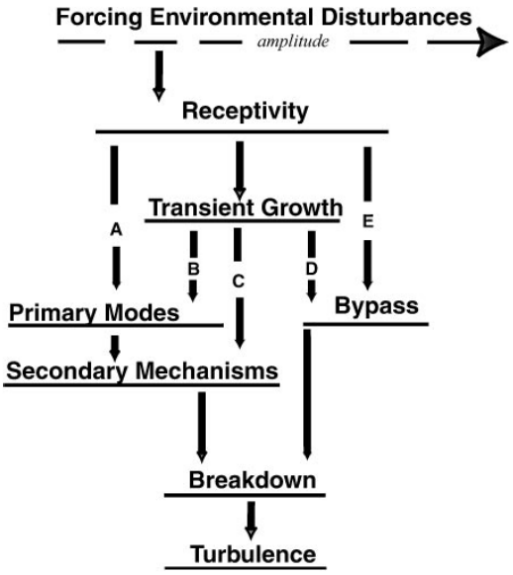

Figure 2.1: Paths to turbulence, taken from [20].

The point of separation in a boundary layer can be localized with the wall shear stress or equivalently with the skin friction coefficient. At the separation point, their values are zero.
The expression of the wall shear stress is:

$$\tau_{\mathrm{w}} = \mu \frac{\partial u}{\partial y}\Big|_{y=0}, \tag{2.11}$$

with μ [kg/m s] the fluid dynamic viscosity, u [m/s] the fluid velocity parallel to the surface and y [m] the distance from the surface. The skin friction coefficient is defined as the adimensionalized wall shear stress by the dynamic pressure:

$$c_{\mathrm{f}} = \frac{\tau_{\mathrm{w}}}{\frac{1}{2}\rho_{\infty} v_{\infty}^2}, \tag{2.12}$$

with ρ_{∞} and v_{∞} the characteristic density and velocity of the flow respectively.

2.1.3 Shock physics

A shock is an abrupt discontinuity in the flow field and occurs when the local flow speed exceeds the local sound speed, *i.e.*, when the Mach number locally exceeds 1. It is caused by the coalescence of acoustic waves that are travelling in the medium and can not progress further upstream. Those acoustic waves are pressure perturbations coming from wall interaction (a), mixing layers (b) or simply adverse pressure gradients (c) illustrated in Fig. 2.2.

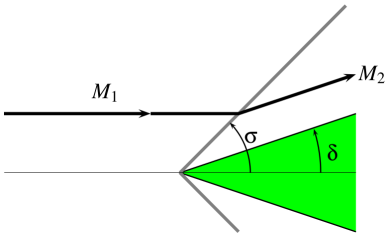

(a) Oblique shock, taken from [21].

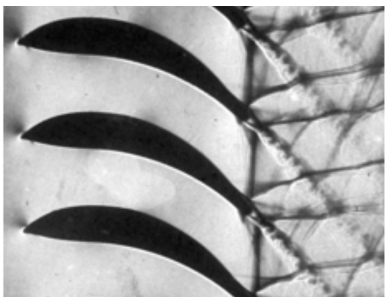

(b) Choking of a turbine cascade, taken from [22].

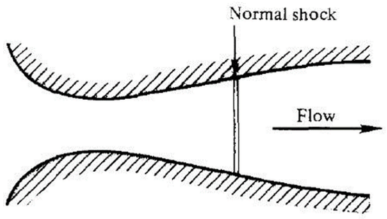

(c) Shock in a nozzle, taken from [23].

Figure 2.2: Examples of shock origins.

Flows represented by the Navier-Stokes equations have always an hyperbolic and an elliptic part, but at specific regimes, they can be simplified.
In subsonic regime in particular, the flow can be viewed as incompressible and information travels infinitely fast, forcing the flow to adapt everywhere at once (mainly elliptic). In transonic regime, compressibility effects are important and the information (acoustic waves) travels at finite speed, influencing the flow locally (mainly hyperbolic). The consequence is the presence of shocks in $M = 1$ regions where the flow adapts to boundary conditions [24] that are not felt in supersonic regions.

So, a shock is formed by the coalescence of acoustic waves. At the shock location, the acoustic waves steepen into a very thin layer as their local speed depends on the local pressure, *i.e.*, the lower pressure part moves slower than the higher pressure part, see Fig. 2.3 [25], [26], [27].

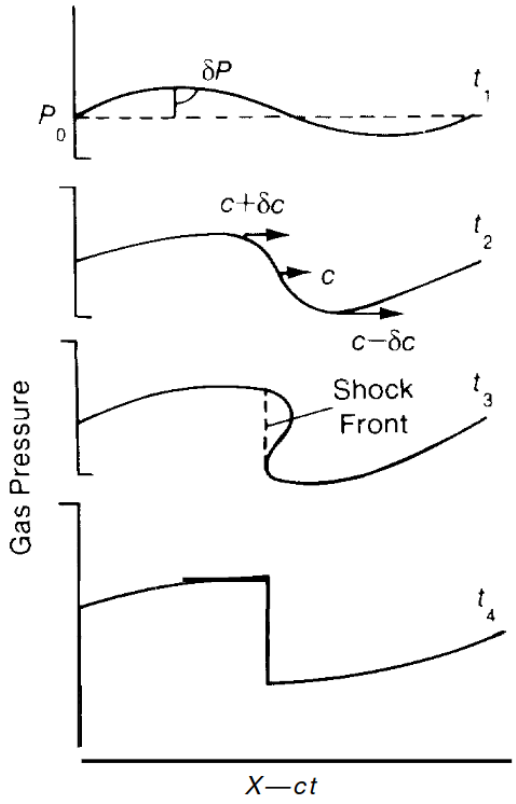

Figure 2.3: Acoustic waves non linear behaviour and steepening, taken from [25].

What is preventing the state variables to have multiple values at the same location (in t_3 in Fig. 2.3), is the increase of heat conduction and viscous stress that are dominant at the shock thickness scale. Therefore,

one can estimate the thickness of the shock δ from:

$$\mathrm{Re}_\delta = \frac{(u_1 - u_2)\delta}{\nu} \approx 1 \qquad \Rightarrow \qquad \delta \approx \frac{\nu}{u_1 - u_2}, \tag{2.13}$$

with ν the kinematic viscosity, u_1 and u_2 the flow velocity before and after the shock ($u_1 > u_2$).
As the considered fluid is air, δ scales as a few collision *mean free paths* (10^{-8} m).
Through the shock, the entropy increases, inducing a loss in total pressure [28], [29]. Because of that total pressure changes across the shock, Bernoulli's equation across the shock can not be used. However, conservation laws still apply and lead to the well known Ranckine-Hugoniot relations [24], [30] [30], [24].

2.1.4 Flow around a circular cylinder

The first part of the problem considered here is about the upstream wake generators, i.e. the rotating bars. Those bars can be viewed as perfect circular cylinders with a diameter of 1 mm, moving at a vertical speed of about 166 m/s. As the inlet flow comes at about 150 m/s with an angle of 42.47°, the relative velocity of the flow with respect to the bars is roughly 290 m/s. With the acceleration of the flow around the bar, the velocity exceeds locally the speed of sound and compressibility effects take place.
The present section describes the physics of the flow around a circular cylinder, with a particular interest to the flow regime concerned here.

Related dimensionless numbers

The Reynolds number Re_D defined in Eq. (2.14) describes the ratio of inertial forces to viscous forces. It is used to differentiate between the flow regimes: laminar, transitional or turbulent.

$$\mathrm{Re}_D = \frac{u_\infty D}{\nu_\infty} = \frac{\rho_\infty u_\infty D}{\mu_\infty}. \tag{2.14}$$

u_∞ is the flow velocity with ∞ specifying that it is a free-stream variable. D is the cylinder diameter and ν_∞ the kinematic viscosity that can be expressed as the ratio of the dynamic viscosity μ_∞ and the density ρ_∞.

The Mach number M_∞ defined in Eq. (2.15) is the ratio between the free-stream velocity and the speed of sound a_∞.

$$\mathrm{M}_\infty = \frac{u_\infty}{a_\infty}. \tag{2.15}$$

The flow is called subsonic if M < 1 and supersonic if M > 1. Transsonic flows have regions of both types, subsonic and supersonic.

The Strouhal number Str defined in Eq. (2.16) describes periodically oscillating flow phenomena with f the frequency of oscillations. Here, f is the frequency at which the vortices are ejected in the wake of the cylinder.

$$\mathrm{Str} = \frac{fD}{u_\infty}. \tag{2.16}$$

Multiple studies have shown a relationship between the Strouhal number and the Reynolds number, see Fig. 2.4. This relationship allows to estimate the wake vortex shedding frequency from Re_D.

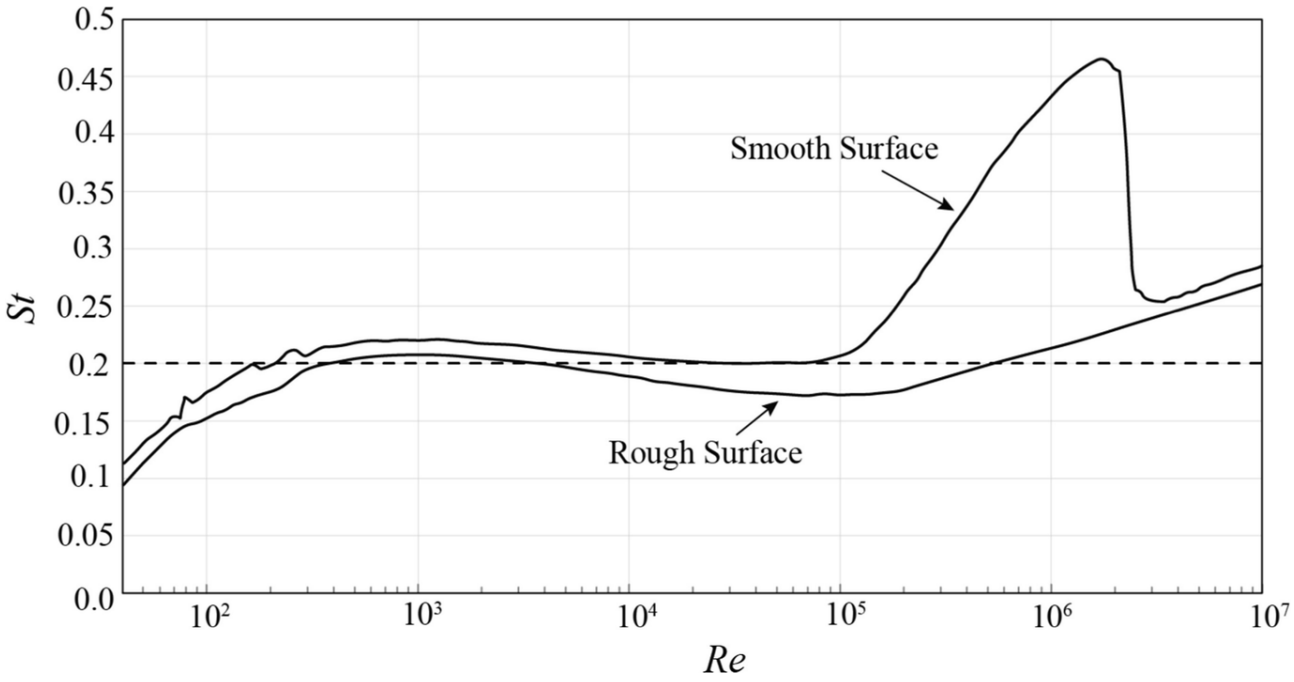

Figure 2.4: Relationship between Strouhal number and Reynolds number for circular cylinders, taken from [31], reproduced from Lienhard (1966).

Separation and vortex shedding

The path of a fluid particle in the flow around a circular cylinder can be decomposed into five steps, see Fig. 2.5. First the particle is stopped at the stagnation point. In this region, the pressure is high and the particle accelerates while going around the cylinder inside the boundary layer. At the separation point, the adverse pressure gradient is too strong and the particle stops following the cylinder surface. An low pressure zone forms behind the cylinder. Then, a small downstream perturbation is enough to start the wake oscillation, forming the well known Karman vortex street whose frequency can be obtained from Eq. (2.16).
In the present case, $\mathrm{Re}_D \approx 2000$ and $\mathrm{M} \approx 0.8$. The corresponding wake vortex shedding frequency is 60900 Hz which corresponds to a period of 1.64e-5s.

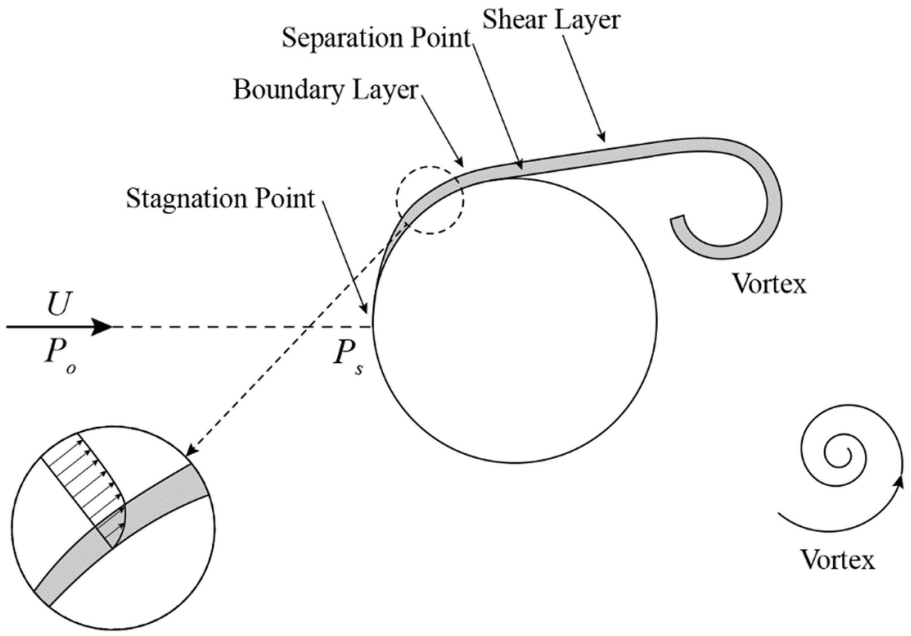

Figure 2.5: Separation and vortex shedding around a circular cylinder, taken from [31].

Flow regime identification and wake behaviour

In Hoffmann and Weiss [32], eight flow regimes are identified, with increasing Re_D and M numbers, gathered in Table 2.1.

Regime	Re_D	M
Steady symmetric separation	50	0.6
Unstable wake, onset of Karman vortex street	50	0.4
Pure Karman vortex street	100	0.4
Unstable Karman vortex street	300	0.6
Lambda shock formation and unstable wake	300	0.8
Lambda shock and unstable wake	53400	0.8
Detached shock and unstable wake	100	1.2
Detached shock and steady wake	26700	1.2

Table 2.1: Flow regimes around a circular cylinder, from [32].

In the present case, $\mathrm{Re}_D \approx 2000$ and $\mathrm{M} \approx 0.8$. The corresponding flow regime is between the "Lambda shock formation and unstable wake" and the "Lambda shock and unstable wake" regimes. Fig. 2.6 shows the shape of the flow corresponding to this regime.

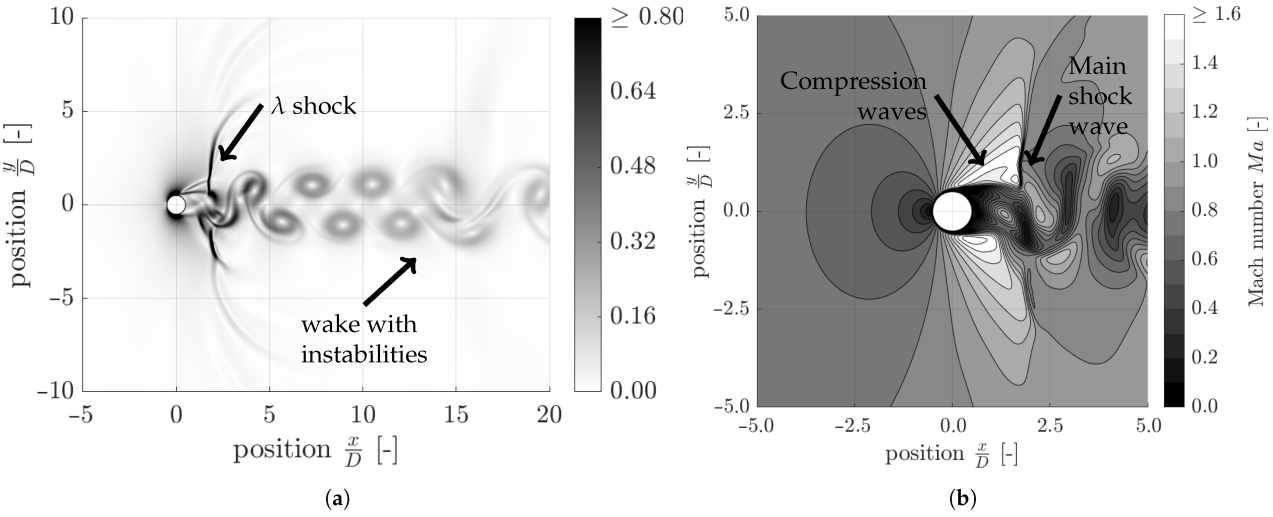

Figure 2.6: Lambda shock formation and unstable wake regime, taken from [32].

As introduced in the previous subsection, starting from the free-stream the flow is first stopped at the stagnation point, and then accelerated upon and below the x axis while going around the cylinder. In the present transonic flow conditions, the acceleration of the flow leads to a lambda shock on both side of the wake. Those lambda shocks consist in compression waves and a main shock wave, see the right figure in Fig. 2.6. The lambda shocks interact with the flow separation.

2.1.5 Losses in low-pressure-turbine

Following Denton [33], losses in low-pressure turbines can be estimated from the entropy increase. In general, entropy comes from viscous effects in boundary layers and mixing processes, shock waves and heat transfer. Neglecting secondary flows, those entropy sources can be linked to four main components of varying importance: the suction side, pressure side, mixing and base flow, see diagram in Fig. 2.7.

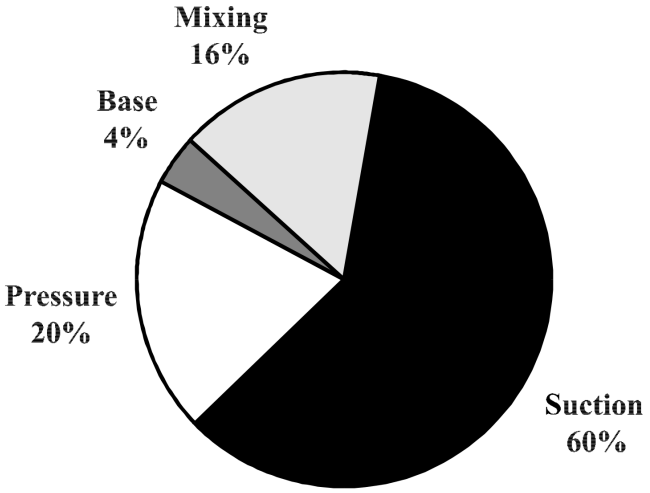

Figure 2.7: Breakdown of the estimated losses on a blade, taken from [4].

As the largest losses arise from the suction side, improving the suction surface flow could lead to significant efficiency increase.
In LPT in general, the flow remains laminar on most of the suction side, then undergoes a transition via a laminar separation bubble. The wake coming from the previous turbine stage can affect this transition process by introducing unsteadiness and turbulence. This wake interaction with the blade boundary layer can be beneficial in certain situations. Fig. 2.8 illustrates the potential benefits of turbulence (higher Reynolds number).

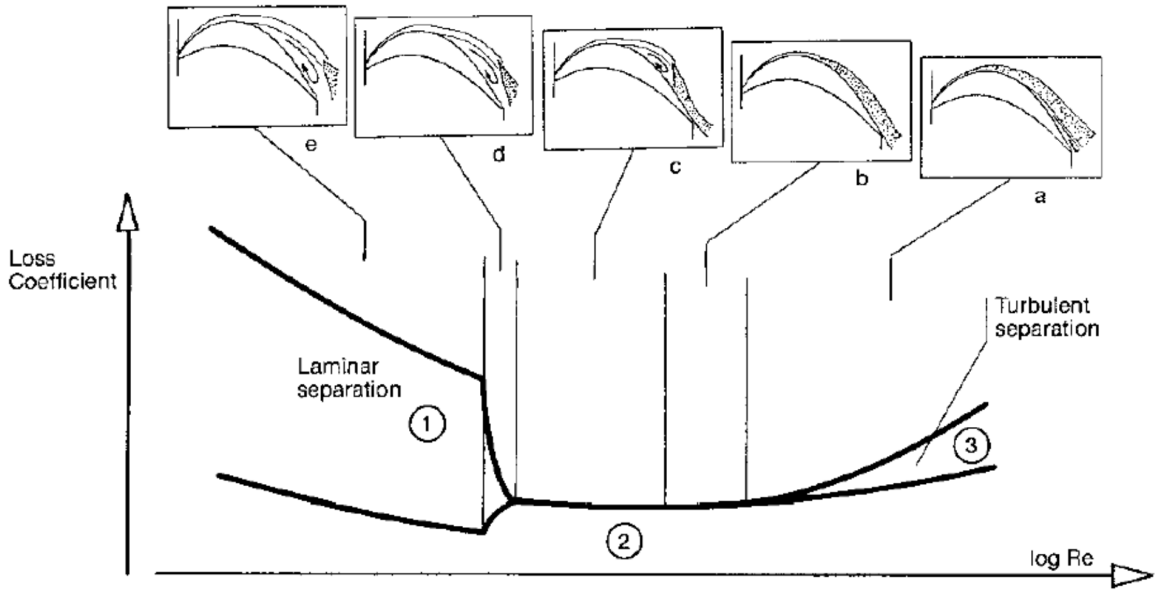

Figure 2.8: Variation of the flow structure on the suction side with related loss coefficient as a function of the Reynolds number, taken from [34].

2.1.6 Wake boundary layer interaction

As stated in the introduction context in section 1.1, various studies exist on the rotor-stator interaction with the upstream wake generated by moving bars. So far, only the setup with the translating bars has been studied, by Hodson and Howell in [9] and [4] and Li Xuejian et al. in [11]. These experimental setups are shown in Fig. 2.9.

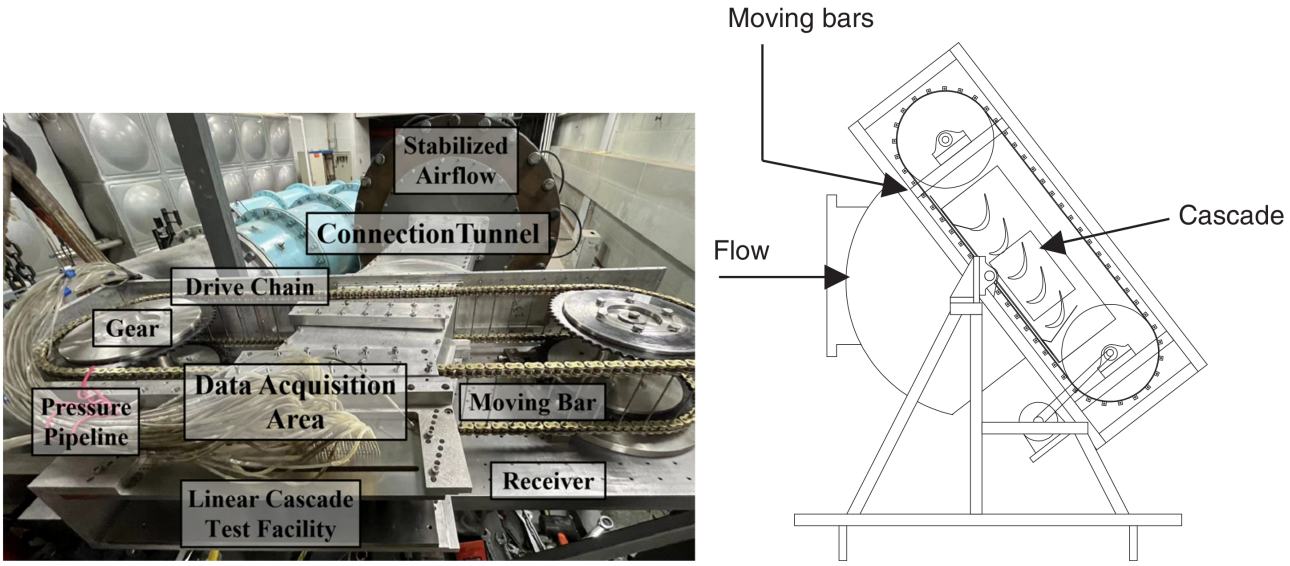

(a) Li Xuejian et al. setup, taken from [11].

(b) Stieger and Hodson setup, taken from [9].

Figure 2.9: Experimental setups with the moving bar rig.

Li Xuejian et al in [11] performed an experimental study but also a numerical simulation of the influence of the wake periodic passages on the blade efficiency with various incidence angles from −50° to 20°. In this study, the wake interaction with the blade boundary layer induced almost no losses for negative incidence angles, but high losses for positive incidence angles. It mainly shown that the wake passage had a great impact on the blade performances in particular in positive incidence angles where it is detrimental.
In Hodson and Howell [9] and Stieger and Hodson [35], the interaction of the wake with the blade boundary layer is described in more details. Fig. 2.10 shows the negative jet model used to simulate the wake. It offers a view of the passage of the wake trough the blade cascade.

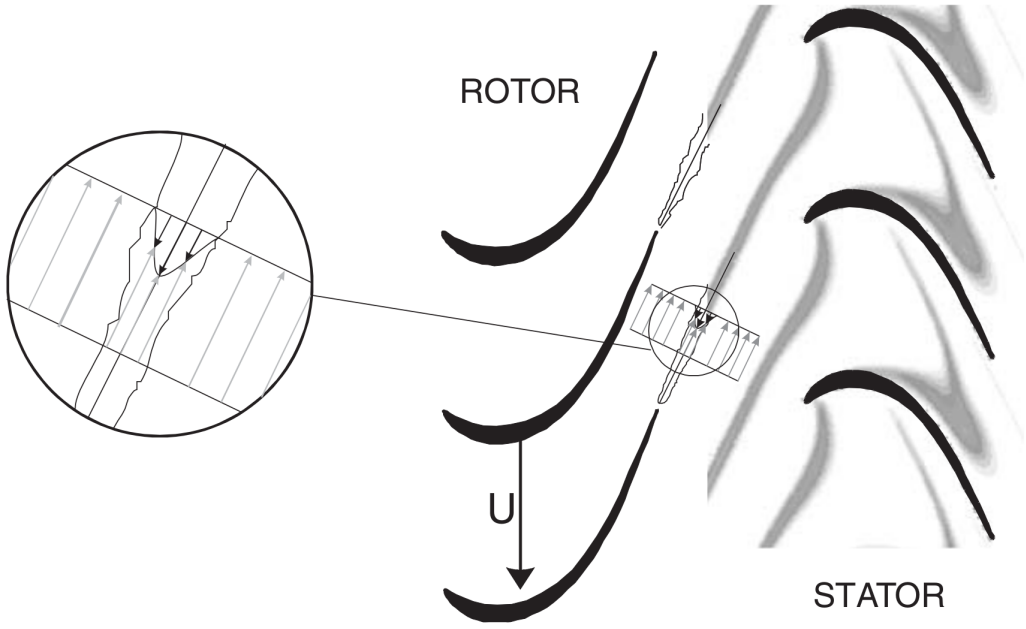

Figure 2.10: Schematic of the wake-blade interaction in high-lift LPT, taken from [9].

The laminar-turbulent transition induced by the passage of the wake is so localized that it is called *wake induced transition*. Multiple mechanisms take place in this wake induced transition. In the case of attached flow, the incoming wakes induce turbulence through by-pass transition mechanism. In the case of separated flow, the incoming wakes induce turbulence by amplification of the Kelvin–Helmholtz instability. In

particular, this local wake induced transition moves with the passage of the wake on the blade surface, see Fig. 2.11.

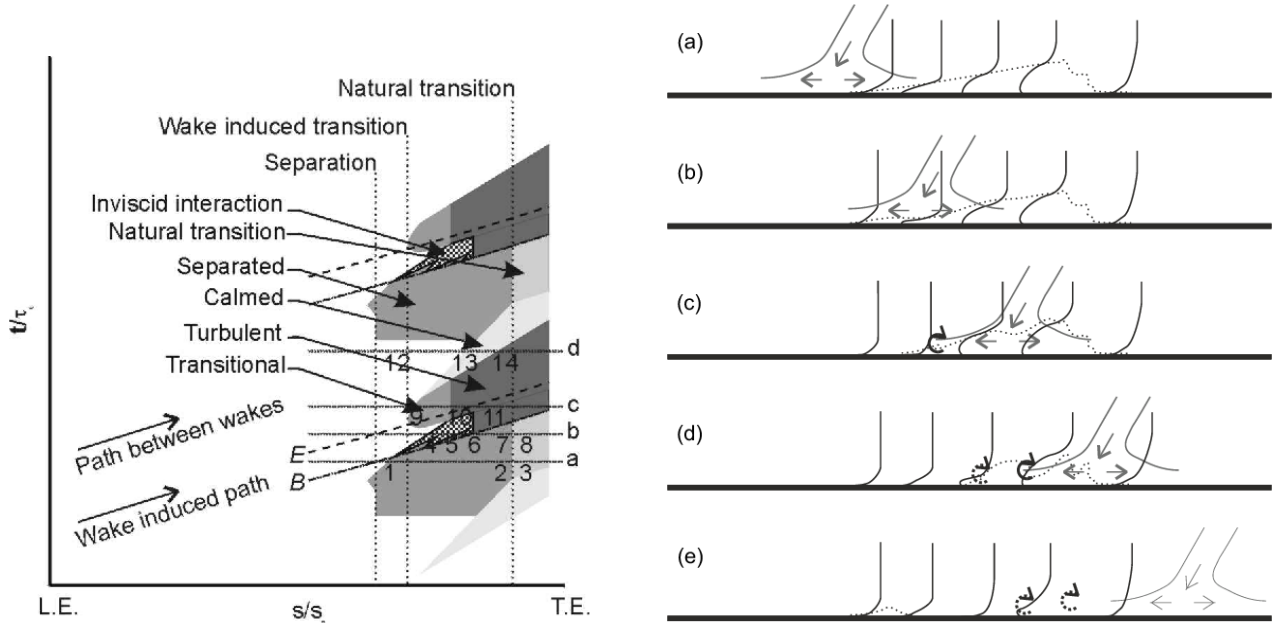

(a) Space-time sketch of the wake induced transition, taken from [35].

(b) Sketch of the passage of the wake on the blade suction side, taken from [35].

Figure 2.11: Experimental setups with the moving bar rig.

The distinction between the cases of wake interaction on attached flow and separated flow are shown in Fig. 2.12.

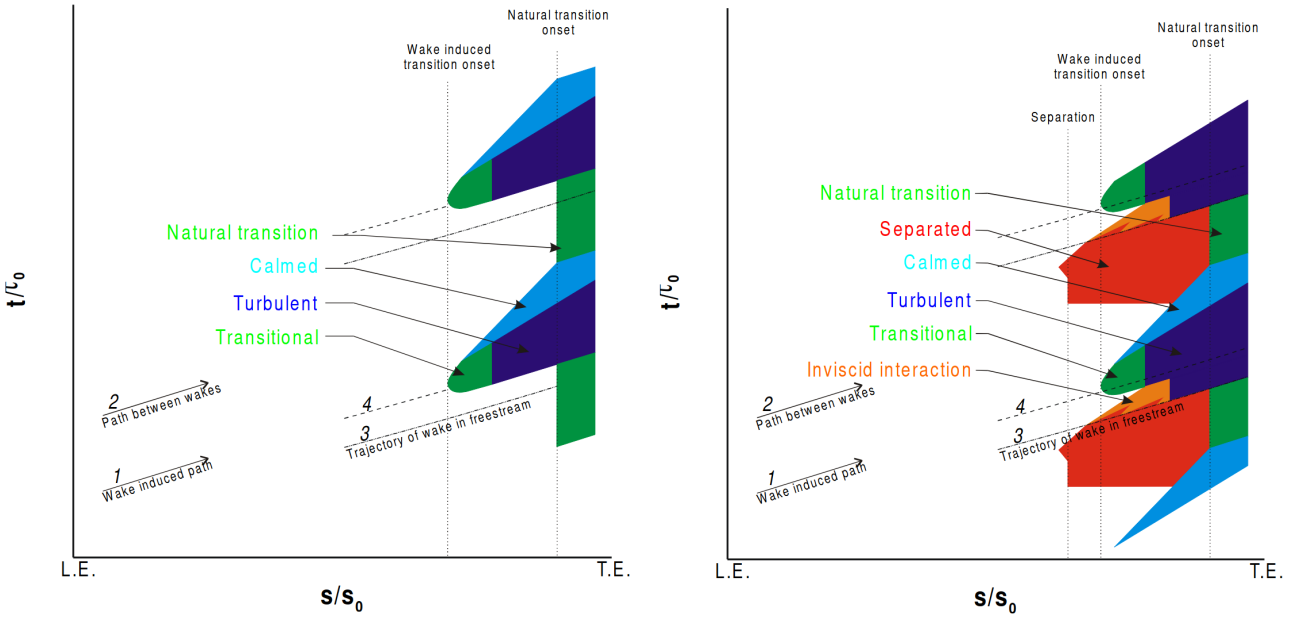

(a) Attached flow case.

(b) Separated flow case.

Figure 2.12: Space-time sketches of the wake induced transition, taken from [35].

2.2 Numerics

The aim of this work is to give a numerical approximation of the physics described in section 2.1, in the context of a high-speed low-pressure turbine cascade.
The numerical approximation of such flow physics can be summarized in 4 steps:

- **Navier-Stokes equations** describe the motion of viscous fluids analytically.
- **Spatial discretisation** of those nonlinear partial differential equations (DGM).
- **Temporal discretisation** of the system using implicit time integration schemes (BDF2).
- **Solving** the resulting nonlinear systems of equations (Newton-GMRES).

Those four steps are briefly described in the next subsections, with the methods and solvers used in this work.

2.2.1 Navier-Stokes equations

The Navier-Stokes equations (NSE) describe analytically the motion of viscous fluids through mass, momentum and energy conservation laws, see equations (2.17), (2.18) and (2.19) respectively:

$$\vec{\nabla} \cdot (\rho \vec{u}) = 0, \tag{2.17}$$

$$\frac{\partial(\rho \vec{u})}{\partial t} + \vec{\nabla} \cdot \rho \vec{u} \otimes \vec{u} = -\vec{\nabla} p + \vec{\nabla} \cdot \bar{\bar{\tau}} + \rho \vec{f}, \tag{2.18}$$

$$\frac{\partial(\rho e)}{\partial t} + \vec{\nabla} \cdot (\rho e + p) \vec{u} = \vec{\nabla} \cdot (\bar{\bar{\tau}} \cdot \vec{u}) + \rho \vec{f} \vec{u} + \vec{\nabla} \cdot \vec{q} + r, \tag{2.19}$$

where ρ is the density of the fluid, $\vec{u}$ the velocity, p the pressure, $\bar{\bar{\tau}}$ the viscous shear stress tensor, $\vec{f}$ the body forces, e the total energy, $\vec{q}$ the heat flux variation and r the heat source term.
In the present flow regime with $\mathrm{Re}_D \approx 2000$ and $\mathrm{M} \approx 0.8$, these equations are not simplified, as it is important to take all aspects into account, from viscous to compressibility effects and turbulence.
The next step is the discretisation of those equations to solve them numerically. The NSE are first discretized spatially and then temporally as separate space and time discretization offers more flexibility and stability.

2.2.2 Discontinuous Galerkin method

The discontinuous Galerkin method (DGM) is a method for solving differential equations. It combines the use of finite element and finite volume methods (FVM) for spatial discretisation. This is especially interesting in the context of computational fluid dynamics where the finite element method allows high order approximation inside elements and the finite volume method can manage strong gradients.
This combination of formulations leads to the approximation of the solution by functions that are regular within each element e, but not necessarily continuous across element boundaries, see Fig. 2.13.
On each element, the solution is approximated by polynomial functions of interpolation order p. In this work, polynomials of order n are referred to as pn.

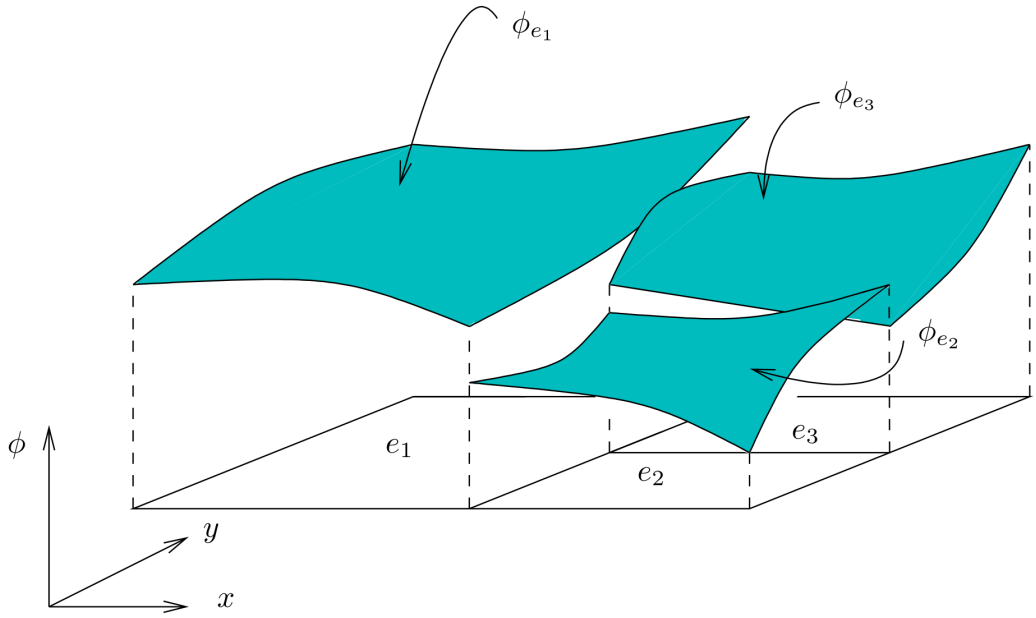

Figure 2.13: Discontinuous finite element interpolation, taken from [37].

2.2.3 Riemann problem

The use of DGM and consequently FVM formulation implies the calculation of the numerical fluxes at each element interface [38]. This is equivalent to solving a Riemann problem [39], which is an initial value problem composed of conservation equations with piecewise constant initial data with a single discontinuity on the considered domain. In the case of the Navier-Stokes equations, changes in the flow can be transmitted only through entropy waves and acoustic waves, and only at some given speeds, which represent the eigenvalues of the governing non-linear equations system.
As a Riemann problem is solved at every mesh element interface and at every time step, the use of an exact Riemann solver such as Godunov's method is expensive. However, multiple approximate Riemann solvers exist such as Osher-Solomon, Roe, Lax-Friedrichs, SLAU, HLL and so on.
The Roe and Lax-Friedrichs solvers are presented in more details in the next subsections as they are used in this work and their differences are important when dealing with transonic flows.

Roe

The Roe scheme is a type of linearized Riemann solver [39] where all the waves are replaced by linear waves with the idea that the speed of each wave is almost identical between two adjacent elements. Following [40], the Roe scheme can be expressed as the sum of a central term and a numerical dissipation term in the form:

$$\tilde{F} = \frac{1}{2}(\bar{F}_L - \bar{F}_R) + \tilde{F}_d, \tag{2.20}$$

with $\tilde{F}$ the numerical flux and $\tilde{F}_d$ the numerical diffusive term. The subscripts L and R stand for the adjacent left and right elements respectively. At the interface, $\bar{F}$ is given as

$$\bar{F} = U \begin{bmatrix} \rho \\ \rho u \\ \rho v \\ \rho w \\ \rho H \end{bmatrix} + p \begin{bmatrix} 0 \\ n_x \\ n_y \\ n_z \\ 0 \end{bmatrix}, \tag{2.21}$$

where H is the enthalpy, n_x, n_y, and n_z refer to the components of face-normal vector n, and $U = n_x u + n_y v + n_z w$ is the normal velocity on the element face. In general, the numerical dissipation term $\tilde{F}_d$ is expressed in the form

$$\tilde{F}_d = -\frac{1}{2} R D R^{-1} \Delta Q, \tag{2.22}$$

with R the right eigenvector matrix of the Navier-Stokes equations, D is the diagonal matrix formed with the associate eigenvalues and $\Delta Q = Q_R - Q_L$, with Q the vector of conservation variables (ρ, ρu, ρv, ρw, ρE). The eigenvalues of D are:

$$\lambda_1 = \lambda_2 = \lambda_3 = |U|, \quad \lambda_4 = |U - c|, \quad \lambda_5 = |U + c|, \tag{2.23}$$

with c the speed of sound.
The issue with the Roe scheme is that wave linearization removes the distinction between compression shocks and expansion shocks, leading to unphysical entropy generation. Also, from a mathematical stand point, λ_4 is zero at the sonic points which renders the system of the Navier-Stokes equations rigid [40]. In other words, at sonic points the scheme is unstable [41], [42].
To prevent small eigenvalues, a correction is applied called "entropy fix". The eigenvalues are then replaced by:

$$\lambda_i = \begin{cases} \lambda_i & \text{if} \quad \lambda_i \geq \delta, \\ \frac{\lambda_i^2 + \delta^2}{2\delta} & \text{if} \quad \lambda_i < \delta, \end{cases} \tag{2.24}$$

with $\delta = \varepsilon_\lambda \max(\lambda_i) = \varepsilon_\lambda(|U| + c)$ where ε_λ is a constant and usually varies between 0.05 and 0.2.
In ArgoDG, ε_λ is a user defined parameter.

Lax-Friedrichs

The Lax-Friedrichs scheme is a type of two-waves Riemann solver. Two-waves solvers consider that only one wave propagates in each direction. In the Lax-Friedrichs scheme, it is assumed that both waves have the same speed a, in opposite directions, which gives the following expression for the numerical flux:

$$\tilde{F} = \frac{1}{2}(\bar{F}_L + \bar{F}_R) - \frac{a}{2}(Q_R - Q_L). \tag{2.25}$$

The wave speed a different for each Riemann problem is chosen as the fastest wave speed appearing in the true Riemann solution to insure stability. However, this method introduces numerical diffusion and can lead to substantial damping of the slower waves [39].

2.2.4 Temporal discretisation

Now that the NSE are spatially discretized with the DGM, temporal integration is needed to solve the resulting system. Multiple time integration schemes exist. In this work, this is done with the implicit, A-stable, second order backward differentiation formula (BDF2) with the following formula:

$$y_{n+2} - \frac{4}{3}y_{n+1} + \frac{1}{3}y_n = \frac{2}{3}hf(t_{n+2}, y_{n+2}), \tag{2.26}$$

with the time-step h [43].

2.2.5 Newton-GMRES method

At each time-step, the resulting global non-linear system is solved by using first a Newton linearization and then the well known GMRES algorithm. All details about the GMRES algorithm can be found in [44].
With the convergence criteria for GMRES to solve the linear system $Ax = b$:

$$||Ax - b||_2 \leq \text{Gtol}\ ||b||_2, \tag{2.27}$$

the standard Newton-GMRES algorithm can be decomposed in the following steps:

Input: Newton Prediction: $\hat{u} = u^{(n)}$, GMRES Tolerance: Gtol, Newton Tolerance: Ntol
Output: Solution $u^{(n+1)}$ of $R_n(u^{(n+1)}) = 0$

- $u^{(n+1)} = \hat{u}$
- **while** $||R_{n+1}(u^{(n+1)})||_\infty >$ Ntol **do**

1. Evaluate residual $R_{n+1}(u^{(n+1)})$
2. Evaluate Jacobian $\frac{\partial R_{n+1}}{\partial u}(u^{(n+1)})$
3. Solve $\frac{\partial R_{n+1}}{\partial u}(u^{(n+1)})p = -R_{n+1}(u^{(n+1)})$ for p using GMRES with tolerance Gtol in (2.27)
4. $u^{(n+1)} = u^{(n+1)} + p$

- **end while**

In DG discretizations, the Jacobian are very large and the CPU time required to compute a Jacobian evaluation (line 2) is one order of magnitude more expensive than a residual evaluation (line 1) [45]. However, using the same Jacobian for several GMRES iterations is possible while generating decent inexact-Newton directions. This is called Jacobian recycling.
For non-linear problems, there is a limit to the number of times a Jacobian can be reused, but only 5 re-uses can already reduce the total computation time by a factor of 3. In ArgoDG, the Jacobian recycling number is defined via the FreezeJacobianMatrix parameter.
GMRES tolerance is also an important parameter to chose properly, which can counter-intuitively reduce the robustness of the algorithm when too high precision is required [46]. Appropriate values of Gtol are between 1e-3 and 1e-2 [45].

Algorithm failure

Multiple reasons can lead to the failure of the Newton-GMRES algorithm :

- Unphysical simulation setup.
- Bad mesh quality.
- Physical contacts are too stiff.
- The convergence criteria are too strict.
- The maximum Newton iterations are too low.

Some of those issues are encountered and addressed in this work, see the transient solutions in chapter 5.

3 Experimental environment

The aim of this work is to numerically reproduce the experimental setup of the SPLEEN project in order to obtain and compare numerical results with experimental ones.
The SPLEEN project provides an experimental database on the subject of Secondary and Leakage Flow Effects in High-SPeed Low-PrEssurE TurbiNes. It began in 2018 and is still ongoing at the Von Karman Institute.
The rotor-stator interaction analysis, see Simonassi et al. [12], is only a part of the SPLEEN project. The experimental data used in this work is available on the online platform *Zenodo*, with the following updates [47], [48], [19]. SPLEEN is funded by the European Union's Horizon 2020 research and innovation program.

In this chapter, the wind tunnel and test section are presented, then the blade cascade and wake generator setups and hypothesis, followed by the experimental parameters and operating conditions. Those experimental parameters and operating conditions will determine the computational domain and boundary conditions used in the numerical simulation, see section 4.2.

3.1 Wind tunnel and test section

The experiments in the frame of the SPLEEN project are conducted at the VKI. The wind tunnel design used to perform the experiments is shown in Fig. 3.1. Following the arrows, the air flow is rotating in the counter clockwise direction, entering from the right in the *test section* located in the upper left corner. In the present case, all elements of interest are contained in the test section, such that the blade cascade, the wake generator, the turbulence grid, and the related sensors to retrieve the flow information.

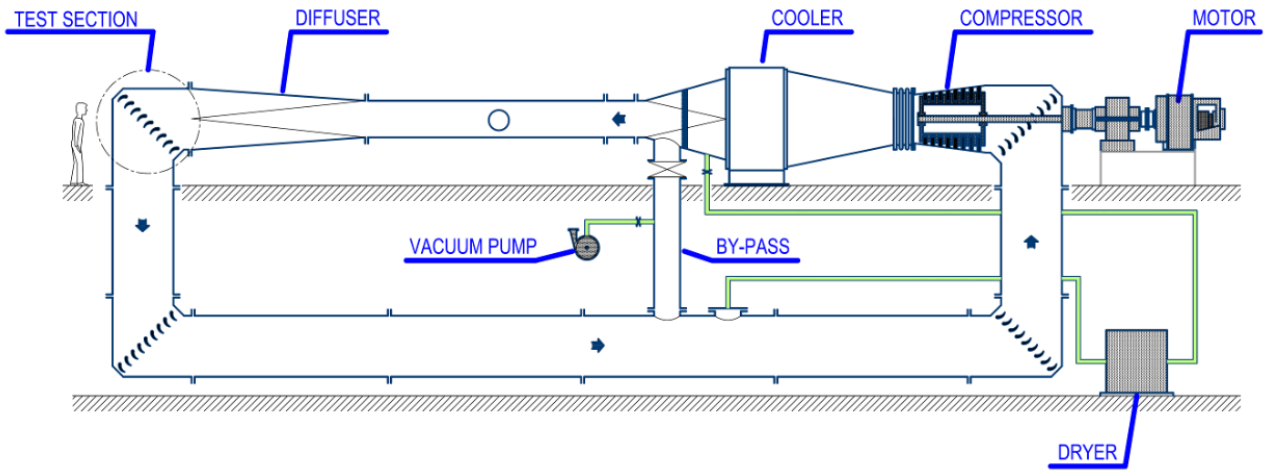

Figure 3.1: Wind tunnel at VKI, taken from [47].

A sketch and a picture of the test section are shown in Fig. 3.2 where inlet and outlet flow conditions are visible. Fig. 3.3 sketches a 3D representation of the front (a) and rear view (b) of the the test section. In (a), one can see the blade cascade as well as some of the 96 wake generator bars and in (b), the motor of the wake generator is visible.
The blade cascade as well as the wake generator are mounted on the same disc that can be rotated such as to change the inlet flow angle of the cascade. The inlet flow angle is different with and without wake generator, more details in section 3.3.1.

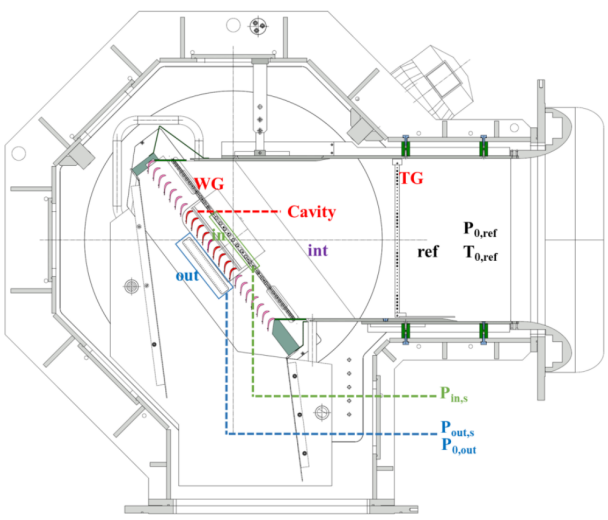

(a) Sketch of the test section with WG = wake generators and TG = turbulence grid. The flow is entering from the right and goes out by the bottom.

(b) Picture of the wind tunnel test section at VKI.

Figure 3.2: Wind tunnel test section at VKI, from [48].

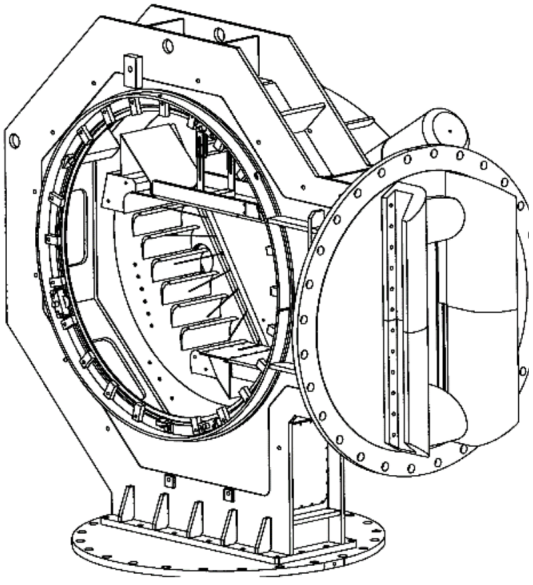

(a) 3D view of the inside of the test section.

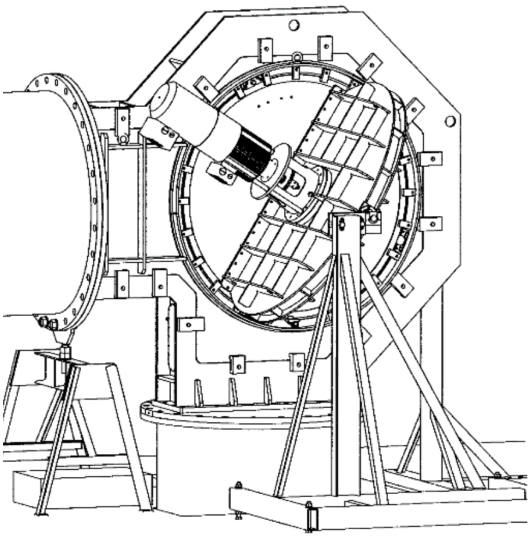

(b) 3D view of the test section from the other side.

Figure 3.3: Test section 3D views. [48].

The region of interest (ROI) is depicted in Fig. 3.4 (a) with the blade cascade in red, and a bar of the wake generator in yellow. A sectional view of the test section is shown in Fig. 3.4 (b) where the ROI, rotated by 135°, can be seen at the bottom of the figure.

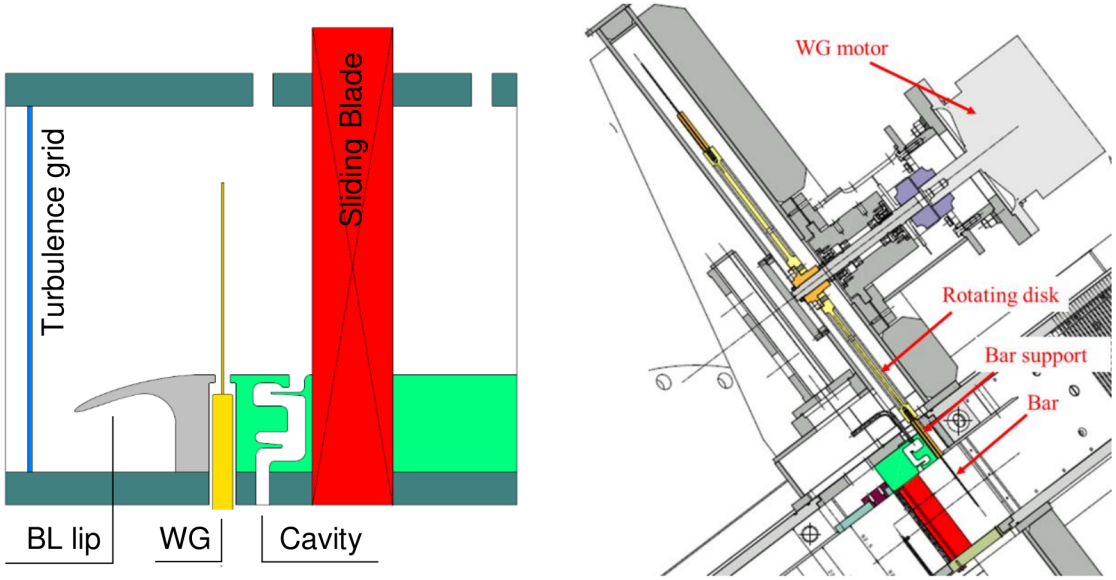

(a) Region of interest (ROI) in the test section.

(b) Sectional view of the test section with the ROI at the bottom of the sketch.

Figure 3.4: Region of interest in the test section and sectional view [48].

3.2 Blade cascade

In the SPLEEN project, two airfoil geometries are initially considered for the blade cascade design. Those airfoils are real engine scale LPT blades. *Airfoil 1* with a scaling factor of 1.6 is finally chosen for most of the experimental tests, whose geometry parameters can be found in Table 3.2. This scaling factor has been chosen in order to respect the outlet isentropic Mach and Reynolds numbers of the real LPT, while maintaining an outlet static pressure higher than 5000 Pa to ensure safe/regular operation of the facility. Indeed, an outlet static pressure below 5000 Pa implies a longer stabilization time of the inlet total pressure for each experiment and potential oil vaporization leading to possible damages to the compressor. More details on the experimental campaign can be found in [48].
The blade cascade is composed of a series of 23 Airfoil 1 geometry blades, see Fig. 3.5 (a) for a zoom on the central blades, and Fig. 3.2 (a) for the complete cascade.

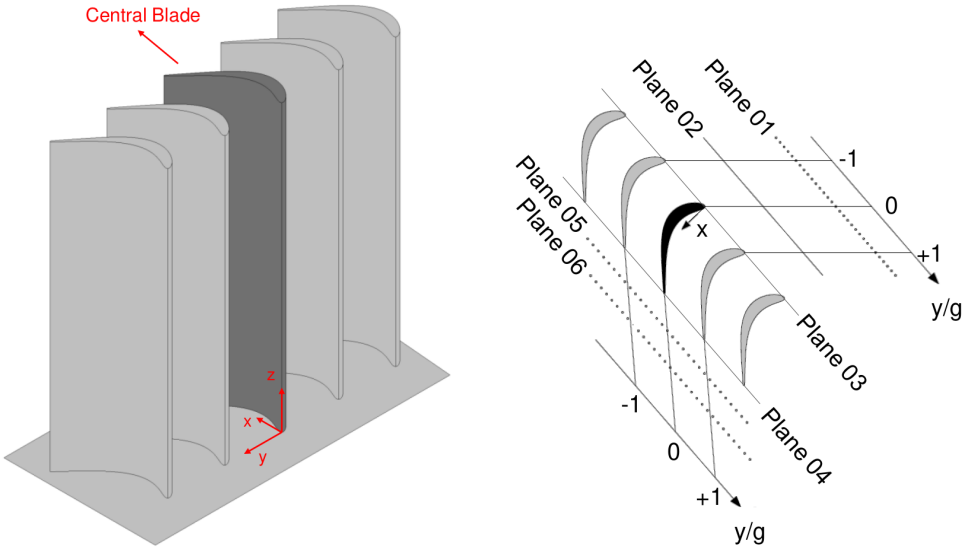

(a) Reference system.

(b) Measurement planes.

Figure 3.5: Blade cascade, taken from [48].

The reference system can be seen in Fig. 3.5 (a). In this work, the x, y and z directions are often referred to as stream-wise, pitch-wise and span-wise directions respectively.
The measurement planes shown in Fig. 3.5 (b) indicate sensors locations and therefore where flow information such as pressure, temperature, velocity, etc are available and can be compared to numerical data. See Fig. 3.10 for the related sensors, and Table 3.3 for the exact planes locations.
The span of the blades is defined in order to neglect the end wall effect at mid-span. Also, all measurements are performed on the central blade of the cascade to limit the impact of the walls in the pitch-wise direction.

3.3 Wake generator

In the SPLEEN project, the wake generator is composed of 96 bars rotating at 3300 RPM upstream of the blade cascade, see Fig. 3.6. The use of rotating bars instead of translating bars, see setup examples in section 2.1.6, allows much higher rotating speeds which are closer to real LPT conditions.

(a) Setup with the rotating bars.

(b) Setup with the rotating bars and the blades behind.

Figure 3.6: Wake generator and blade cascade setup setup at VKI [48].

3.3.1 Hypothesis and adjustment

Blade like wake

The use of cylindrical bars to simulate the wakes shed by upstream turbomachinery blades has been validated by Pfeil et al. [49]. They showed that the structure of the far wake of an airfoil and that of a cylindrical body of the same drag is almost identical (at a distance above 80 times the diameter of the bar). Additionally, Schulte and Hodson [50] showed that this similitude holds true also at a distance ranging between 40 and 80 times the bar diameter [19].
In the present experimental case, the horizontal distance between the wake generator and the LE of the blades is $1.12 \times c_{ax} = 53$ mm and the bar diameter is 1 mm. So, the conditions for the simulation of the wake of blades by rotating bars are fulfilled in terms of geometry parameters. However, in terms of flow conditions, there are some discrepancies between the SPLEEN experimental setup and the previously used setups, see section 2.1.6. The bars are rotating at much higher speed which increases the relative flow velocity and the pressure is also much lower in the SPLEEN wind tunnel. Those environmental conditions are made to be closer to real LPT conditions, however, there are far from the ones that validated the use of rotating cylinders to represent the wake of turbine blades. Those differences between generated wake and blade wake are shown in the results chapter section 6.4.

Midspan 2D flow

The region of interest (ROI) is defined as the region without (1) the influence of the tip of the wake generator, (2) the endwall secondary flows and purge and (3) the boundary layers and endwall flows developed on the outer cascade walls, see Fig. 3.7 (a). With those considerations that have taken into account the design of the test section, at the midspan location, the flow can be considered as 2D. The final design of the wake generator is depicted in Fig. 3.7 (b). The final length of rotating bars results from the balance between reducing the effects of the bar tip and reducing the centrifugal load.

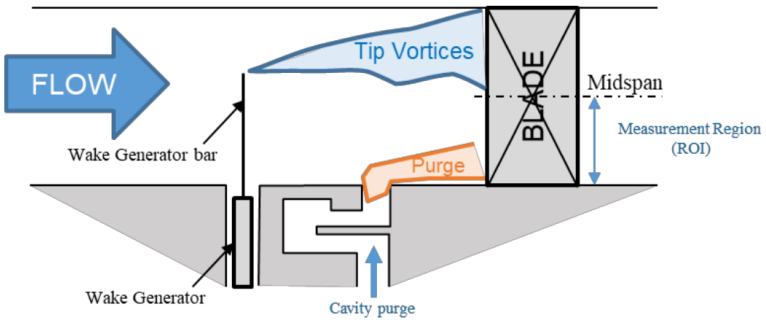

(a) Setup with the rotating bars

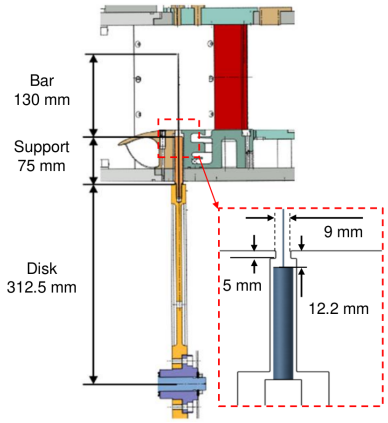

(b) Setup with the rotating bars and the blades behind

Figure 3.7: Midspan hypothesis, taken from [48].

The peripheral velocity of the bars v_b is computed from the rotational velocity of the WG ($\Omega = 3300$ RPM) and the distance from the center of rotation to the region of interest ($r = 482.2$ mm), see Fig. 3.7 (b):

$$v_b = \frac{2\pi\Omega}{60} r = 166.636 \text{ m/s}. \tag{3.1}$$

Incidence angle correction

The blade cascade and the WG are on a rotating disc, see Fig. 3.2 and 3.3. This disc allows to rotate the blade cascade in order to change the inlet flow angle with respect to the blade cascade. The aim is to have the flow aligned with the LE of the blades i.e. the same inlet flow angle as the blade metal angle.
After the experimental tests without the WG, it has been noticed that the inlet flow angle was actually 36.3° and not 37.3° but it was too late to change it. Also, an incidence angle of $-1°$ is acceptable.
With the WG, the rotating bars induce a change in the global flow angle of about 6.1° ($37.3 - 31.6$) see [16]. In order to realign the flow with the midspan blade LE, the disc carrying the blade cascade and the WG is rotated from 40.73° to 46.9°. After this change, the incidence angle has been reduced to $-2°$, see Fig. 3.8. This disc rotation of 6.17° has to be taken into account in the numerical simulation, in order to be as close as possible to the experimental conditions. So, the inlet flow angle in the numerical simulation is set to 42.47°. A comparison is made with the resulting final incidence angle of $-2°$ obtained experimentally in section 6.1.3. Table 3.1 summarizes the experimental procedure of the incidence angle correction.

	Without WG	**With WG**	**WG and correction 1**	**WG and correction 2**
Cascade angle	40.73°	40.73°	44.9°	46.9°
Blade metal angle	37.3°	37.3°	37.3°	37.3°
Flow angle at LE	36.3°	-	34°	35.3°
Incidence angle	$-1°$	-	$-3.3°$	$-2°$
Inlet flow angle	36.3°	36.3°	40.47°	42.47°

Table 3.1: Summary of the incidence angle correction with the WG.

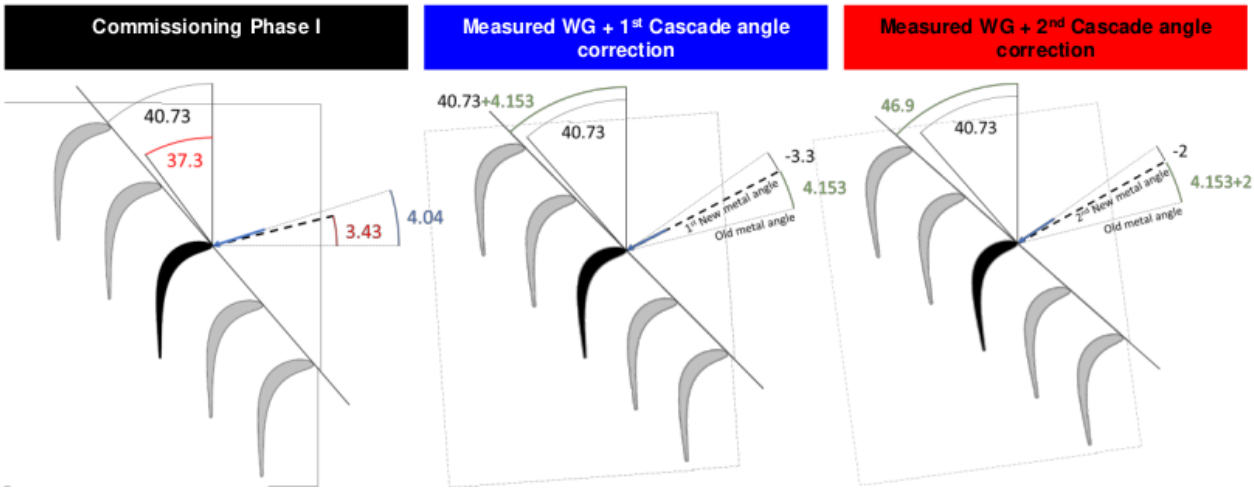

Figure 3.8: Incidence angle correction, taken from [19].

3.4 Experimental setup

In this last section, the final geometry parameters and operating conditions from the experimental campaign are gathered.

3.4.1 Geometry parameters

The scheme of the rotating bars in front of the blade cascade is shown in Fig. 3.9 and the related parameters in Table 3.2.

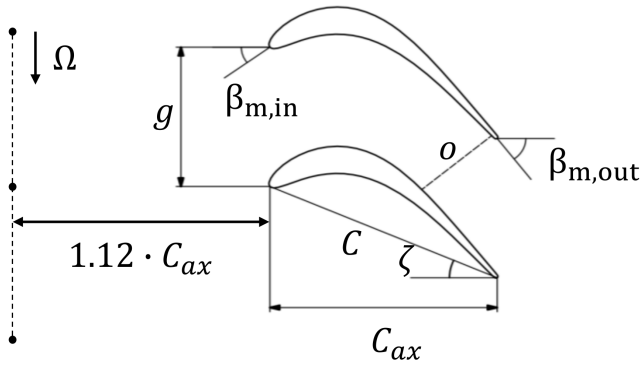

Figure 3.9: Wake generator and blade cascade geometry, taken from [12].

Parameter	Symbol	Value	Units
True chord	c	52.280	[mm]
Axial chord	c_{ax}	47.610	[mm]
Pitch	g	32.950	[mm]
Span	H	165.000	[mm]
TE radius	$\delta_{TE}/2$	0.435	[mm]
Throat opening	o	19.400	[mm]
Inlet angle	$\beta_{m,in}$	37.300	[°]
Outlet angle	$\beta_{m,out}$	53.800	[°]
Stagger angle	ζ	24.400	[°]
Maximum roughness	Ra	1.670	[µm]
Rotating velocity	Ω	3300	[RPM]
Peripheral velocity	v_b	166.636	[m/s]

Table 3.2: Setup geometry parameters of the spleen c1 project [12].

3.4.2 Operating conditions

In the experimental SPLEEN project, the operating conditions are defined from imposed outlet isentropic Mach and Reynolds numbers. In the experimental campaign, multiple operating conditions are tested with $Re_{6,is}$ = [65k 70k 100k 120k] and $M_{6,is}$ = [0.7 0.8 0.9 0.95]. The subscript 6 indicates the measurement Plane 06 which corresponds to the outlet of the test section.
The related inlet total pressure $p_{0,in}$ and outlet static pressure p_{out} are adjusted following Eq. (2.1) and measured at Plane 02. The inlet total temperature $T_{0,in}$ is adjusted from its relation with the $Re_{out,is}$ through the isentropic equations: $T_{0,in}$ is measured at plane02, the inlet of the test section. From that measurement, the values of $\rho_{is,out}$ from Eq. (2.3), T_{out} from Eq. (2.4), $U_{is,out}$ from Eq. (2.5), $\mu_{is,out}$ from Eq. (2.6) and ultimately

$Re_{out,is}$ from Eq. (2.2) can be retrieved. Then $T_{0,in}$ is fixed for each chosen value of $Re_{out,is}$.
The measurement planes as well as the sensors used to perform the operating conditions selection are shown in Fig. 3.10. The position of the measurement planes are gathered in Table 3.3.
In particular, the wake generator (WG) is positioned at Plane 01, in front of the blades whose LE is located at Plane 03.

In the present work, the operating conditions are fixed with $Re_{6,is}$ = 70k and $M_{6,is}$ = 0.7. The resulting flow conditions are gathered in Table 3.4. Those fixed experimental flow conditions are used to set the boundary conditions of the computational domain in the numerical environment described in the next chapter.

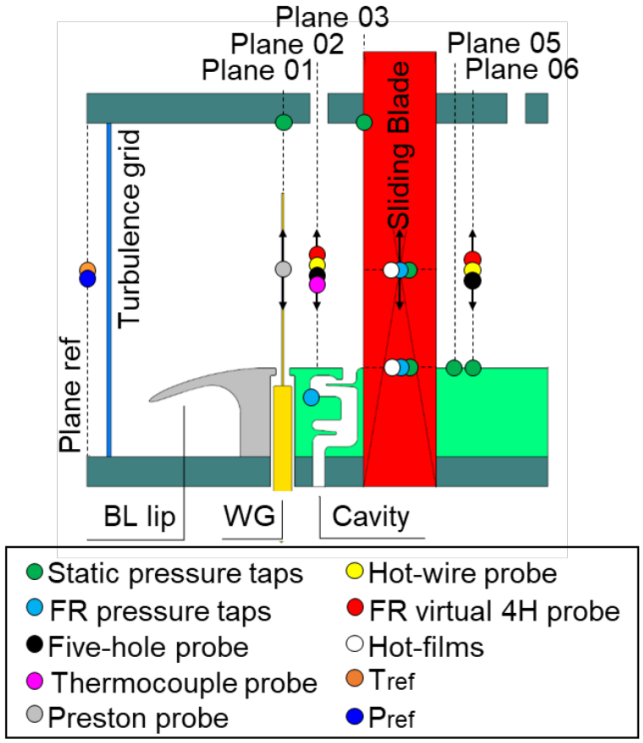

Figure 3.10: Region of interest of the test section of the wind tunnel, with measurement planes and sensors [51].

Plane 01	**Plane 02**	**Plane 03**	**Plane 04**	**Plane 05**	**Plane 06**
$-1.12c_{ax}$	$-0.5c_{ax}$	$0.0c_{ax}$	$1.0c_{ax}$	$1.25c_{ax}$	$1.5c_{ax}$

Table 3.3: Axial location of measurement planes, reproduced from [19].

Quantity	**Symbol**	**Value**	**Units**
Inlet total pressure	$p_{0,in}$	10779.39	[Pa]
Inlet total temperature	$T_{0,in}$	300	[K]
Inlet flow angle	α	42.47	[°]
Outlet static pressure	p_{out}	7771.16	[Pa]
Is. out. Reynolds number	Re	70,000	[-]
Is. out. Mach number	M	0.7	[-]

Table 3.4: Operating conditions.

4 Numerical environment

In this chapter, the numerical tools and computational domains with flow conditions are defined.

4.1 Numerical tools

The core of this work is the numerical simulation of the interaction between the wake generator and the blade cascade. This numerical simulation is done with two main softwares: *Gmsh* and *ArgoDG*. Gmsh is used for discretization of the numerical domain into a 3D mesh, followed by a mesh partitioning to allow parallel computation. Then, ArgoDG is used to compute the flow following the steps described in section 2.2. The Newton-GMRES algorithm is run on the *Lucia* cluster.
Finally, the results are visualized using *Paraview*.
Those numerical tools introduced here are presented in more details in the next subsections, with a particular focus on the specifics linked to this work.

4.1.1 Gmsh

Gmsh is a finite-element mesh generator developed by Christophe Geuzaine and Jean-François Remacle [52]. The meshes used in this work and the partitioning for parallel computation have been realized with this mesh generator.

4.1.2 ArgoDG

ArgoDG is a software developed at Cenaero with no granted access to the code. The information given in the following subsections come from literature review as most of the implemented tools definition are accessible in the literature. Only the sponge layer definition and parameters come from the *Argo user manual*.

Sponge layer

A *sponge layer* is a tool implemented in ArgoDG that is primarily used to damp flow fluctuations that are likely to cause spurious reflections at inlet or outlet boundaries. The damping is achieved by adding a source term that penalizes the difference between the local solution u and its moving time average $\bar{u}$.
The amplitude of this source term is set by the penalty factor σ. The penalty factor is added into the general advection-diffusion equations as follows:

$$\frac{\partial \mathbf{u}}{\partial t} + \nabla \cdot \mathbf{F}(\mathbf{u}) + \nabla \cdot \mathbf{D}(\mathbf{u}) + S(\mathbf{u}) = \sigma(\mathbf{x})(\bar{\mathbf{u}} - \mathbf{u}), \tag{4.1}$$

with $\mathbf{F}(\mathbf{u})$ and $\mathbf{D}(\mathbf{u})$ the convective and diffusive fluxes, and $S(\mathbf{u})$ the source terms. The time average $\bar{\mathbf{u}}$ is computed using a moving-average strategy. The period during which $\bar{\mathbf{u}}$ is computed, is based on the physics of the simulated phenomena. In the present case, for the wake generator, the averaging period is defined by the vortex shedding period in the bar wake. The damping factor σ is defined as a function of the spatial

variables, typically to allow a rapid increase towards the boundaries of the domain.
A 1% difference between $\mathbf{u}$ and $\bar{\mathbf{u}}$ at the end of the sponge layer is considered sufficiently small. So, the penalty factor is adjusted following

$$\int_{x_0}^{x_1} \frac{\sigma(x')}{a} dx' = -\ln(0.01), \tag{4.2}$$

with a the local flow velocity and assuming that the sponge layer starts at x_0 and ends at x_1. Expression 4.2 can be simplified into

$$\sigma = -\frac{a\ln(0.01)}{x_1 - x_0}, \tag{4.3}$$

considering that $\sigma(x')$ increases sufficiently fast to the constant value σ. See section 5.1.3 for sponge layer applications.

Artificial viscosity

The presence of a shock is a concern in a numerical simulation as its thickness is of the order of magnitude of the *mean free path* so about 10^{-8} m. The capturing of the shock by an adapted mesh refinement is not possible as it would require either a too long computation time or too much computational resources. To give an estimation, the computation of one convective time takes about 4.4 days with 30 nodes on Lucia. About 4M elements with a smallest mesh size element of 10^{-5} m are used, see chapter 5 for more details. Decreasing the mesh size from 10^{-5} m to 10^{-8} m would require about 1000 times more elements and so 1000 times more nodes on Lucia (300 max). The is clearly unfeasible so the shock is doomed to be under resolved. It leads to large discontinuities inside elements resulting in strong oscillations (Gibbs oscillations) for high order methods such the one used in the present case (p3).
A solution to this problem lies in the shock formation mechanism. Indeed, this small thickness is the result of the shock steepening effect, see section 2.1.3. The idea behind the artificial viscosity (AV) is to stop the steepening of the shock waves, therefore increase the shock thickness and soften the local discontinuity, see Fig. 4.1.

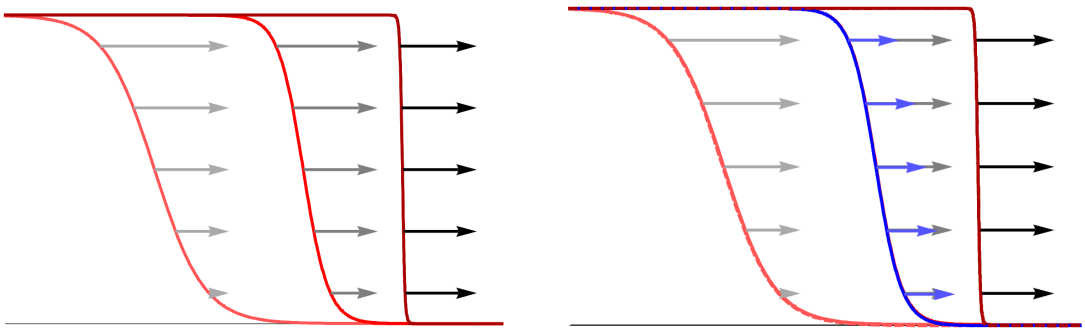

(a) Shock wave steepening.

(b) Shock wave steepening artifically stopped.

Figure 4.1: Shock steepening and artificial viscosity, taken from [53].

Nevertheless, a mesh refinement at the shock location is needed, and is this case, a region of the mesh must be refined as the shock is moving, see mesh in section 4.2.1.

In *ArgoDG*, the use of the AV can be viewed as a shock capturing method, following the approach proposed by Persson and Peraire [54]. To limit the impact of the AV on the real flow physics, the AV is only applied on elements where the discontinuity is too important. The identification of those elements is done by a discontinuity sensor. The amplitude of the discontinuity inside an element is evaluated through the difference between the solution approximated by order p and $p-1$ orthogonal polynomials. The solution of order p

and order $p-1$ within each element is given by:

$$u = \sum_{i=1}^{N(p)} u_i \psi_i, \quad \text{and} \quad \hat{u} = \sum_{i=1}^{N(p-1)} u_i \psi_i,$$

where $N(p)$ is the total number of terms in the expansion and ψ_i are the basis functions.
Within each element Ω_e, the smoothness indicator, is defined by:

$$S_e = \frac{(u-\hat{u}, u-\hat{u})_e}{(u,u)_e},$$

where $(\cdot,\cdot)_e$ is the standard inner product in $L2(\Omega_e)$.
The AV is introduced into the equations by adding a Laplacian term of the form $\nabla \cdot (\epsilon_e \nabla \mathbf{U})$. The value of ϵ_e is smoothly applied to the elements through the following function:

$$\epsilon_e = \begin{cases} 0 & \text{if} \quad s_e < s_0 - C, \\ \frac{\epsilon_0}{2}\left(1 + \sin\frac{\pi(s_e - s_0)}{2C}\right) & \text{if} \quad s_0 - C \leq s_e \leq s_0 + C, \\ \epsilon_0 & \text{if} \quad s_e > s_0 + C, \end{cases}$$

with $s_e = \log_{10}(S_e)$ coming from the discontinuity sensor with s_0 the value of the threshold defined by the user and the parameter C determining the smoothness of the AV application. The maximum amplitude of the AV is defined by:

$$\epsilon_0 = k \frac{h}{p} \lambda_{\max},$$

with h the element size, p the polynomial order, $\lambda_{\max}$ the maximum wave speed and k a user define parameter. In summary, the three parameters determining the AV and defined by the user are:

$$\begin{cases} C & \text{smoothness}, \\ s_0 & \text{activation threshold}, \\ k & \text{amplitude}. \end{cases}$$

Some examples of application of shock capturing with higher-order, PDE-based artificial viscosity can be found in Barter and Darmofal [55].

Velocity perturbation

At the restart of a simulation, a velocity perturbation can be added to the existing velocity field as a “white noise”. This white noise is bounded by a user chosen amplitude as a percentage of the local velocity. The usage of the VP is to speed up the transition from 2D to 3D flow. Indeed, from the imposed initial and boundary conditions, the flow is initially perfectly constant in the third direction making it a “2D flow”. In a numerical simulation, it is the machine error that causes the transition from 2D to 3D but this process is rather slow.

Riemann solver

In ArgoDG, the following Riemann solvers are available : Roe, Lax-Friedrichs, SLAU, Godunov, SLAU2 and Central. The Roe solver is less dissipative than Lax-Friedrichs, however it is less stable in transonic flow regimes as explained in section 2.2.3. In the transient solution chapter, a switch is made from Roe to Lax-Friedrichs to stabilize the solution.

Non matching connection

Non matching connection methods are used to connect two different domains with non intersecting meshes. In the present case, this is necessary as two different domains are defined, one moving for the wake generator and one static for the blade cascade, see section 4.2. In classic FVM, non matching connection is

based on the construction of a new mesh to intersect the two meshes. This construction introduces new elements of arbitrary shape from triangles to octagons that are then decomposed into triangles to use the same quadrature rule for each element. This method of mesh intersections allows to keep the conservative property of fluxes across the two domains junction. However, it is expansive and must be done at each time-step as the domains are moving relative to each other.
In DGM, non matching connection is a much simpler process with only the interpolation of the quadrature points from one domain to the other, see Fig. 4.2.

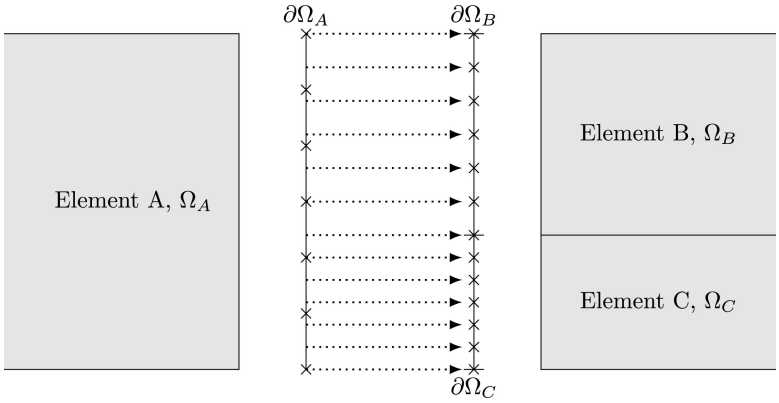

Figure 4.2: Interpolation of the quadrature points from element A to elements B and C, taken from [56].

This method is not conservative and implemented in FVM leads to wrong mass and momentum balance. In DGM however, with a sufficiently good mesh, the high order of interpolation inside elements allows the use of such simpler method without introducing much errors, see Edward Laughton et al. [56] for more details.

4.1.3 Lucia cluster

The numerical simulations performed in this work are done on the computer cluster Lucia. Lucia is hosted at, and operated by Cenaero [57]. The cluster is mainly organized into 300 nodes of 128 CPUs each and 50 nodes of 32 GPUs each. It allows to perform parallel computations by partitioning the space domain, each partition attributed to one or more CPU. In Lucia, two types of API are allowed : MPI and OpenMP. In the case of MPI, each CPU is devoted to one partition. In OpenMP, multiple CPUs can be used for each partition (up to max 4 CPUs per task for optimal parallelization). As the computational domain is divided into many elements, a rule of thumb for Lucia memory usage is to partition the mesh to have 1000 elements per partition and per CPU.
The jobs submission on Lucia is done through a *.slurm* file to specify critical information such that the resources (nodes and memory usage) and the required execution time. The maximum execution time is two consecutive days.
The queue time depends on the amount of requested resources and the number of users is the queue. For the simulations performed in this work, the required resources at the end are about 30 nodes, see Table 4.3, and are monopolized during multiple days. In that case, the queue time goes rapidly up to 2 days when Lucia's queue is full which doubles the total computation time. During summer and week-ends, Lucia's queue is smaller and the resources are more available.

4.1.4 ParaView

ParaView is an open-source, multi-platform scientific data analysis and visualization tool that enables analysis and visualization of extremely large datasets [58]. It can be automatized using pvpython which is the Python interpreter that runs ParaView's Python scripts. This tool have been used to retrieve all the simulation pictures shown in this work.
Because the data of the simulations that are stored on Lucia are too big to be transferred each time on local computer to be visualized, a tunnel is created directly between Lucia and ParaView opened in local. This is also done through a job submission on Lucia requiring 8 GPUs.

4.2 Computational domain

The computational domain reproduces the experimental setup presented in Chapter 3, see Fig. 3.9. However, the rotating bars of the experimental setup are replaced with translating bars in the numerical setup see Fig. 4.3. This change is made for simplicity, and is supported by the hypothesis validated during the experimental campaign see section 3.3.1. The rotational speed of the bars is converted into a vertically translating velocity $\mathbf{v}_b = -166\ \mathbf{e_y}$ m/s, see section 3.3.1.
To reduce the computational cost, the thickness of the domain is only a fraction of the full span, defined as 7% of the chord c so $dz = 0.07 * \text{chord} = 3.6596$ mm, which is about 2.2% of the experimental span. This thickness is validated by the correlations analysis done in section 6.1.2.

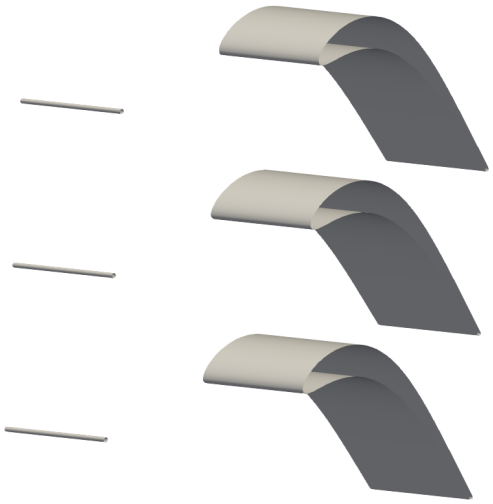

Figure 4.3: 3D view of the wake generator and the blade cascade for the numerical simulation.

Two frames of reference are defined as the bars are moving while the blades are static. One for the wake generator domain which is moving at $\mathbf{v}_b$, and a second static one for the blade cascade. A view of the full computational domain in the XY plane is shown in Fig. 4.4.

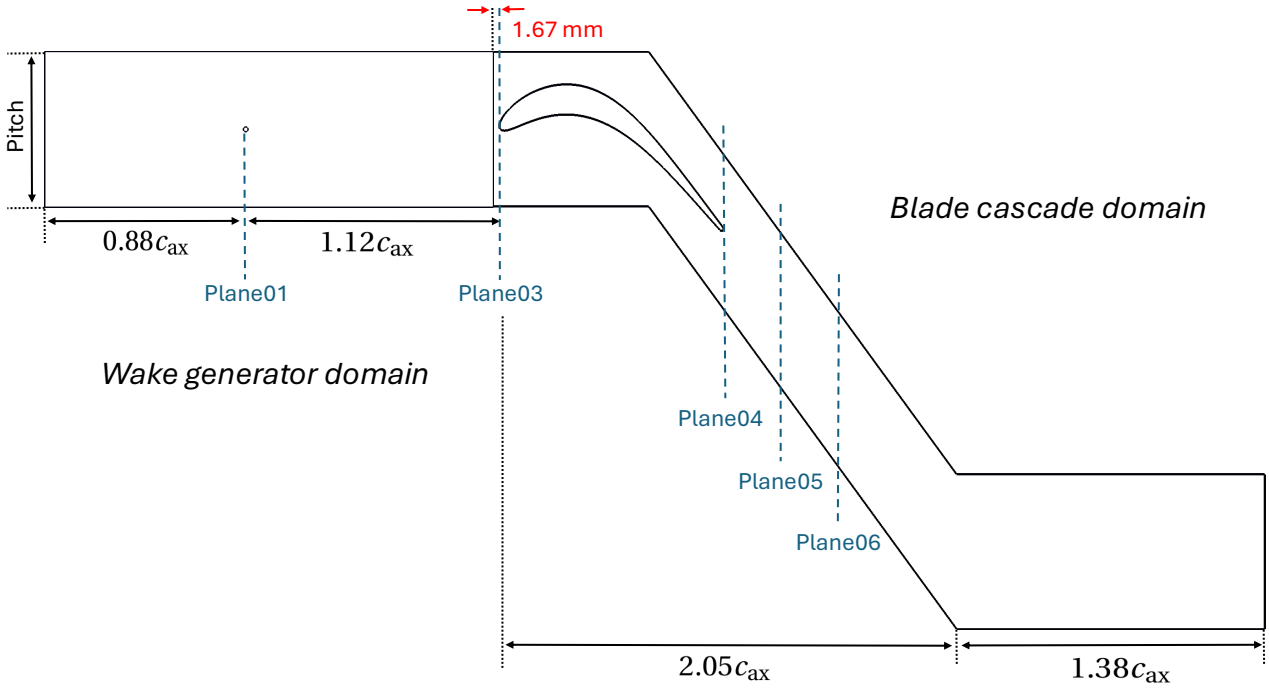

Figure 4.4: Scheme of the computational domain.

The end of the wake generator domain is chosen close to the leading-edge (LE) of the blade cascade to reduce the computational cost. Indeed, only the wake of the bar requires a local mesh refinement, see mesh in Fig. 4.6. However, because the wake generator domain is moving, the whole inlet region of the blade cascade must be refined, see mesh in Fig.4.10. So, the inlet region of the blade cascade is reduced as much as possible while maintaining a good mesh element quality at the LE. The resulting distance between the LE and the inlet of the blade cascade domain is 1.67 mm.

To save time, the idea is to not start from zero and compute directly the flow with the two domains coupled. First, the flow is established on each domain separately, then both domains are coupled. The solution for the wake generator has not been computed yet, so it has been done in this work, see section 5.1. For the blade cascade domain however, the solution is interpolated from Borbouse solution [18], on the new domain and mesh designed for the simulation of the rotor-stator interaction.
The junction between the two domains is made by non matching connections implemented in ArgoDG.

During the experimental campaign, multiple flow conditions have been tested with various outlet isentropic Mach and Reynolds numbers. In this work, only the test case with M = 0.7 and Re = 70k is investigated. The related numerical inlet and outlet boundary conditions as well as the other simulation parameters are presented in the next two subsections 4.2.1 and 4.2.2 for the wake generator and the blade cascade respectively. Then, the coupling of the two domains is described in more details.

4.2.1 Wake generator

In this section, the flow conditions, domain, boundary conditions and mesh of the wake generator are presented.

Flow conditions

The flow conditions imposed at the inlet of the wake generator are obtained from the experimental conditions, such as total pressure, total temperature and flow angle.
At the outlet of the wake generator, the static pressure is imposed. As the wake generator is located upstream of the blade cascade, the static pressure is the one at the inlet of the blade cascade. This value p_{out} at the inlet of the blade cascade is obtained from the pitch average of static pressure values at Borbouse's domain inlet [18].
The inlet flow angle is defined from the experimental setup with the adjustment to take into account the turning of the flow induced by the wake generator, see section 3.3.1.
The flow conditions of the wake generator are summarized in Table 4.1.

Quantity	Symbol	Value	Units
Inlet total pressure	$p_{0,\text{in}}$	10779.39	[Pa]
Inlet total temperature	$T_{0,\text{in}}$	300	[K]
Inlet flow angle	α	42.47	[°]
Outlet static pressure	p_{out}	9548	[Pa]

Table 4.1: Inlet flow conditions taken from the experimental SPLEEN project and outlet flow condition from Borbouse simulation [18].

Domain and boundary conditions

The numerical domain of the wake generator is a rectangular box containing the cylinder, see sketch in Fig. 4.5 and Fig. 4.4 for the dimensions. The center of the cylinder is located at the origin of the frame of reference. The boundary conditions applied at the boundaries of the domain are gathered in Table 4.2.

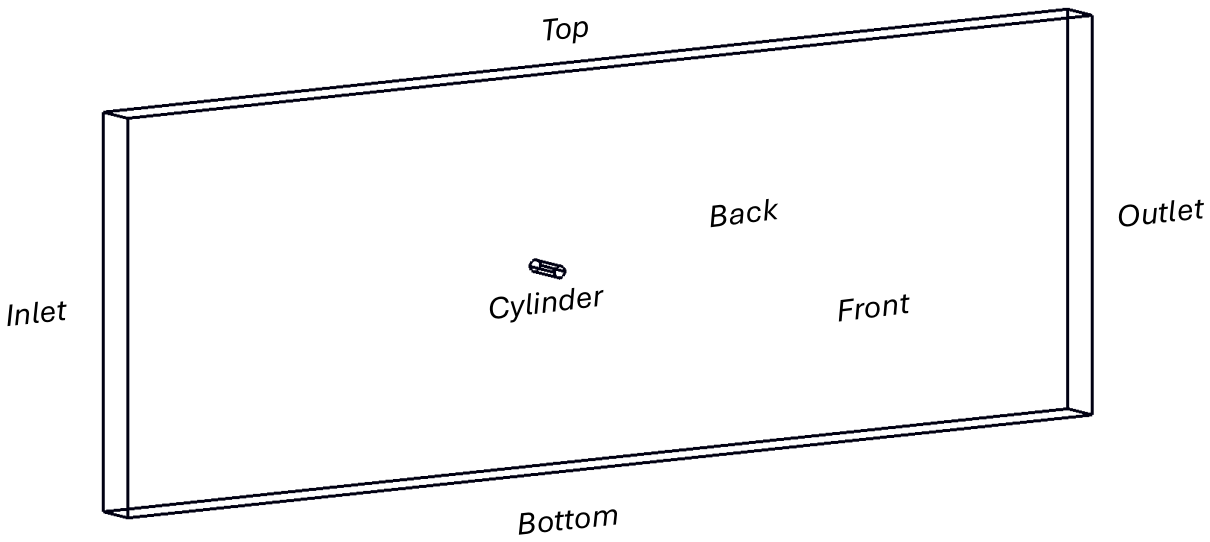

Figure 4.5: Computational domain of the wake generator.

Domain side	Boundary condition
Inlet	See Inlet Table 4.1
Outlet	See Outlet Table 4.1
Top-Bottom	Periodic
Back-Front	Periodic
Cylinder	No-slip, adiabatic

Table 4.2: Boundary conditions.

Mesh

Mesh design is always the balance between precision and computational cost. The general procedure is to increase the number of mesh elements in regions where high precision is needed and use a coarser mesh elsewhere. Typically, regions requiring high precision are regions with strong velocity gradients.
The wake generator case is no exception and four aspects of the problem that require mesh refinement are identified (see section 2.1.4 for theoretical background about the flow around a circular cylinder):

- Boundary layer close to the cylinder surface.
- Transonic flow leading to acoustic waves traveling in all directions.
- Shock behind the cylinder.
- Wake behind the cylinder.

An example of mesh used during this work is shown in Fig. 4.6. The first aspect is taken into account with small elements close to the cylinder, and increasing size when moving away from the surface, see Fig. 4.7. The second aspect leads to a maximum element size of 1 mm everywhere, especially in the upstream region of the cylinder where velocity gradients are only present because of travelling waves. Multiple refinement boxes are made to take care of the shock attached to the wake. Those boxes are used to smooth transitions between variable-size elements. In the mesh in Fig. 4.6, 3 boxes are shown. However, in the early stages of the transient solution, only one box is used, and in the last stages of the transient solution with the two domains coupled, 8 boxes are used, see 8th mesh version in Fig. 5.23b at the end of the transient solution

chapter. The last aspect is about the capture of the wake that will interact with the blade cascade downstream. “Refinement rails” are made to capture the wake without refining the whole domain downstream of the cylinder. Those refinement rails can be seen in Fig. 4.6. They are defined with the estimation of the wake angle α_w from the following velocity triangle formula:

$$\alpha_w = \arctan\left(\frac{v_f \sin\alpha - v_b}{v_f \cos\alpha}\right) \approx 67.5°,$$

with the inlet flow angle $\alpha = 42.47°$, the inlet flow velocity $v_f \approx 150$ m/s and the cylinder velocity along the y direction $v_b = -166$ m/s.

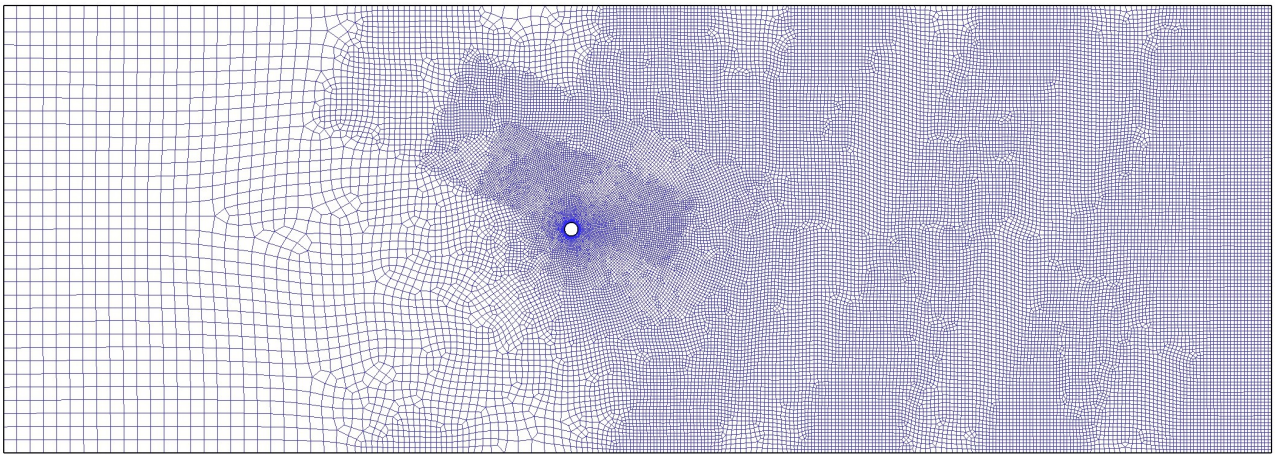

Figure 4.6: Example of mesh of the wake generator.

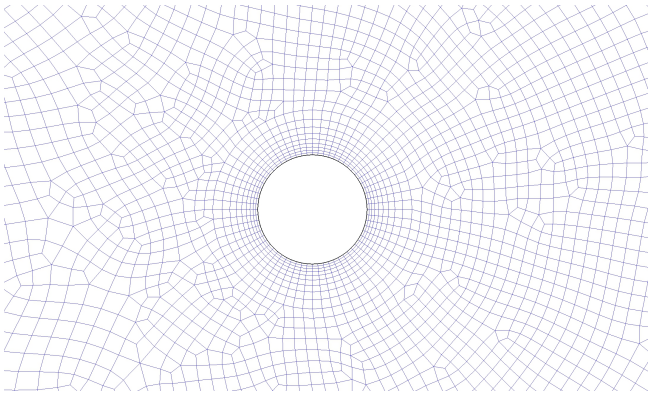

Figure 4.7: Example of mesh of the wake generator, zoom on the mesh refinement around the cylinder.

The size of the first mesh element close to the cylinder surface is chosen through the dimensionless number n+ and s+ in the normal and tangent directions to the surface respectively, defined as

$$n+ = \frac{nu^\star}{\nu},$$
$$s+ = \frac{su^\star}{\nu},$$

with n normal distance from the wall, s the tangential distance along the surface, ν the kinematic viscosity and $u^\star$ the friction velocity defined as

$$u^\star = \sqrt{\frac{\tau}{\rho}},$$

with τ the wall shear stress and ρ the density.
The span and time averaged variations of n+ and s+ along the cylinder surface are shown in Fig. 4.8. The second polar coordinate θ defines the location on the projected cylinder surface in the XY plane. This figure has been obtained afterwards from the data of the performed simulation. The stagnation point is located at -112.5° in the hollow between the two bumps on the graph. This validates the estimated wake angle of 67.5°. The maximum values of n+ and s+ are 7.8 and 19 respectively. Those values are computed with the size of the first element in contact with the cylinder surface. In high order DGM elements, the actual first degree of freedom is the first quadrature point above the cylinder surface. For p3, 4 quadrature points are defined per direction. That means that the first quadrature point is located at a distance 3 times smaller from the cylinder surface than the element size. The actual n+ and s+ values must then be divided by 3 to represent the actual precision of the method in the surface vicinity. A rule of good practice is to set the n+ and s+ values from 1 to 5 and 10 to 20 respectively. Considering that in most cases, the velocity gradients are smaller in the stream-wise direction. So, the n+ and s+ maximum values are 2.6 and 6.3 which are acceptable.

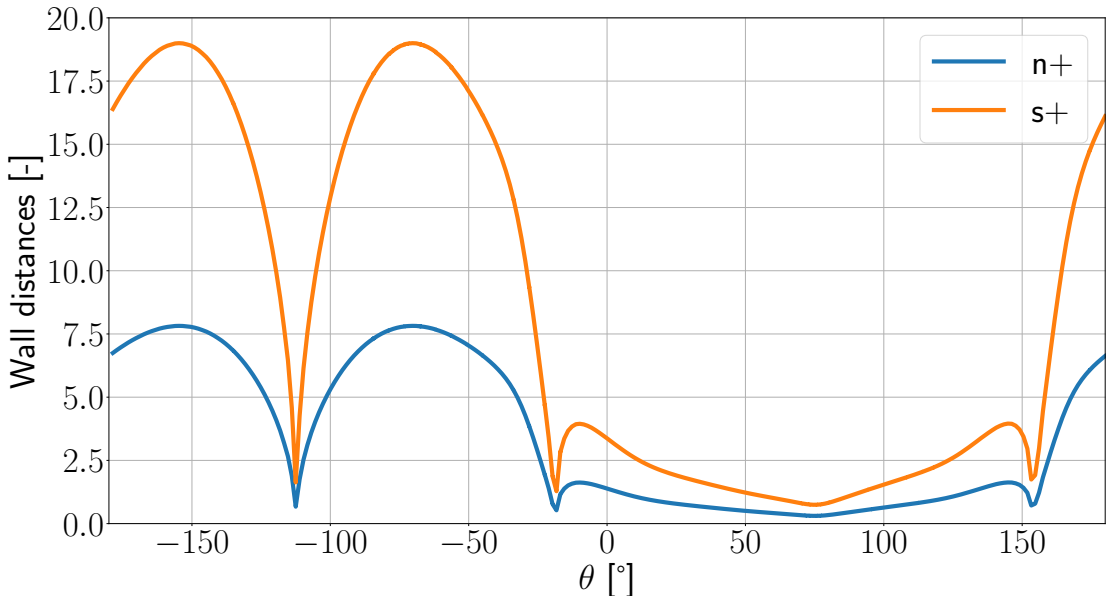

Figure 4.8: n+ and s+ span and time averaged variations along the cylinder surface.

No mesh refinement convergence study for the whole domain has been done in this work as the computation time for such simulation is high. To give perspective, the convective time of the wake generator alone is

$$t_{\text{conv}} = \frac{2c_{\text{ax}}}{v_f \cos\alpha} \approx \text{1e-3s}, \tag{4.4}$$

and the time-step used is Δt = 1e-8s which gives 100,000 iterations per convective time. Considering that the speed of the parallel computation on Lucia, with the last mesh, is about 300 iterations per hour, one convective time takes about 2 weeks to be solved (without considering Lucia's queue which often doubles the time).
So, the mesh of the wake generator has been done by gradually increasing the number of elements in the mesh, each time the solver was not able to converge, see the details of the transient solution in section 5.1. At the end of the transient solution of the two coupled domains, the whole region downstream of the cylinder was refined as the wake angle changed. However, the use of a coarser mesh in the first stages with all the adjustments to make the simulation work was crucial.

4.2.2 Blade cascade

The idea is to not compute the solution on the blade cascade like for the wake generator, but rather start from the one obtained by Borbouse [18]. This is done by interpolating Borbouse's solution on the cut domain presented in the next section. The inlet and outlet boundary conditions remain the same, but the wake generator will be placed upstream of the blade cascade.
In Borbouse's work, three Mach numbers have been analysed (0.7, 0.9, 0.95). Due to lack of time, in the present work, only the case M=0.7 is considered.

Domain and boundary conditions

The computational domain is identical than Borbouse's except for the inlet, which is cut to place in front of the wake generator. The cut is made the closest to the LE, while keeping a quality mesh, in order to reduce the number of mesh elements. As explained previously, refinement rails can only be used in the wake generator domain which is moving with the wake unlike the blade cascade. The resulting blade cascade domain is shown in black in Fig. 4.9 while the initial inlet domain is shown in orange. The interpolation of the solution obtained by Borbouse [18] on the cut domain is possible thanks to the periodic conditions imposed on the upper and lower boundaries.
Boundary conditions such as no-slip and adiabatic conditions on the blade surface are also identical to Borbouse's work.

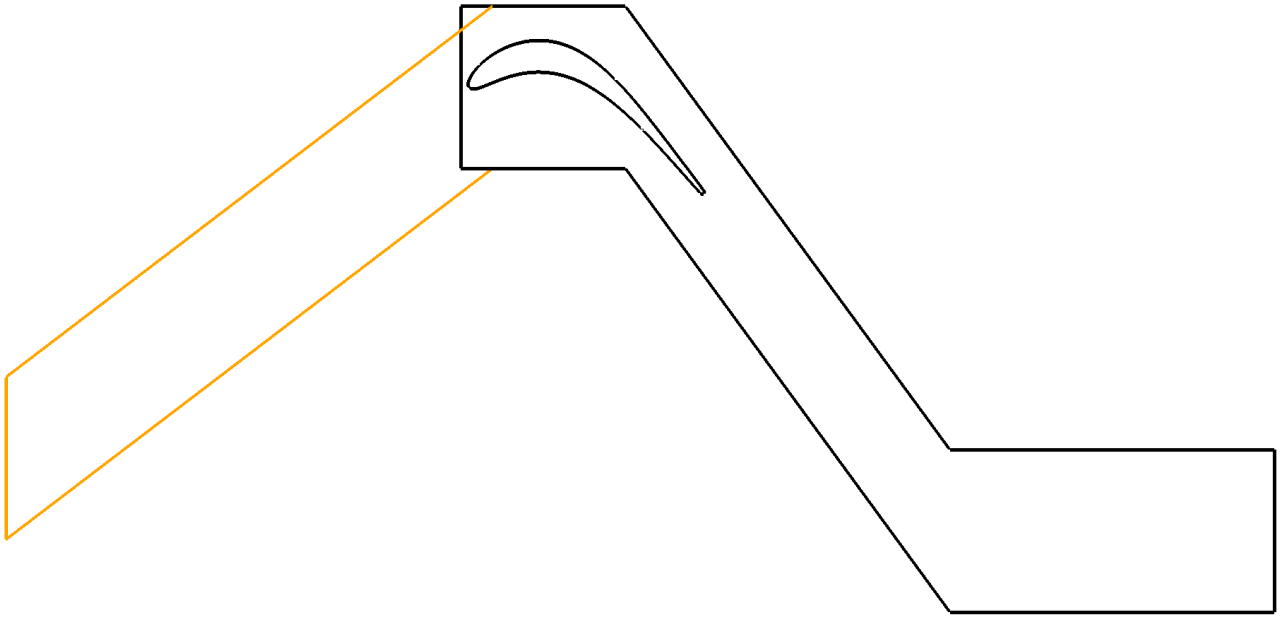

Figure 4.9: Blade cascade computational domain. In orange, the inlet of Borbouse's domain. In black, the cut domain used for the rotor-stator interaction simulation.

Mesh

The mesh on the blade cascade domain is the same as in Borbouse simulation, except in the inlet region and around the blade where the mesh element size is imposed to 2.5e-4 m to correspond to the size in the refinement rails of the wake generator. The mesh of the blade cascade used in this work is shown in Fig. 4.10.
Additional mesh refinement is applied at the LE to ensure element quality between the two boundaries: the inlet and the blade.

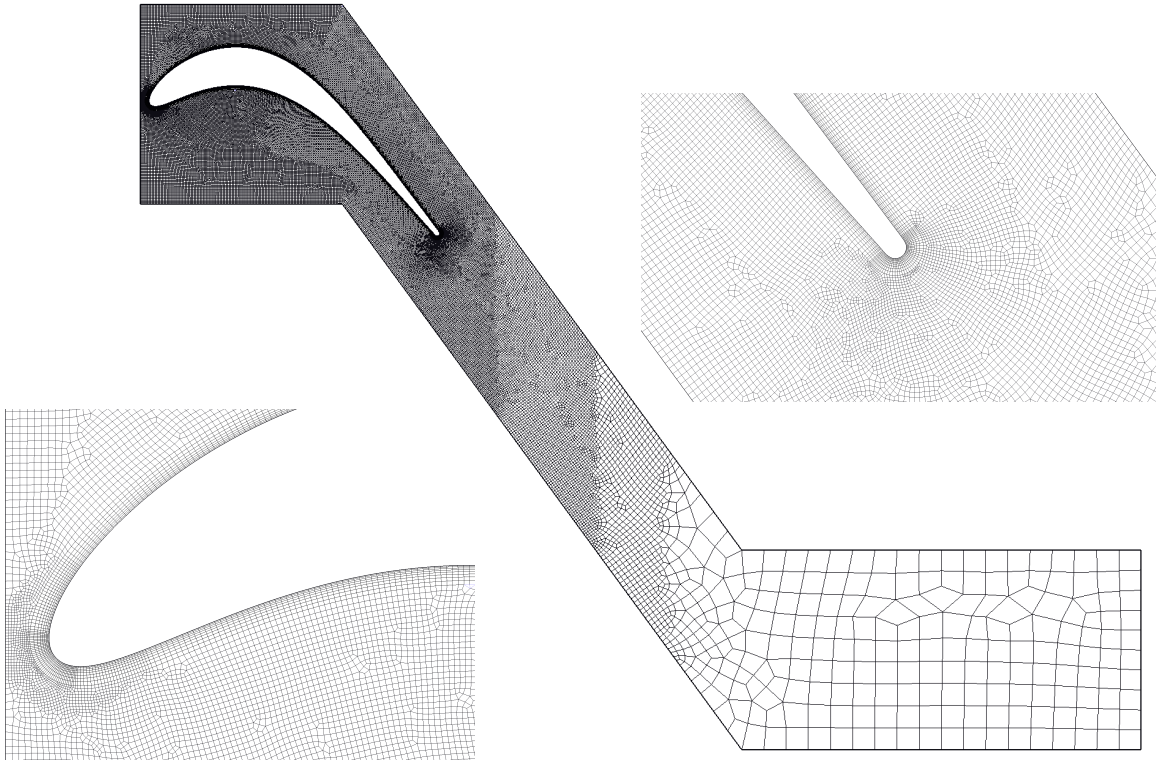

Figure 4.10: Mesh of the blade cascade domain.

4.2.3 Wake generator and blade cascade assembly

The coupling of the two domains, the wake generator with the blade cascade, is achieved by the use of non matching connection, see section 4.1.2. At each time-step, the solution of each domain is first computed separately in its own frame of reference. Then the information from one domain is given to the other and vice versa. Fig. 4.11 shows the coupling of the two domains.

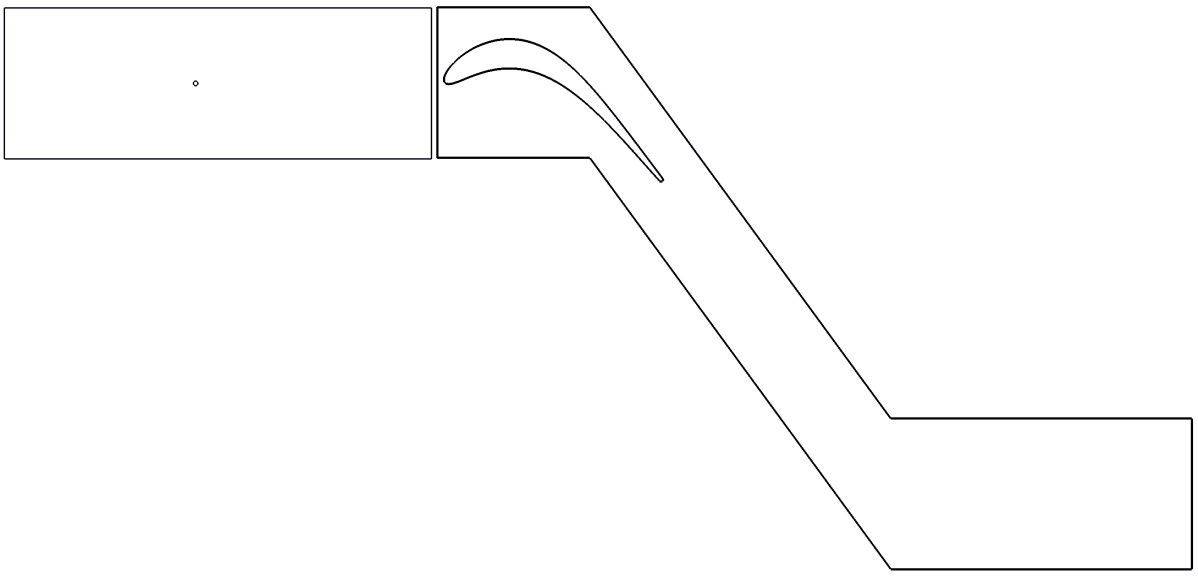

Figure 4.11: Wake generator and blade cascade coupling.

In the absolute frame of reference, the wake generator domain (the rotor) is translating downwards while the blade cascade domain (the stator) is static. Because of the periodic boundary conditions on top and

bottom boundaries of the wake generator, the part of the domain of the wake generator that is below the inlet of the blade cascade can be viewed as shifted up again, resulting in an infinite wake generator passage in front of the static blade cascade. This situation is illustrated by Fig. 4.12.

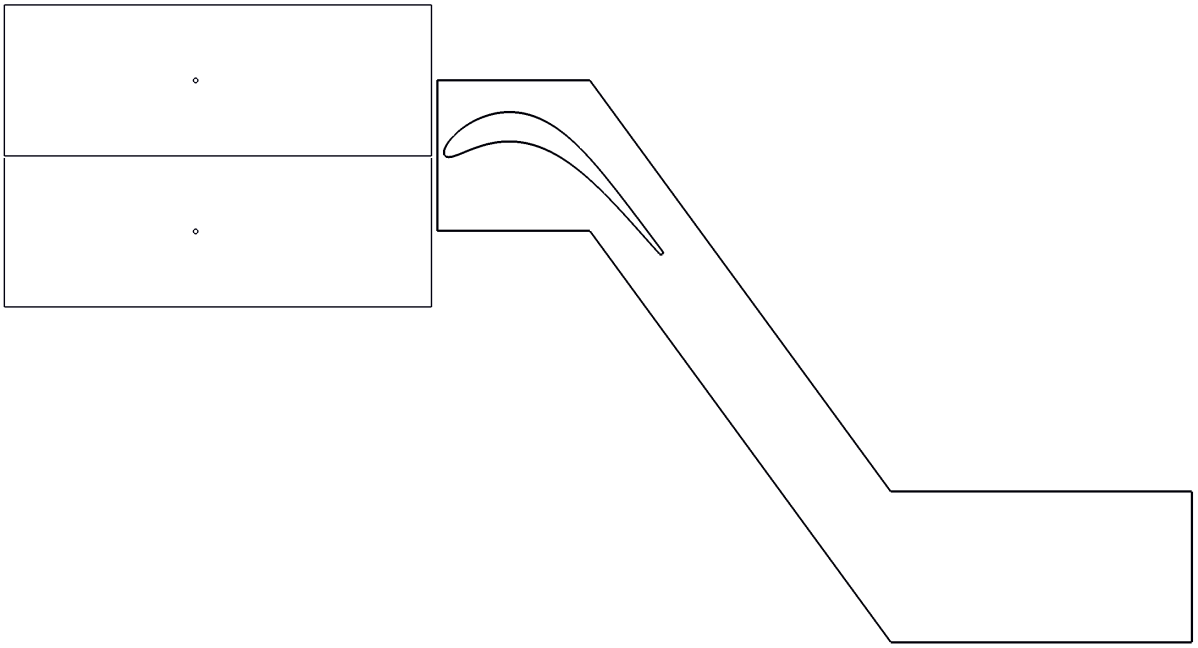

Figure 4.12: Infinite wake generator passage in front of the static blade cascade.

When the two domains are coupled, the total flow conditions are applied at the inlet of the wake generator, as described in section 4.2.1 and the static pressure condition is applied at the outlet of the blade cascade, see section 4.2.2. No boundary conditions are needed at the junction of the two domains.
The final mesh on both domains with the 3D view of the numerical setup in Fig. 4.3 is shown in Fig. 4.13. Note that the actual thickness of the computational domain in the span-wise direction is only 7% of the blade chord and not 56% that are shown in Fig. 4.13 for visibility purposes. The resources used by the final mesh are gathered in Table 4.3.

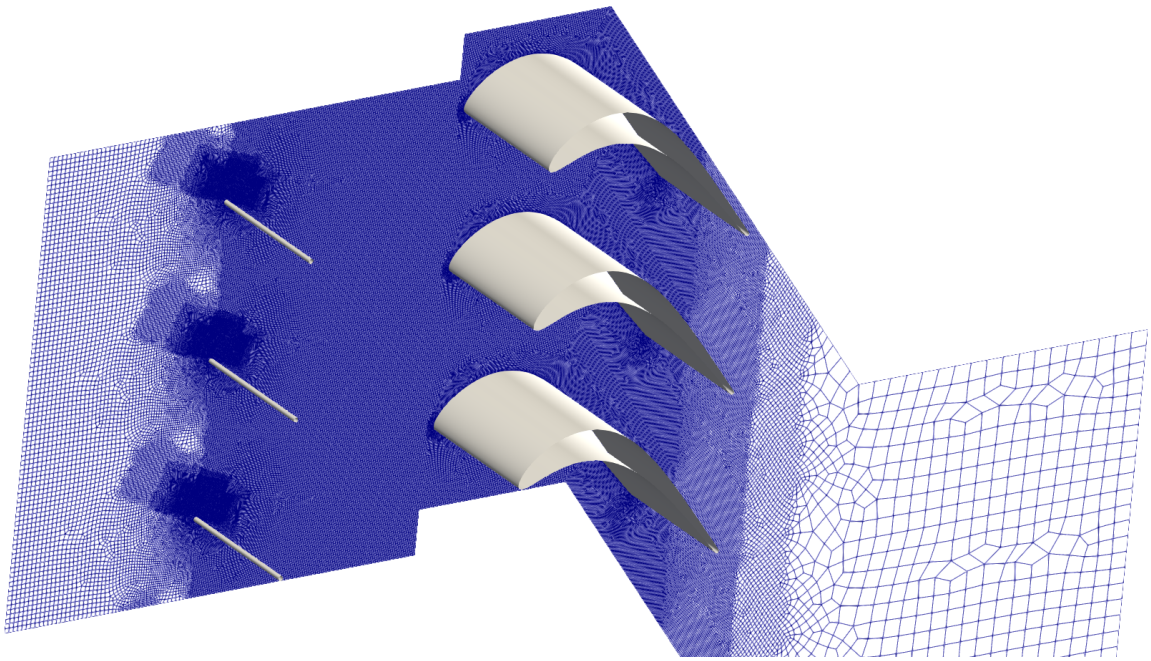

Figure 4.13: 3D view of the full computational domain.

Domain	Nbr of elements	Nbr of partitions	Nbr of nodes	Elements/CPU
Wake generator	2,602,500	2560	20	1016
Blade cascade	1,355,130	1280	10	1058
Total	3,957,630	3840	30	-

Table 4.3: Final mesh resources.

The meshes have been designed to match the demand of the strong gradient regions, but also to have a similar number of elements per CPU for both domains to optimize the parallel computation. That way, each time-step is computed with roughly the same time for both domains without having one domain waiting for the slower one to finish.

4.3 Schemes and solvers

As introduced in section 2.2 about the numerics in the Theoretical background chapter, the problem considered here involves transonic unsteady compressible flows. The unsteady solution is approximated using the discontinuous Galerkin method and a time marching method with implicit temporal discretization using the second order backwards differencing formula BDF2. The viscosity of the fluid is obtained from Sutherland's law. The Riemann solver that worked for the entire simulation is the Lax-Friedrichs solver, see transient solution in section 5.1. The absence of domain specification for the Riemann solver forces the use of the more dissipative Lax-Friedrichs solver one the wake generator as well as for blade cascade where it is not needed.
The solution is first initialized with p0 and then p3. Thus, the discontinuous Galerkin method is 4th order accurate. It results $4^3 = 64$ interpolation points so 64 degrees of freedom (DOFs) per equation and per element. With the final mesh shown in Fig. 4.13, the number of DOFs is 253M.
The final non-linear equations system is solved using the Newton-GMRES algorithm with a Jacobi preconditioner. The maximum number of iterations for the GMRES algorithm is increased from 30 to 50, and from 5 to 10 for the Newton solver. The FreezeJacobianMatrix parameter varies during the transient solutions but is finally fixed to 10. The final time-step used is 1e-8s.

5 Transient solutions

As described in the previous section 4.3, the method used is a time marching method, with a transient phase between the imposed initial solution at $t = 0$, and the established flow solution. Generally, the transient phase of a numerical simulation is not of great interest and is just mentioned without going into details. In this work however, the transient phase is interesting as several problems with important consequences were encountered, and to which answers were found. Those problems and answers are described in the following sections with first the wake generator domain, and then the two domains coupled. No transient phase for the blade cascade domain is shown in this work as the solution on this domain is interpolated from the one obtained by Borbouse [18].

5.1 Wake generator

The transient solution of the wake generator domain is decomposed into four main steps: the initialization of the solution with order 0 polynomials (p0), the transition from p0 to p3, the stabilization of the p3 solution and the correction of the inlet flow angle. The following section describes in more details those four steps, the related meshes and a global temporal view of the transient solution. Afterwards, the transonic flow simulation issues are discussed along with the answers provided in this work.

5.1.1 Main steps of the transient solution

Initialization with order 0

5e-5s: Initialization of the simulation. The relative Mach number shows the starting of the wake behind the cylinder. As the flow is not established yet, the wake is following the same direction as the movement of the bar.

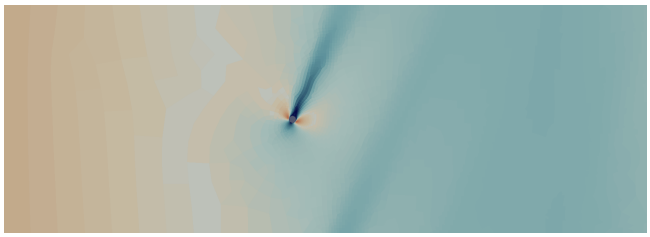

1e-3s: The pressure wave is coming from the left, ie the inlet boundary condition, and travels across the domain. The wake is already in its stable direction that can be estimated by the velocity triangle with the cylinder translation and the incoming flow with inlet flow angle.

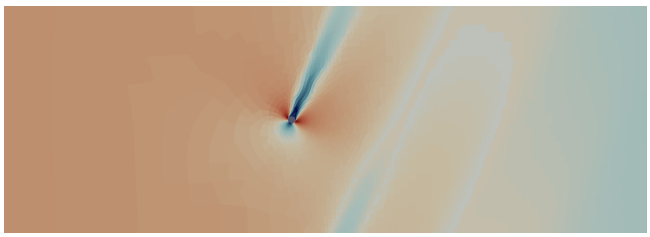

1.5e-3s: The pressure wave is still traveling back and forth in the domain.

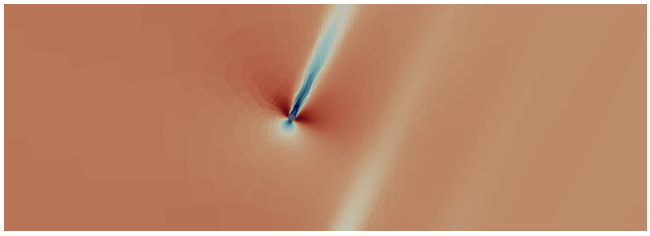

1.035e-2s: The solution is stabilized and the traveling pressure wave has vanished.

Transition to order 3

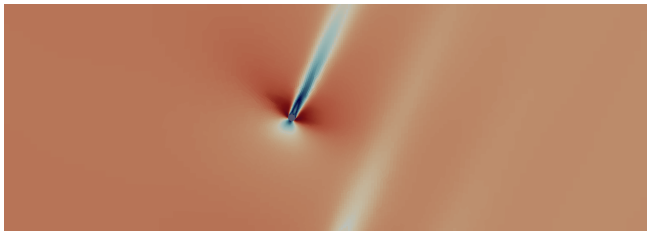

1.036e-2s: Change of mesh to initiate the transition from p0 to p3. On either side of the cylinder, the velocity increases.

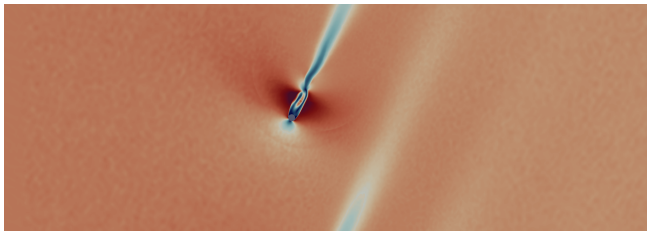

1.0396e-2s: Transition to p3: the no-slip condition is well imposed and the surface flow changes, leading to the initialization and growth of a separation bubble behind the cylinder. Now, the velocity increases on either side of the bubble. A velocity perturbation (VP) of 10% is added to speed up the transition from 2D to 3D flow to damp large discontinuities.

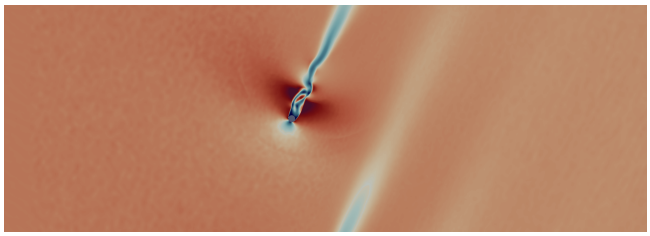

1.0406e-2s: Start of the separation bubble break and shock apparition attached to the bubble. Artificial viscosity (AV) is added in order to increase the thickness of the shock, see AV in section 4.1.2.

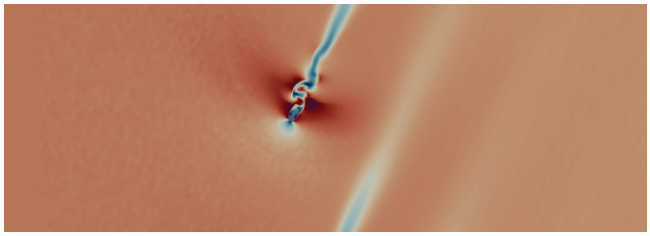

1.0415e-2s: Break of the separation bubble into several vortices with high velocity parts coming from the acceleration on either side of the cylinder and the bubble.

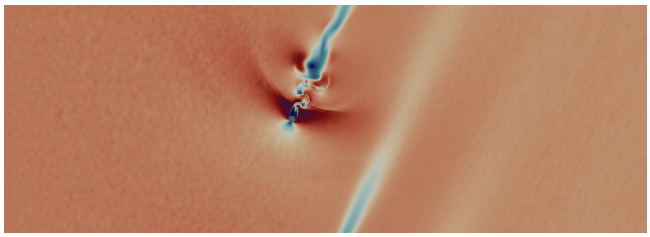

1.0435e-2s: The strong vortices coming from the break of initial separation bubble are moving away from the shock. They are denoted as spurious vortices as they are not part of the established flow. A Z-shaped sponge layer (ZSL) is applied to damp them, see subsection 5.1.3.

Stabilization with order 3

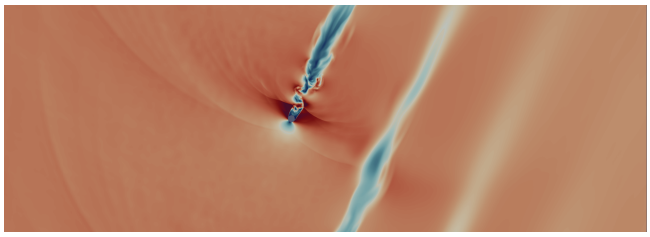

1.0568e-2s: Stabilization of the wake close to the cylinder. Removal of the ZSL as the spurious vortices have vanished. Establishment of the Karman vortex street and start of the slow periodic motion of the shock.

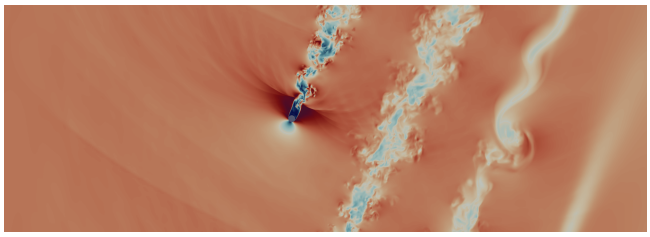

1.07535e-2s: After removal of the ZSL, the wake of the cylinder continues to extend towards the outlet with increasing width and decreasing turbulent intensity.

Inlet flow angle correction

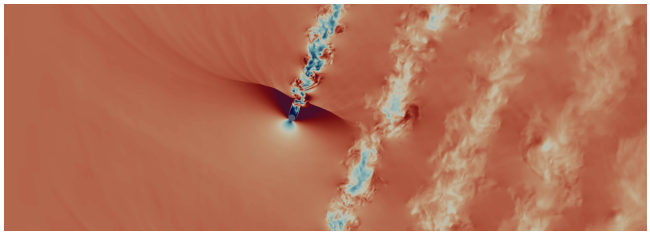

1.21825e-2s: Wake and shock fully established. Application of an inlet sponge layer in order to remove any possible reflections on the inlet boundary, see subsection 5.1.3. The change of inlet flow angle from 36.3° to 42.47° is completed, see incidence angle correction in section 3.3.1.

Meshes

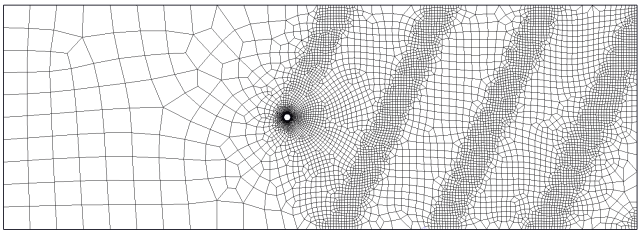

0 → 1.035e-2s: 200,940 elements.
Mesh for the initialization of the solution with order 0. The refinement regions in the direction of the wake are called “refinement rails”.

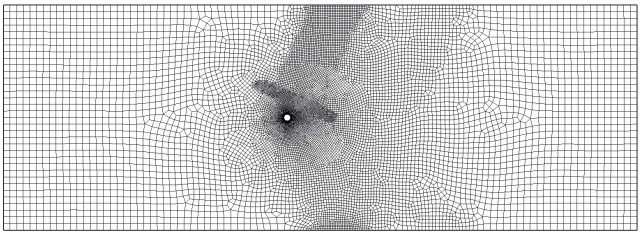

1.035e-2s → 1.0597e-2s: 366,420 elements.
Mesh for the transition from order 0 to order 3 with ZSL, see subsection 5.1.3. Mesh refinement in the shock region, first refinement rail and refinement of the whole domain to capture the waves that are travelling in all directions.

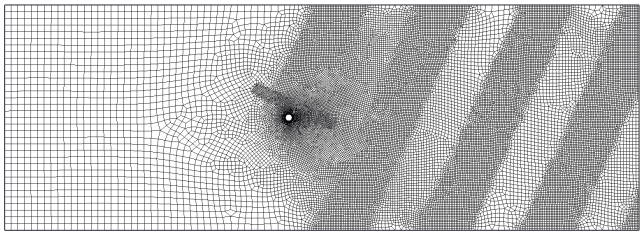

1.0597e-2s → 1.1582e-2s: 772,770 elements.
Mesh after the removal of the ZSL and starting of the Karman vortex street. The refinement rails are enlarged to better capture the wake.

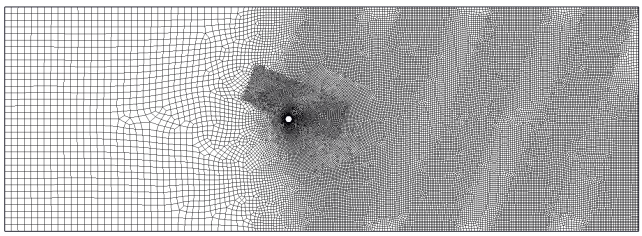

1.1582e-2s → 1.21945e-2s: 1,037,730 elements.
Mesh with an increase of the shock refinement region because of the shock motion, refinement between the refinement rails as the actual wake becomes thicker, and change of the angle of the refinement rails according to the corrected inlet flow angle.

Global temporal view

In order to follow the time evolution of the simulation, an estimation of the angle of the wake is obtained by looking at the momentum convective fluxes on the surface of the cylinder:

$$\alpha_{\text{estimate}}(t) = \arctan\left(\frac{\text{Momentum convective flux along y }(t)}{\text{Momentum convective flux along x }(t)}\right). \tag{5.1}$$

Those fluxes are non zero despite the no-slip boundary condition as the cylinder is translating in the absolute frame of reference. So, the cylinder applies some momentum to the flow.
Fig. 5.1 shows the estimate wake angle time evolution as the simulation progresses. First, the initialization of the flow with p0 in blue. Then, the transition from p0 to p3, the stabilization and the flow angle correction respectively in orange, green and red. Fig. 5.2 offers a closer look on the last three steps of the transient solution.

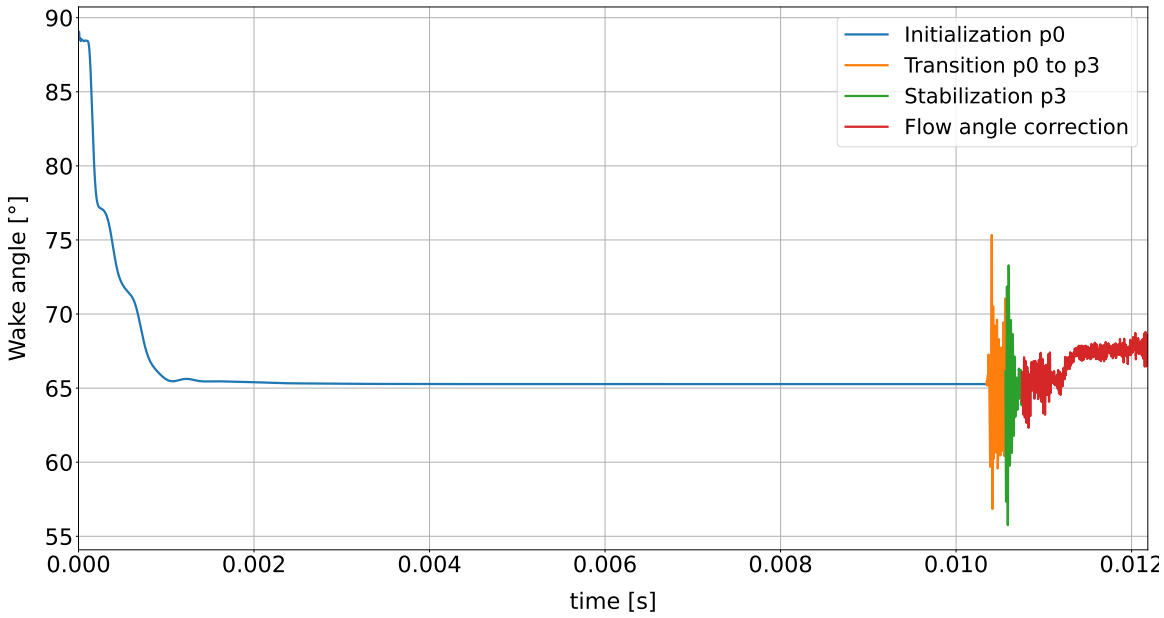

Figure 5.1: Estimate wake angle, complete time evolution.

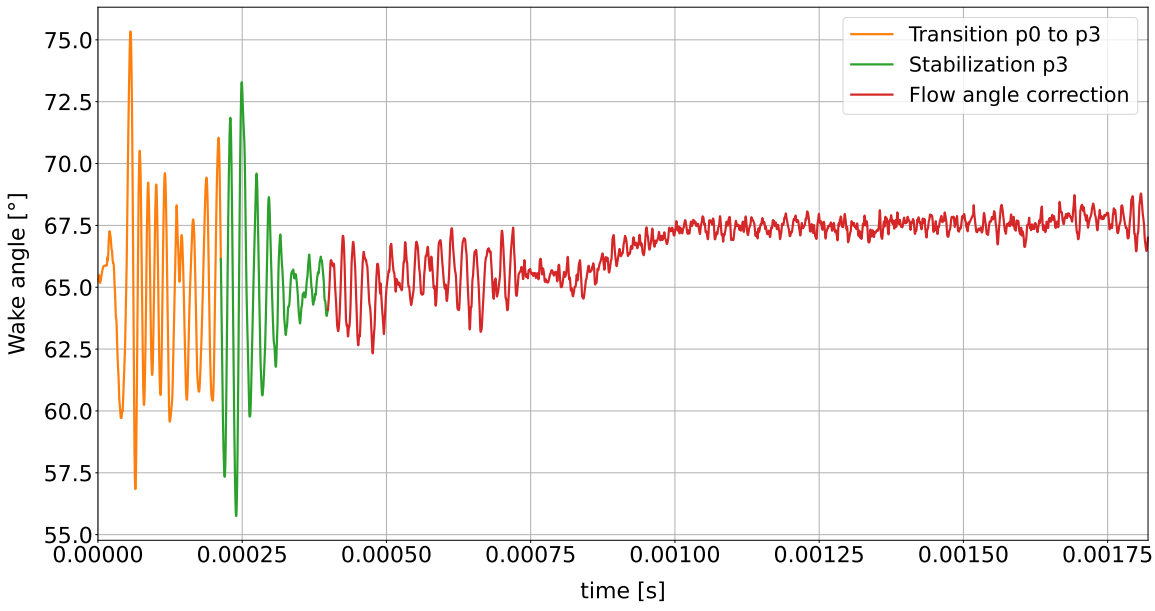

Figure 5.2: Estimate wake angle, three last steps time evolution.

Several observations can be made:

- The predicted wake angle computed for the refinement rails is confirmed by the simulation.
- The p0 solution converges to a steady flow angle around which the p3 solution is oscillating, before the change of inlet flow angle.
- The second wake angle from the change of inlet flow angle is also well predicted.
- Around t=0.00075s in Fig. 5.2, the flow is stabilized and even with the change of inlet flow angle, the amplitude of the wake oscillations remain small. That concludes the transient phase of the wake generator solution.

5.1.2 Transonic flow issues and remedy tools

As described in section 2.1.4, this case of flow around a circular cylinder at Re = 70k and M = 0.7 implies transonic flow behaviour and the presence of shocks. Those shocks induce discontinuities in the solution, that are moving with time, and can be located everywhere, not only at the boundary of two elements. Indeed, at the boundary of two elements, the DGM would manage easily such discontinuities. Those large discontinuities inside elements however, are difficult to manage by the solver and may lead to its inability to continue the simulation, see Fig. 5.3. A strategy to carry such a complicated simulation is to reduce the time-step, refine the mesh and allow more GMRES and Newton iterations at each time-step. All these approaches increase the computational cost and time. In this work, the minimum time step is set to 1e-8s and the number of mesh elements of the order of 1M which requires 8 nodes of 128 CPUs each on the Lucia cluster. The maximal GMRES iterations is set to 50 and 10 for the Newton iterations. With those constraints on the user defined parameters, several additional tools were necessary to carry out the simulation, see section 4.1.2:

- Sponge layer (SL)
- Velocity perturbation (VP)
- Artificial viscosity (AV)
- More dissipative flux function : Lax-Friedrichs (Lax) instead of Roe

By trial and error, the amplitude of the VP is fixed to 10% and the three parameters of the AV are [1 -3 1]. The penalty factors defining the ZSL and the SLIN are described in section 5.1.3.
In order to compare those different tools and their impact on the simulation, the wake angle time evolution is presented in Fig. 5.3.
For the comparison between the tools used, the mesh is the one in Fig. 4.6, without all the refinements rails, and the time-step is fixed to 1e-8s.
The simulation presented in the previous section is added to the figure (Combined) as a reference. As described previously, this “Combined” simulation is run with all the tools. It must be noticed that its simulation conditions are not the same with varying meshes and time-steps.
Fig. 5.3 highlights that the simulation with the Roe flux function is the most sensitive to transonic flow behaviours. Tests have been conducted with Roe + AV and Roe + AV + 10% of entropy fix (EF) but they all lead to failure at about the same simulation time as shown in Fig. 5.3 for Roe. The next most sensitive one is the simulation with Lax-Friedrichs and the velocity perturbation, then Lax-Friedrichs alone, Lax-Friedrichs and the Z-shaped sponge layer. The simulations “Combined” and Lax-Friedrichs with artificial viscosity are the only ones that can manage the complexity of the transonic flow.
The following figures in Fig. 5.4 show the impact of these different tools on the solution. Each figure shows the final state of the simulation when the solver is unable to go any further. In the case of Lax + AV, the figure shown is the one at time t=1.25e-4s and at t=1.7e-4s zoomed out.

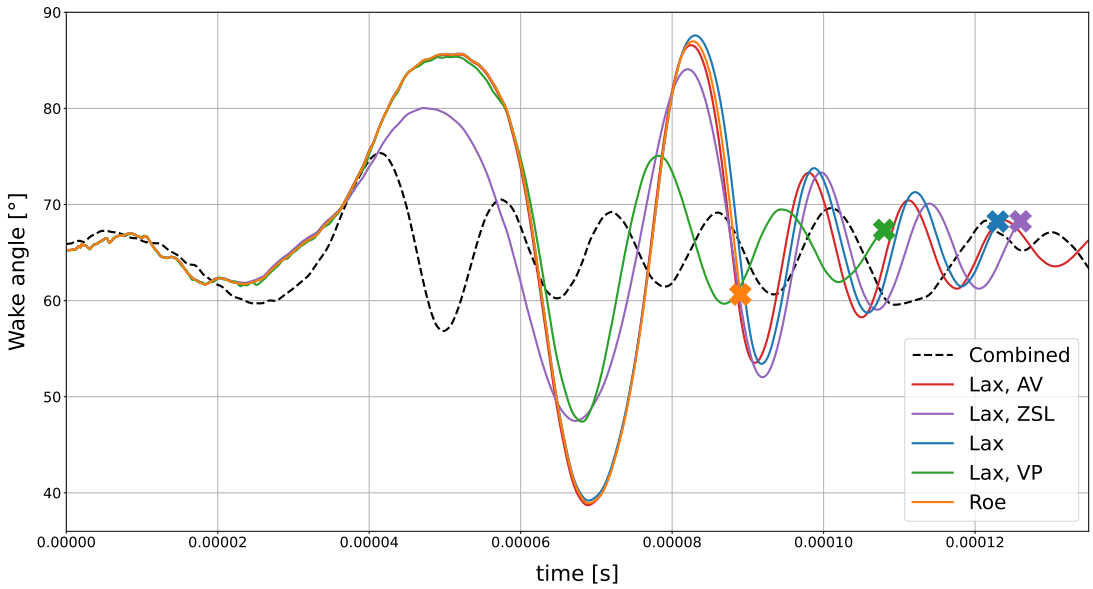

Figure 5.3: Comparison of the time evolution of the wake angle, for the different tools used: artificial viscosity (AV), Z-shaped sponge layer (ZSL), velocity perturbation (VP) and Riemann solvers Roe and Lax-Friedrichs (Lax). The crosses indicate the final state of a simulation when the solver is unable to go any further. In dotted black line (Combined), the start of the simulation with p3 presented in section 5.1.1.

Fig. 5.4 (a) shows that as soon as the shock leaves the most refined mesh region (see last mesh in section 5.1.1), the solver is not able to go any further. The other figures show that the flux function Lax-Friedrichs is more robust, as all cases are able to go further in the simulation. The Roe flux function is better than the LF as LF is much more dissipative, but all attempts to go back to Roe after the stabilization of the wake have failed, see section 2.2.3 about the Roe issue with transonic flows.
Fig. 5.4 (b) shows that the VP made the transition to 3D flow faster, reducing the intensity of the shock and also increasing considerably the dissipation of the spurious vortices (SV) without a sponge layer.
Fig. 5.4 (c) shows that with Lax alone, the SV are dragged along by the flow without real damping.
Fig. 5.4 (d) Shows the radical effect of the sponge layer on the solution: all the SV have vanished. The position of the ZSL spared the shock as intended.
Fig. 5.4 (e) shows that the simulation can be carried out with Lax + AV only. However, like in the case of Lax alone, the SV are not damped and are dragged along by the flow. The refinement rails are in the same direction than the propagation of the SV and are able to capture them. However, Fig. 5.4 (f) shows that those SV are moving away from the central wake axis and even leaving the refinement rails. Nevertheless Lax + AV seem to allow the solver to continue the simulation further.
In the simulation that has been carried out to the fully established wake, all the available tools such as Lax, AV, VP and ZSL have been used together, in order to benefit from all advantages. Furthermore, it allowed to increase the time-step from 1e-8s to 1e-7 for a part of the simulation which lowered considerably the computational cost and time.
Finally, all figures in Fig. 5.4 indicate that Lax-Friedrichs is able to take care of the transonic behaviour of the flow in the wake region however, AV must be added to take care of the shock combined with a good mesh refinement. Table 5.1 sums up the comparison of the numerical tools.

Numerical tool	**Shock start**	**SV removal**	**Success**
Roe, Roe + AV, Roe + AV + EF	×	-	×
Lax + VP	✓	✓	×
Lax	✓	×	×
Lax + ZSL	✓	✓	×
Lax + AV	✓	×	✓

Table 5.1: Numerical tools comparison.

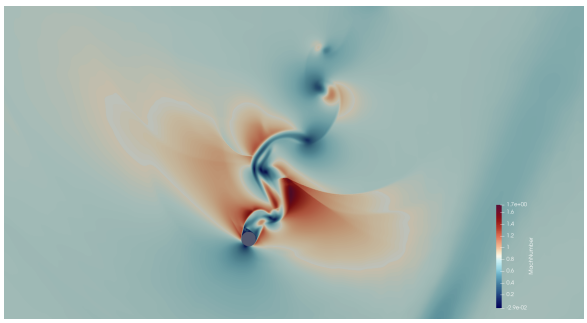

(a) Mach number for the Roe simulation.

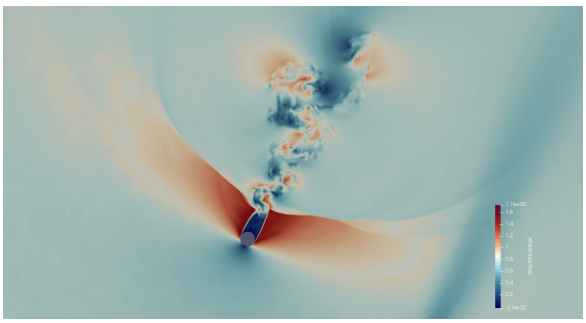

(b) Mach number for the Lax + VP simulation.

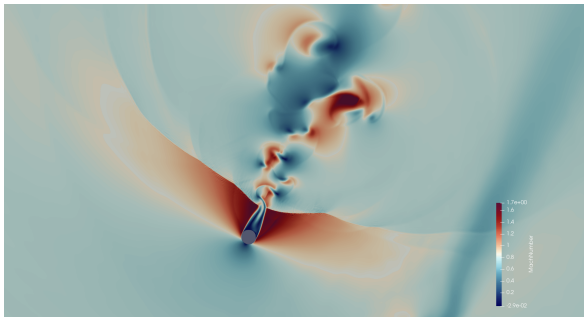

(c) Mach number for the Lax simulation.

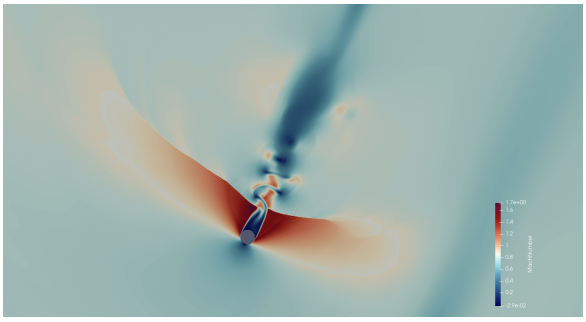

(d) Mach number for the Lax + ZSL simulation.

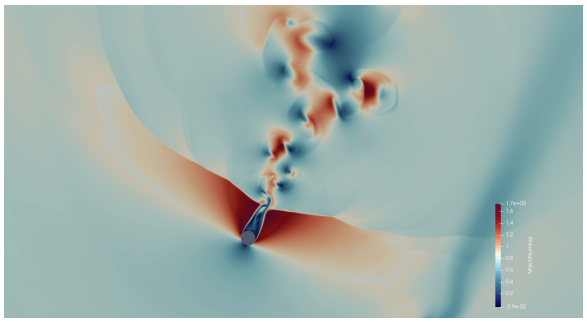

(e) Mach number for the Lax + AV simulation at t=1.25e-4s.

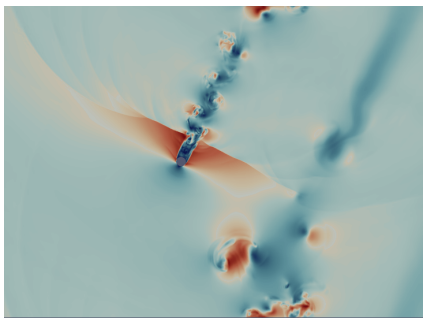

(f) Mach number for the Lax + AV simulation at t=1.7e-4s zoomed out.

Figure 5.4: Final state of the simulation with the different tools used.

5.1.3 Sponge layers

Z-shaped sponge layer (ZSL)

In order to rapidly damp the spurious vortices, a Z-shaped sponge layer is applied at the transition from p0 to p3. The value of the penalty factor σ defines the Z-shape with the following expression:

$$\begin{aligned}\sigma =& 5000 \times (1+\tanh\big(500 \times (y + x/\tan(\alpha_w) - 5 \times 0.001/\sin(\alpha_w))\big)) \\ & \times (1+\tanh\big(500 \times (-y + x \times \tan(\alpha_w) + 6 \times 0.001 \times \sin(\alpha_w) \times \tan(\alpha_w))\big)) \\ & \times (1+\tanh\big(500 \times (y + x \times \tan(\alpha_w) - 6 \times 0.001 \times \sin(\alpha_w) \times \tan(\alpha_w) + g)\big)) \\ & \times (1+\tanh\big(500 \times (y - x \times \tan(\alpha_w) - 6 \times 0.001 \times \sin(\alpha_w) \times \tan(\alpha_w) + g)\big)) \\ & + 40000 \times (1+\tanh\big(500 \times (-y + x \times \tan(\alpha_w) + 6 \times 0.001 \times \sin(\alpha_w) \times \tan(\alpha_w) - g)\big)),\end{aligned}$$

with the pitch $g = 0.03295$ m and the estimated wake angle $\alpha_w = 65°$.
Fig. 5.5 shows the resulting Z-shaped sponge layer. The center of the cylinder is located at (0,0) in the XY plane. The SL is defined in order to respect the periodicity of the domain and apply the penalty factor on the solution progressively.

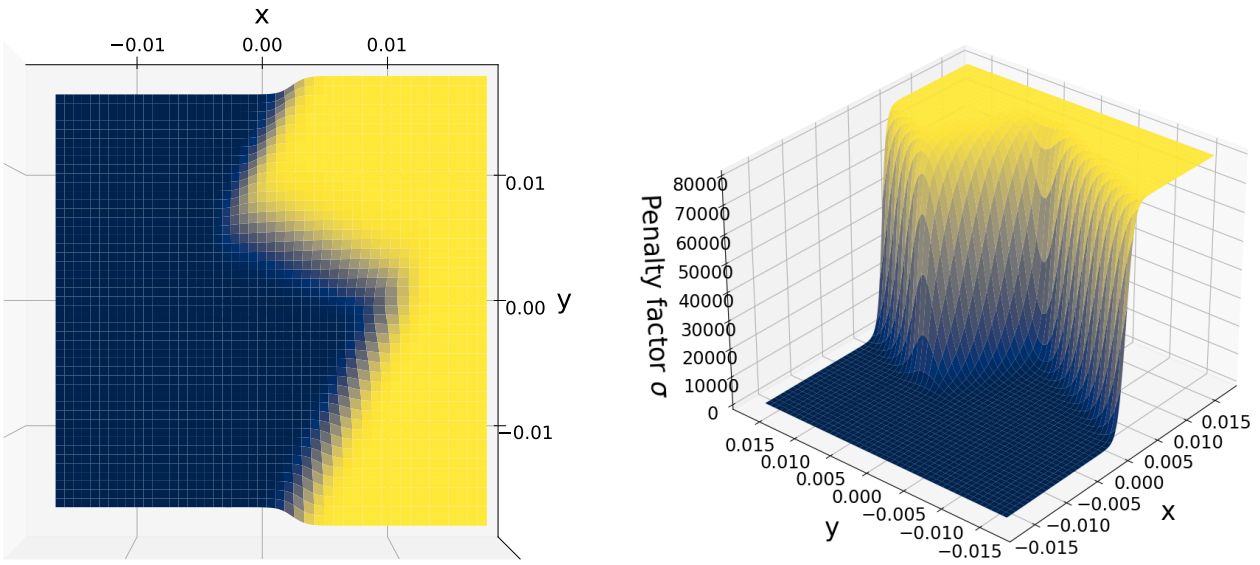

(a) Upper view.

(b) Side view.

Figure 5.5: Z-shaped sponge layer. The center of the cylinder is located at (0,0) in the XY plane.

Inlet sponge layer SLIN

As pressure waves move upstream, they reach the inlet of the computational domain and collied with the imposed total pressure condition. This pressure variation is converted into velocity by the boundary condition. As the velocity of the flow is not in the same direction as this velocity creation, the collision creates vorticity which is then carried downstream by the flow.
Fig. 5.6 shows the pressure waves coming from the interaction of the flow with the cylinder using the Schlieren method (gradRhoOverRho variable). Some of the waves are moving upstream and reach the inlet. Fig. 5.7 then shows the vorticity present in the domain. There is indeed spurious creation of vorticity at the inlet that is moving downstream. It can be noticed that this is not the case at the outlet, where only the static pressure boundary condition is applied. However, spurious wave pressure reflections are possible, as it can be seen at the outlet of the domain shown in Fig. 5.6.

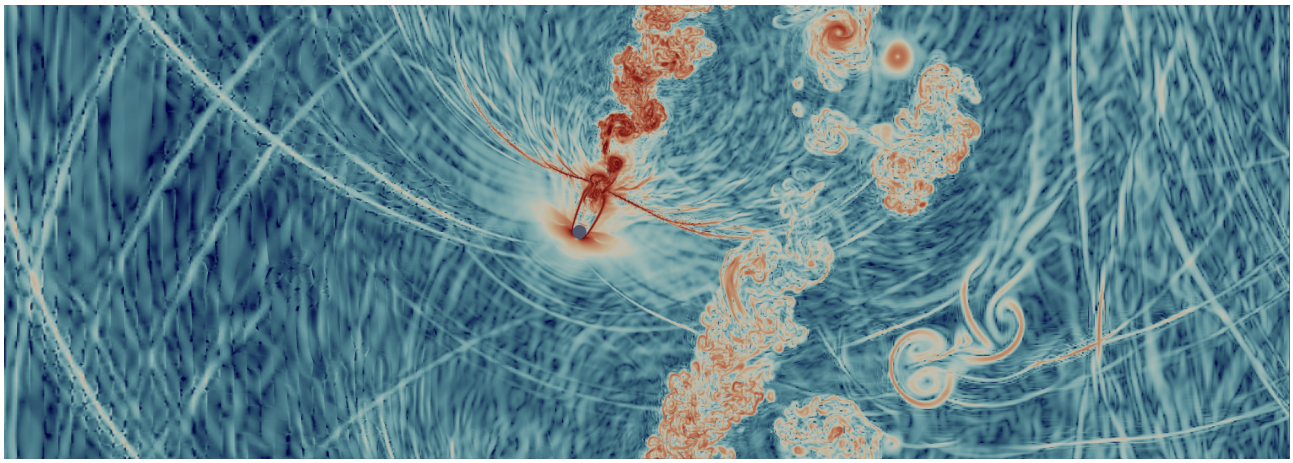

Figure 5.6: GradRhoOverRho, from the simulation with Lax + AV at t = 2.66e-4s, no sponge layer applied.

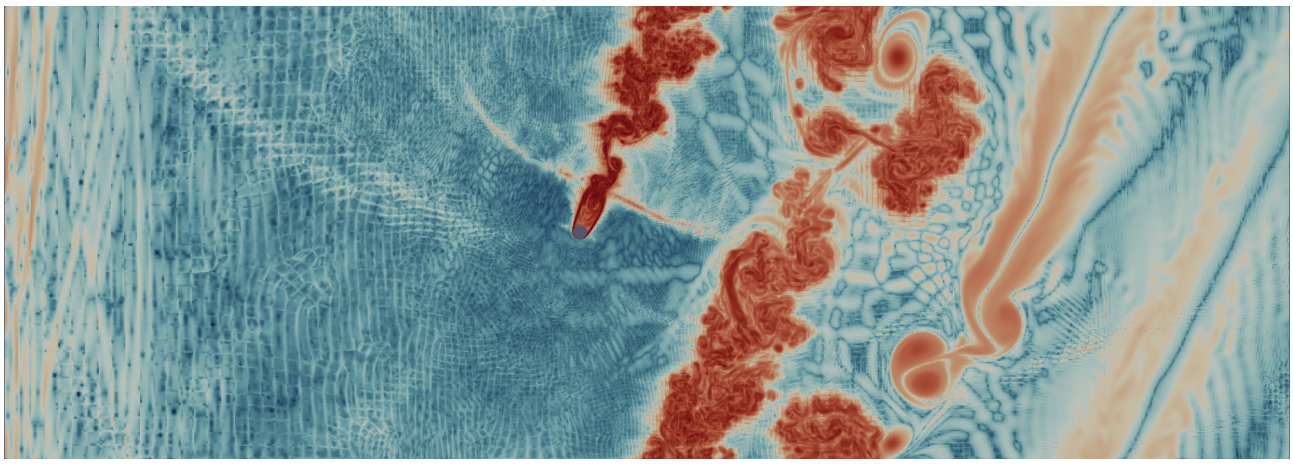

Figure 5.7: Vorticity, from the simulation with Lax + AV at t = 2.66e-4s, no sponge layer applied.

This spurious vorticity is called “reflection” on the boundary. To avoid any “reflections”, an inlet sponge layer is defined to damp all pressure variations travelling to the inlet, see Fig. 5.8 for the related penalty factor, which expression is given in (5.2).

$$\sigma = 50000 \times (1 + \tanh(500 \times (-x - c_{ax} \times 0.88 + (g/2)))) \tag{5.2}$$

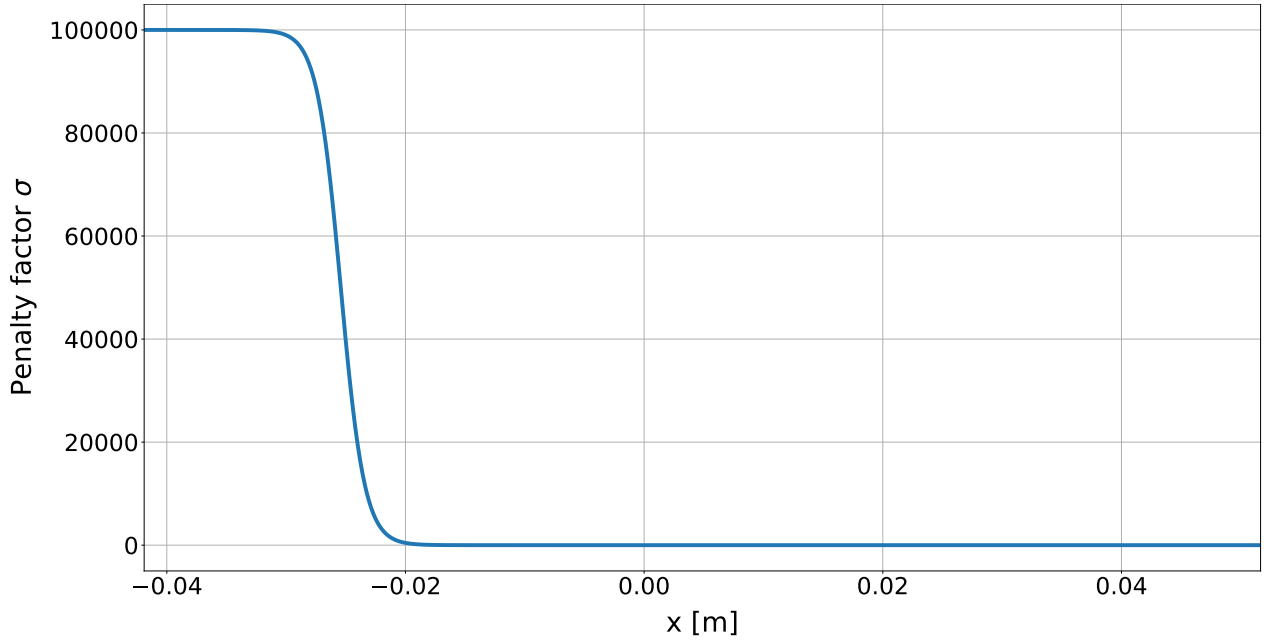

Figure 5.8: Penalty factor of the inlet sponge layer. In this case, the value of σ is constant along y.

5.2 Blade cascade with wake generator

In this section, the transient phase of the wake generator coupled with the blade cascade is presented. Like in the transient phase of the wake generator alone, several problems were encountered here.
The transient solution of the wake generator coupled with the blade cascade is decomposed in four steps:

- Coupling initialization.
- Synchronized restarts.
- Solver instability.
- Outlet sponge layer.

Those four steps are described in details in the following sections.

5.2.1 Two domains coupling

The coupling of the wake generator domain and the blade cascade domain is realized by an interface coded in ArgoDG, that allows non matching connection, see section 4.1.2.
The solution on each domain is initialized separately as described in section 4.2.3. On one hand, the solution of the wake generator alone obtained after the transient phase described in the previous section. On the other hand, the solution of the blade cascade alone, obtained by Borbouse [18]. As a result, the solution is different on both sides of the junction, see Fig. 5.9. A zoom on the junction is shown in Fig. 5.10a and Fig. 5.10b.

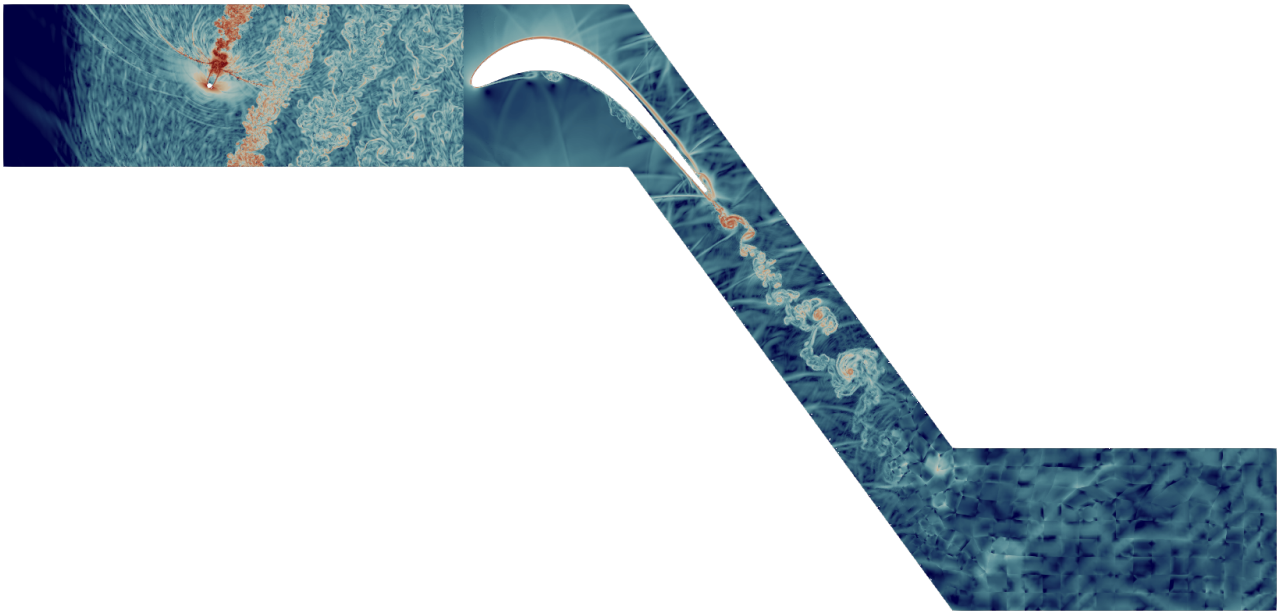

Figure 5.9: Schlieren of the computed solutions for the wake generator and the blade cascade before coupling.

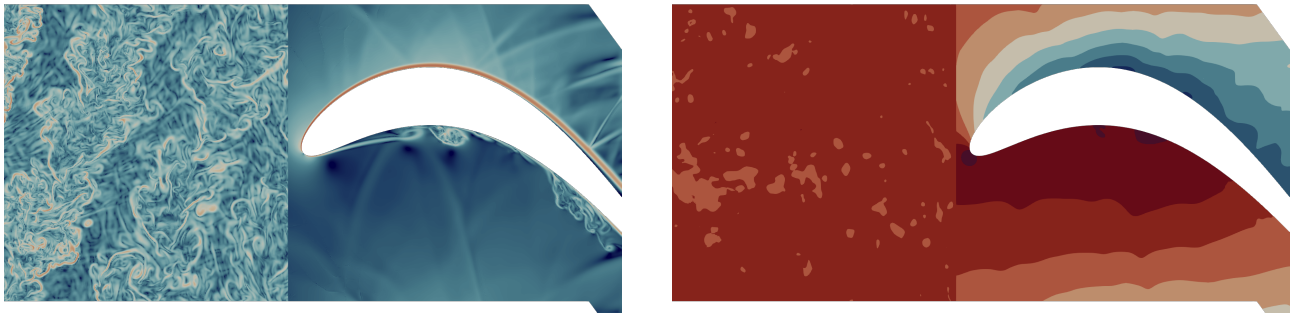

(a) Zoom on the junction, from Fig. 5.9.

(b) Static pressure isobars at the junction.

Figure 5.10: State of the flow before coupling.

Firstly, the generated wake has reached the outlet of the first domain while there is no turbulence at the inlet of the second domain before coupling, see Fig. 5.10a.
Secondly, for the initialization of the solution of the wake generator, the static pressure was imposed uniform at the outlet. Its value was fixed from the average of the static pressure at the inlet of the blade cascade alone. It results the strong pressure field difference shown in Fig. 5.10b and on the graph in Fig. 5.11.
At the coupling, the information from both domain travels into the other until the junction is stable. It happens in the form of two strong pressure waves going upstream and downstream, Those pressures waves are call adjustment waves, shown in Fig. 5.12.

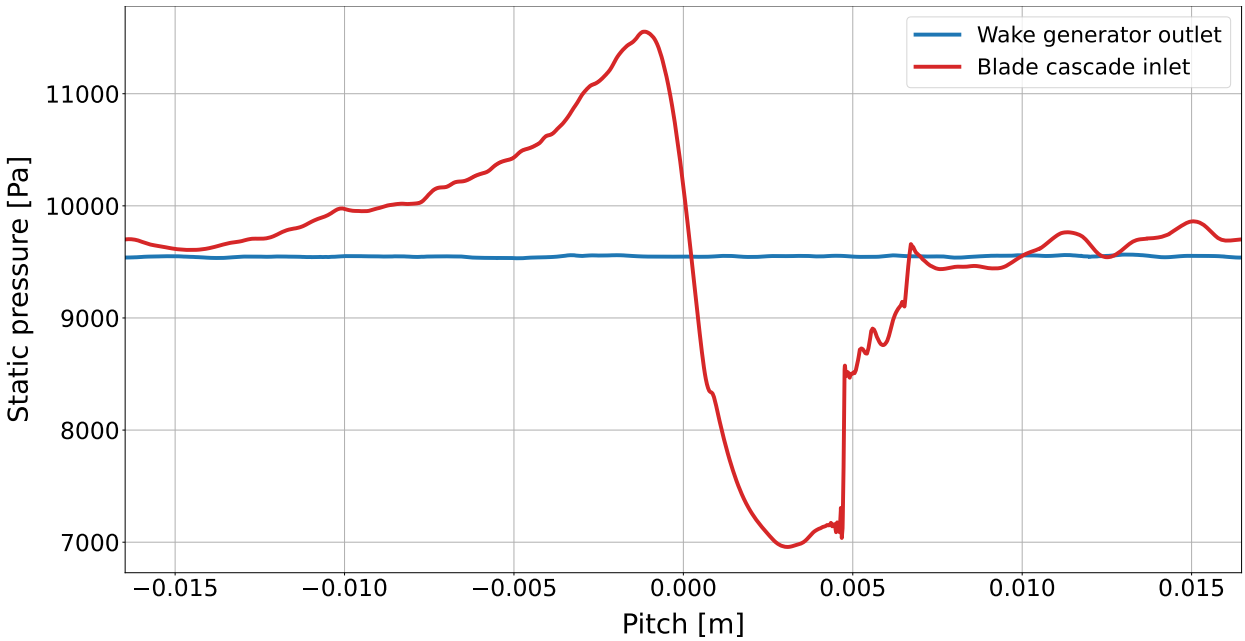

Figure 5.11: Static pressure in terms of the pitch, at the junction, from the wake generator side and from the blade cascade side before the coupling.

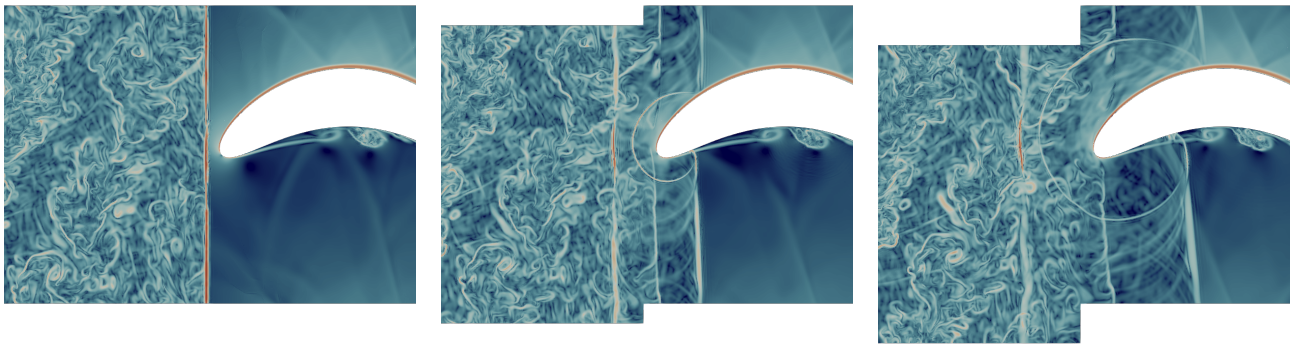

(a) 2e-7s after coupling. (b) 1.32e-5s after coupling. (c) 2.64e-5s after coupling.

Figure 5.12: Adjustment waves after coupling of the two domains.

Those adjustment waves are too large and prevent the GMRES solver to converge.
Thus, they must be damped in order for the solver to converge. Two ideas are considered: a reduction of the element order in the junction region, or the usage of a sponge layer also located in the junction region. Both ideas are developed hereafter.

Element order spatial variation

The element order can be defined by a function dependent on the spatial variables. It is applied in the absolute frame of reference without the possibility of specifying the domain to which it applies. It therefore applies to both domains without distinction. However, the wake generator and the blade cascade are defined in their own frames of reference with different origins, see sections 4.2.1 and 4.2.2 for more details. To make it work, a new domain with a new mesh for the wake generator is built, shifted upstream so that the two domains do not overlap anymore. However, WG solution is attached to the previous mesh which is still overlapping the blade cascade domain. So, at the restart of the simulation, the previous WG solution is translated to be interpolated of this new shifted mesh. ArgoDG allows to interpolate previous solutions on new meshes with translation and rotation transformations.

Unfortunately, after several trials with different parameters, it appears that there is a problem in the translation of the solution which may be related to an improper interaction with the periodic boundary conditions, see Fig. 5.13.
As the code of ArgoDG is the property of Cenaero, it can not be changed by an external user, so another solution is necessary.

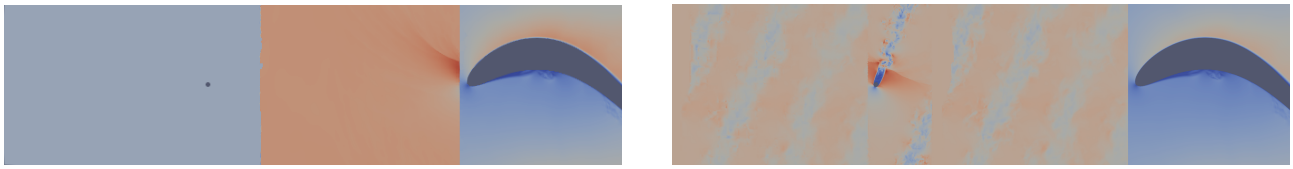

(a) Translation = [-0.0533232 0 0]

(b) Translation = [0.0533232 0 0]

Figure 5.13: Problem in the translation of the solution that might be related to an improper interaction with the periodic boundary conditions.

Sponge layers

As the idea of reducing the order to take care of the discontinuity at the junction of the two domains was not possible, sponge layers are used instead. Their shape is the same as the one presented in the previous section, see Fig. 5.8. Sponge layers are defined by domain so two must be define here, one at the outlet of the wake generator (SLW) and one at the inlet of the blade cascade (SLB).
Their full expressions are given below, each penalty factor is defined in their respective frame of reference:

$$\sigma_{\text{SLW}} = 25000 * (1 + \tanh(2500 * (x - 0.05165653333 + 0.005/6))), \tag{5.3}$$

$$\sigma_{\text{SLB}} = 25000 * (1 + \tanh(-2500 * (x + 0.005/6))). \tag{5.4}$$

This method worked as the sponge layers were able to sufficiently damp the adjustment waves. Those adjustment waves are rapidly decaying as they move upstream and downstream so the sponge layers were rapidly removed after 2640 time-steps of 1e-8s. The adjustment waves of the working simulation during the application of the sponge layers are visible in Fig. 5.12.
This usage of sponge layers applied on two different domains with respective frames of reference showed an inaccuracy in the code of ArgoDG: the specification of the domain in the sponge layer definition is not taken into account in the code. It resulted in the application of both SLW and SLB on each domain, see Fig. 5.14. SLW wrongly applied to the blade cascade is more visible than SLB on the wake generator as the flow is almost uniform upstream of the cylinder, whereas the wake is present downstream of the LE of the blade. Comparing Fig. 5.14a to Fig. 5.14b, one can see in the wake of the blade that it is as if the vortices leave trails behind them as they are being smoothed out by the sponge layer SLW.
This is not a problem as it is part of the transient solution and the sponge layers SLW and SLB were only briefly applied for the coupling initialization. However, in the case of the sponge layer applied at the inlet of the wake generator (SLIN), it is always applied. Fortunately, SLIN is applied far away from the cylinder centered at (0,0,0) and so, is applied outside of the blade cascade domain. The same reasoning can be done if a sponge layer is applied at the outlet of the blade cascade, and will be outside of the wake generator domain.

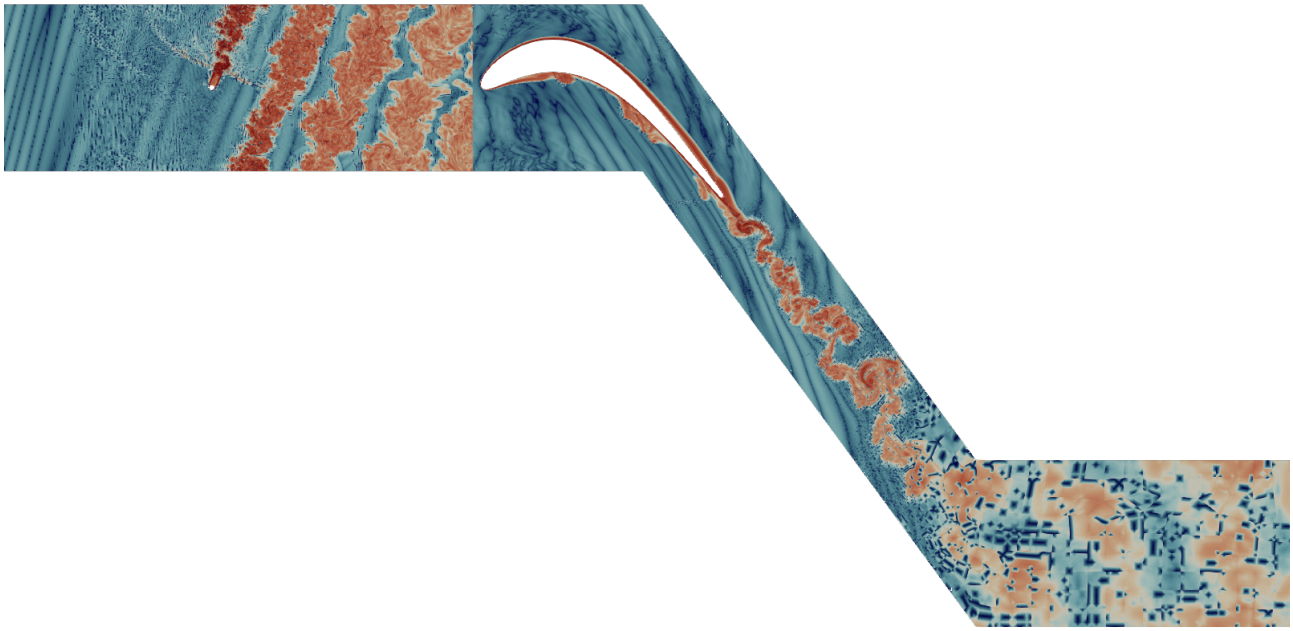

(a) Coupling initialization.

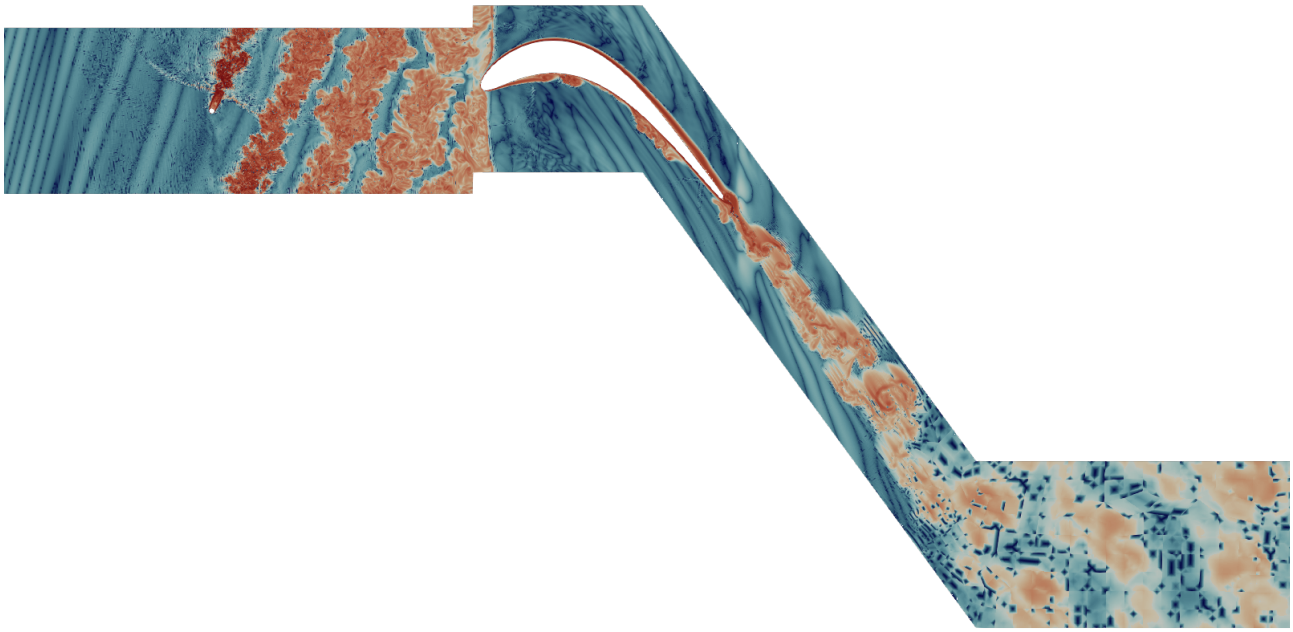

(b) Before removal of sponge layers, 2.64e-5s after coupling.

Figure 5.14: Enstrophy on both domains, at initialization of the coupling and just before the removal of the sponge layers around the junction.

5.2.2 Synchronized restart

Now that the coupling is successfully initialized, the next issue concerns restart synchronization.
The system of discretized NSE is solved by the Newton-GMRES method using multiple CPUs on Lucia. Those CPUs are shared with other users and the maximum reservation time is 2 days. This implies multiple restarts from previous calculation as one convective time takes about 4.4 days in the regular use of Lucia. This computation time is developed hereafter.
The convective time of the present problem is defined as the axial chord of the blade divided by the speed of the flow which gives 0.04761/150 = 3.174e-4s. With a time-step equal to 1e-8s, one convective time takes 31740 iterations. To give perspectives, on Lucia, with 1 node per partition and 1000 mesh elements per

partition, about 300 iterations are done per hour. That gives about 106 hours or 4.4 days to achieve one convective time.

In ArgoDG, 4 types of restart are possible:

- None, the simulation starts from the given initial solution at t = 0.
- Clean, the simulation starts from a computed solution interpolated on the domain, but all existing data are deleted. This mode is necessary for a change of mesh or folder.
- Full, same as Clean but all existing data are conserved and used in the next statistical calculations.
- Checkpoint, same as Full but allows the simulation to be restarted automatically.

For example, None restart was used at the start of the wake generator simulation with p0. After that, Clean restarts were used for mesh changes. When a change of mesh is done, the Clean restart mode is forced as the solution from the previous mesh must be interpolated on the new mesh.
However, the global time of the simulation is only stored in the Full restart mode and not in the Clean restart mode. This is a problem when it comes to two domains that move relative to each other. If the global time of the simulation is lost, the wake generator domain restarts at its initial position whereas its solution is the translated one. It results in the desynchronization of the solution of the wake generator with the one of the blade cascade.
Fig. 5.15 is an illustration of the desynchronization at the restart of a simulation. The displayed field are static pressure isobars. In (a), both domains are synchronized. In (b) the domains are desynchronized and in (c) is the view if the wake generator was at its initial position. One can see that the simulation is continuing with the wake generator at its initial position instead of the real translated position.

(a) At restart, t=0s, real domain position.

(b) After restart, t=2e-6s, real domain position.

(c) After restart, t=2e-6s, initial domain position.

Figure 5.15: Static pressure isobars of a test case with the two domains coupled. Illustration of a desynchronized restart.

To get around the storing time problem, it appears that the global time in a Clean restart is computed from the product of two parameters defined in the input file: *Iteration* at which the simulation restarts and *Timestep* of the new simulation. In order to get the right global time in a Clean restart, one must adjust those two parameters, with the freedom of changing the Timestep as long as Iteration is changed accordingly.
This particular case shows that the global time of a simulation should be stored and conserved throughout restarts, regardless of the type of restart.

5.2.3 Solver stability

Now that the two domains coupling works and the restarts are synchronized, the next issue concerns solver stability. As described in the transient solution of the wake generator in section 5.1, the computation of the solution was sensitive to strong discontinuities and required a Lax-Friedrich flux function and artificial viscosity. Mesh refinement in the shock region was also critical. All these aspects still apply in the two coupled domains case. However, the change in boundary condition at the outlet of the wake generator

has consequences such as small changes in flow velocity field, wake angle and shock behaviour. It results in the failure of the solver to continue the simulation with the same parameters that work for the wake generator alone. The exact reason for the solver's failure at time t = 4.4262e-4s has not been found, but several problematic aspects have been identified, such as spurious oscillations close to the shock and the application of AV in some vortices of the wake, see Fig. 5.16.

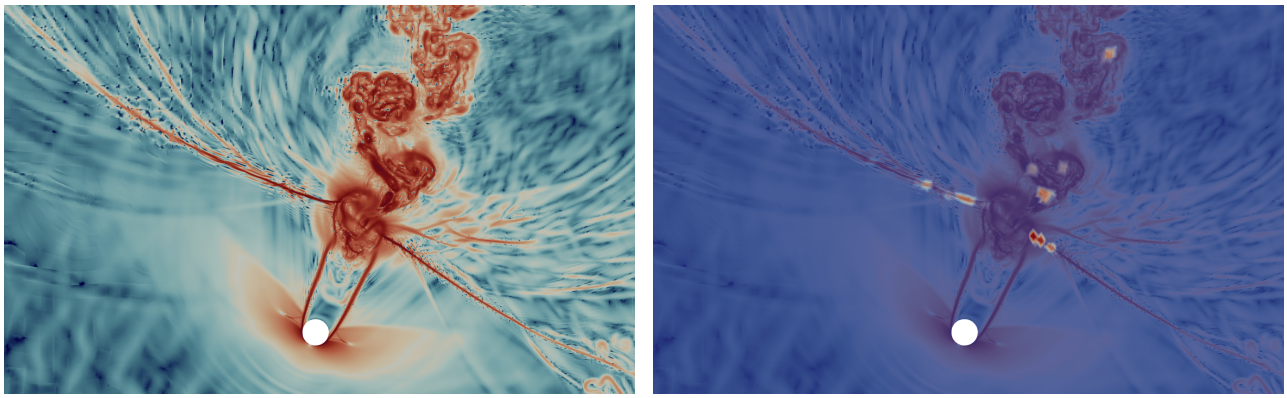

(a) Schlieren. (b) Schlieren and AV superposed.

Figure 5.16: Simulation of the two domains coupled, zoomed at the start of the wake of the translating bar (t = 3.6795e-4s). Schlieren on the left and Schlieren and AV superposed on the right.

The first aspect considered to improve the computation stability is to reduce the spurious oscillations in the vicinity of the shock. New meshes with increased refinement in the shock region were tested. This refinement greatly reduced those spurious oscillations, see Fig. 5.17b. In addition, a uniform mesh refinement of the whole region behind the bar is done to take into account the change of wake angle, which is no longer in the same direction as the refinement rails. The first and sixth versions of meshes are shown in Fig. 5.17a and Fig. 5.17b respectively. Five different meshes with increased refinement have been tested unsuccessfully before the test of the sixth version. However, the solver was still unable to advance to the next time-step even with the sixth improved version of mesh and a reduction of the time-step from 2e-8s to 1e-8s, the smallest allowed time-step.

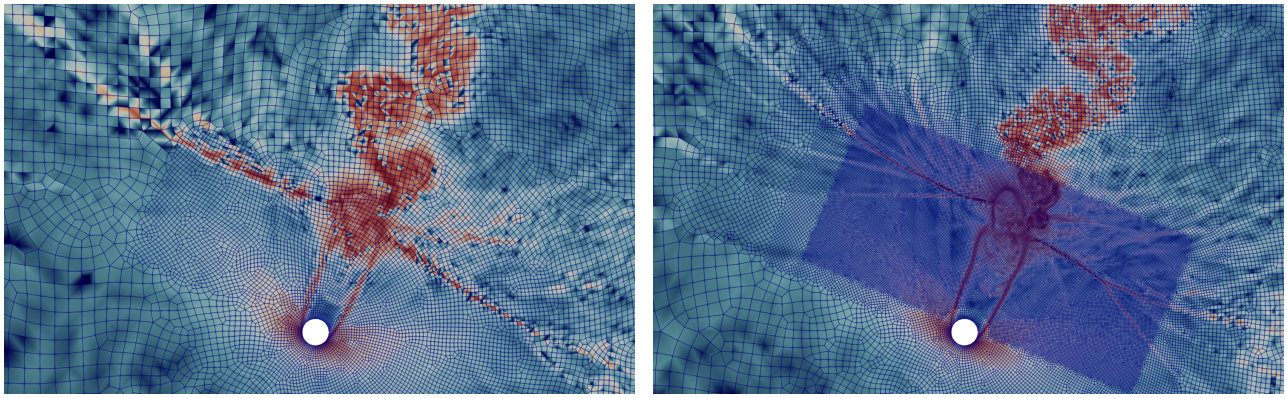

(a) Previous mesh (1st version, 1,104,570 elements). (b) New mesh (6th version, 2,354,040 elements).

Figure 5.17: First and sixth versions of meshes for the wake generator domain, zoomed in the shock region.

The second problematic aspect considered is the application of AV in the wake vortices. Indeed, AV is applied at the shock location, but also in the wake close to the shock as some strong vortices fulfill the AV sensor condition. Then, those vortices are carried downstream by the flow with the AV. This situation leads to the transportation of AV towards regions less refined, creating large variation of viscosity between adjacent elements, see Fig. 5.18. Moreover, Fig. 5.18 shows that the most important values of AV are located in the vortices of the wake and not in the shock anymore. For comparison, the value of the AV applied in the

wake vortices is 4e-4 [Pa.s] and the free stream dynamic viscosity is 1.5e-5 [Pa.s]. Meaning that the viscosity varies by a factor about 30 between 2 adjacent elements.

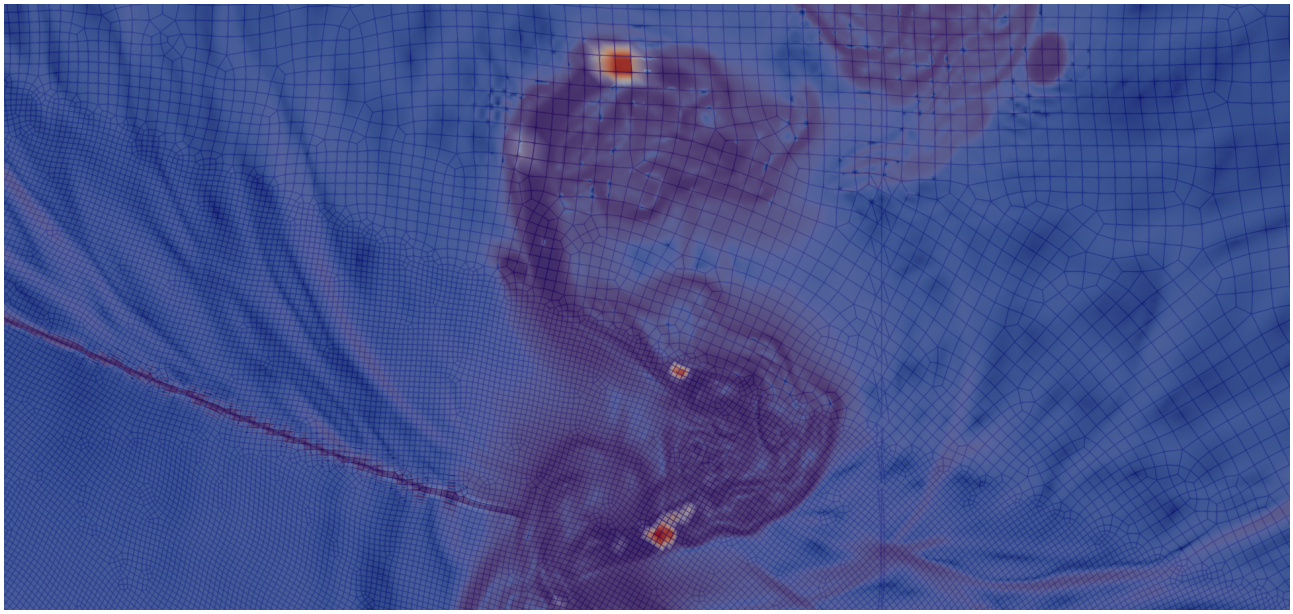

Figure 5.18: Schlieren with AV superposed, at t = 4.15e-4s, sixth mesh version.

To tackle this issue, the AV is only applied on a box, located in the shock region such as to remove the AV from the wake vortices. This AV box solved the problem for 282 additional time-steps but failed at iteration 22413. The use of AV box in the context of two coupled domains showed that domain specification in the AV definition does not work in ArgoDG, see Fig. 5.19, but it is not a problem in this case as there are not strong variations in the density field close to the LE of the blade.

Figure 5.19: AV box around the shock region. Highlight on the domain specification problem.

It appeared that the AV box worked by removing the AV from the wake vortices, but did not solved the problem inside the box. Increasing the size of the box along with an increased mesh refinement region at the start of the wake did not work either (seventh mesh see Fig. 5.23a). Nonetheless, it showed that in the wake vortices, important values of AV were applied in locations where the AV sensor did not detect strong density discontinuities, see Fig. 5.20.
Comparing Fig. 5.20a and Fig. 5.20b, one can see that the AV is wrongly imposed in a wake vortex as the AV sensor did not even detect a discontinuity there. This is due to the update of the AV. The problem was solved by changing the update frequency of the AV from *WithinNewton* to *EveryTimeStep* in the input file. So, instead of updating the AV at each GMRES iteration, the AV is only updated at each time-step which is apparently more stable in the present case, where AV is applied on rapidly moving discontinuities such as

the wake vortex visible in Fig. 5.20b.
With this change of AV update frequency, AV box, and 7th mesh version, the simulation ran without problems (up to t = 5.02e-4s).

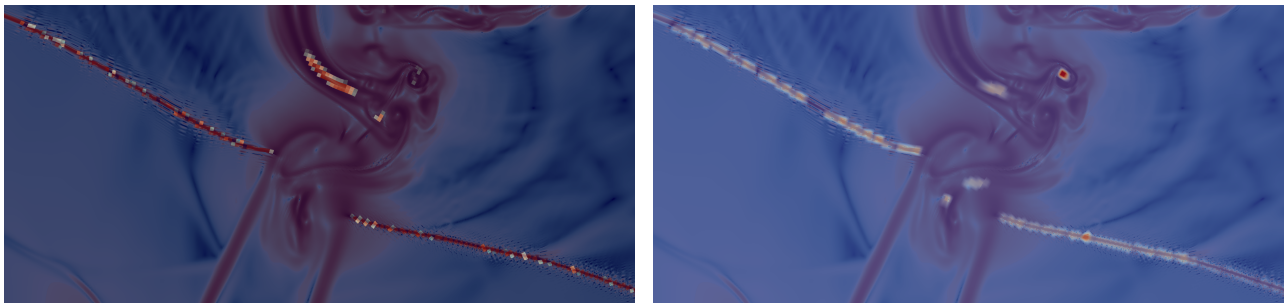

(a) Schlieren with superposed AV sensor.

(b) Schlieren with superposed AV.

Figure 5.20: Comparison of AV sensor (left) and actual applied AV values (right), one time-step before the solver's failure.

Before the change of AV update frequency, a simulation without AV was tested to verify that the solver's failure was related to the AV. This simulation ran with success, proving that the AV was indeed at the root of the problem but also that the simulation was able to run without AV to stabilize the shock. However, until now, AV was necessary due to the presence of the shock, see the transient solution of the wake generator alone in section 5.1. Indeed, the effect of the complete removal of the AV is directly visible in the shock vicinity, see Fig. 5.21, where oscillations around the shock start to grow. Nevertheless, the multiple mesh refinements in the shock region seem to be able to limit them. As it is preferable to have small spurious oscillations than AV, the simulation is continued without AV. Moreover, removing the AV reduces greatly the computation time (from 174 to 300 time-steps/hour) as no more artificial discontinuities are introduced in the solution.

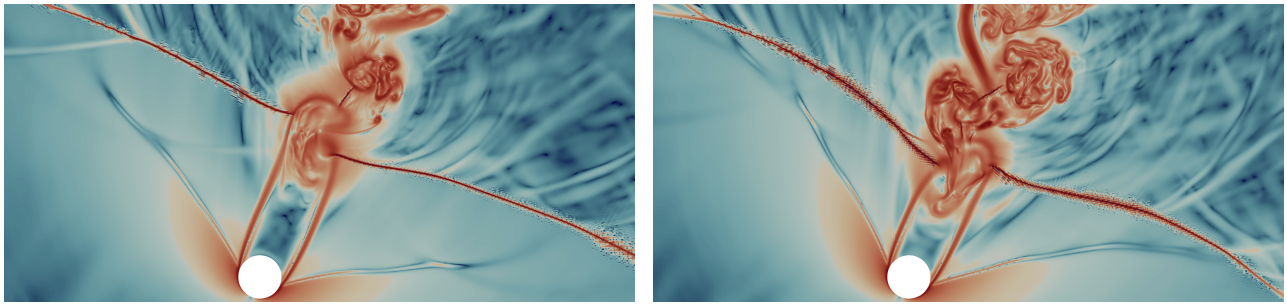

(a) Schlieren of the shock before AV removal.

(b) Schlieren of the shock after AV removal.

Figure 5.21: Comparison of the shock before AV removal, t = 5.02e-4s (left) and t = 5.38e-4s after AV removal (right).

The simulation ran without AV from t = 5.02e-4s until t = 1.1083e-3s during which the length of the "branches" of the shock is increasing and eventually goes out of the most refined region, leading to too strong oscillations which results in solver's failure, see Fig. 5.22.

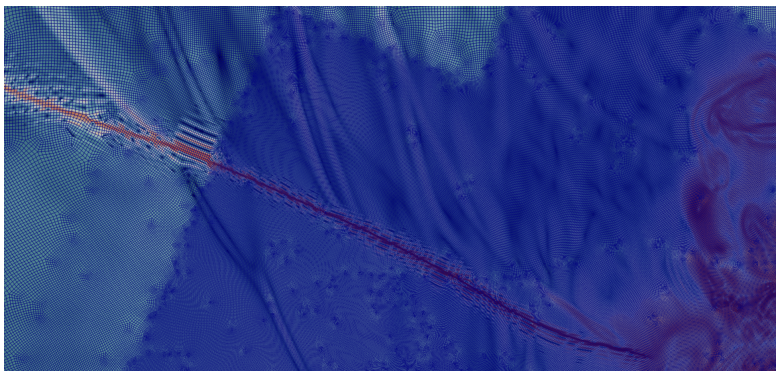

Figure 5.22: Schlieren with seventh mesh version, adaptation level 2, one time-step before solver's failure.

To resume the simulation, an eighth mesh version is made with the width of the most refined region increased, see Fig. 5.23 for the comparison between seventh and eighth meshes. About 200k elements are added to the seventh mesh to obtain the eighth mesh, which require 2 additional nodes for the calculation on Lucia. That makes 30 nodes in total, so 3840 CPUs working in parallel. That represents a tenth of Lucia's resources with a long queue time related to the use of such amount of resources.

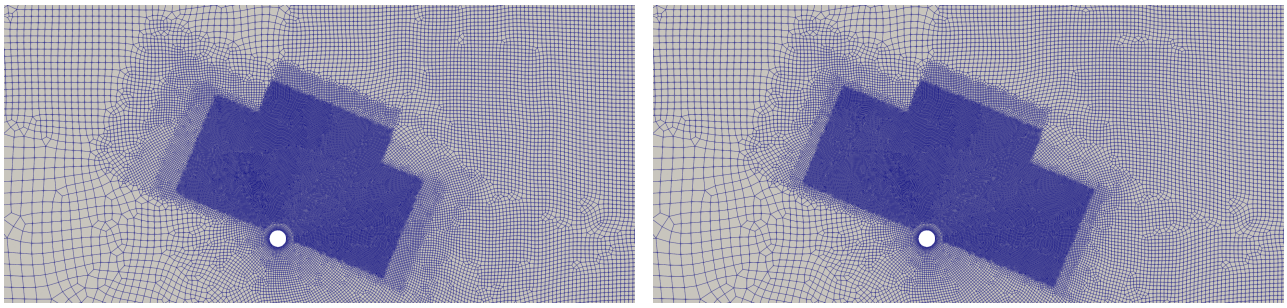

(a) Seventh mesh version, 2,415,060 elements.

(b) Eighth and last mesh version, 2,602,500 elements.

Figure 5.23: Comparison of the last two mesh versions, with the increase of the width of the most refined region to capture the shock.

Restarts from t = 1.105e-3s and t = 1.1e-3s with the eighth mesh did not work, even if they removed the spurious oscillations seen in Fig. 5.22. Also in 3D view, the origin of solver's failure was not found. However, restart from t = 9.4e-4s with the 8th mesh worked. Fig. 5.24 shows the 2 simulations with the 8th mesh at t = 1.105e-3s, one restarted from t = 1.1e-3s that failed at t = 1.1083e-3s and one restarted from t = 9.4e-4s that succeeded. It can be seen that both simulations are quiet different in regions where the mesh is almost identical (same element size). These differences are due to the highly chaotic nature of the flow, with the shock constantly interacting with the unsteady wake.

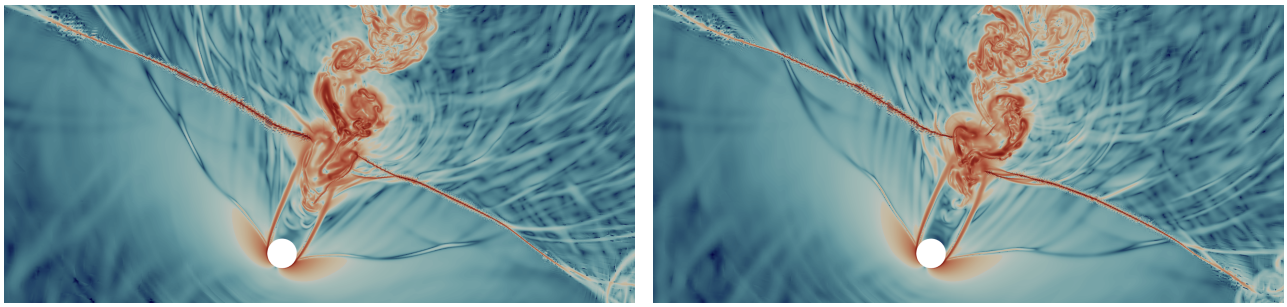

(a) Restarted from t = 1.1e-3s.

(b) Restarted from t = 9.4e-4s.

Figure 5.24: Comparison of 2 simulations with the eighth mesh at t = 1.105e-3s, one restarted from t = 1.1e-3s (left) that failed at t = 1.1083e-3s and one restarted from t = 9.4e-4s (right) that succeeded.

So, with the eighth mesh and the restart from t = 9.4e-4s, the simulation continued without other problems. The latest time reached by the simulation is 1.5e-3s from the coupling of the two domains.
In the future, the shock may change again and the mesh refinement region may need to be enlarged accordingly. Nevertheless, so far, the simulation is running with the eighth mesh version, a time-step of 1e-8s and a freeze Jacobian matrix of 10.
The difficulties encountered by the presence of large discontinuities in the solution induced by the presence of a shock and the intensive mesh refinement that was needed to take care of them proves that adaptive mesh refinement (AMR) methods are valuable when compressibility effects are important.

5.2.4 Outlet sponge layer

The environment behind the TE of the blade, such as the mesh refinement and the usage of sponge layer, have been conserved from Borbouse simulation to ensure comparable blade wakes. However, the definition of Borbouse's outlet sponge layer contains an inaccuracy which causes the sponge layer to be inactive. It results in spurious reflections at the outlet of the blade domain, flowing up to the TE, see Fig. 5.25.

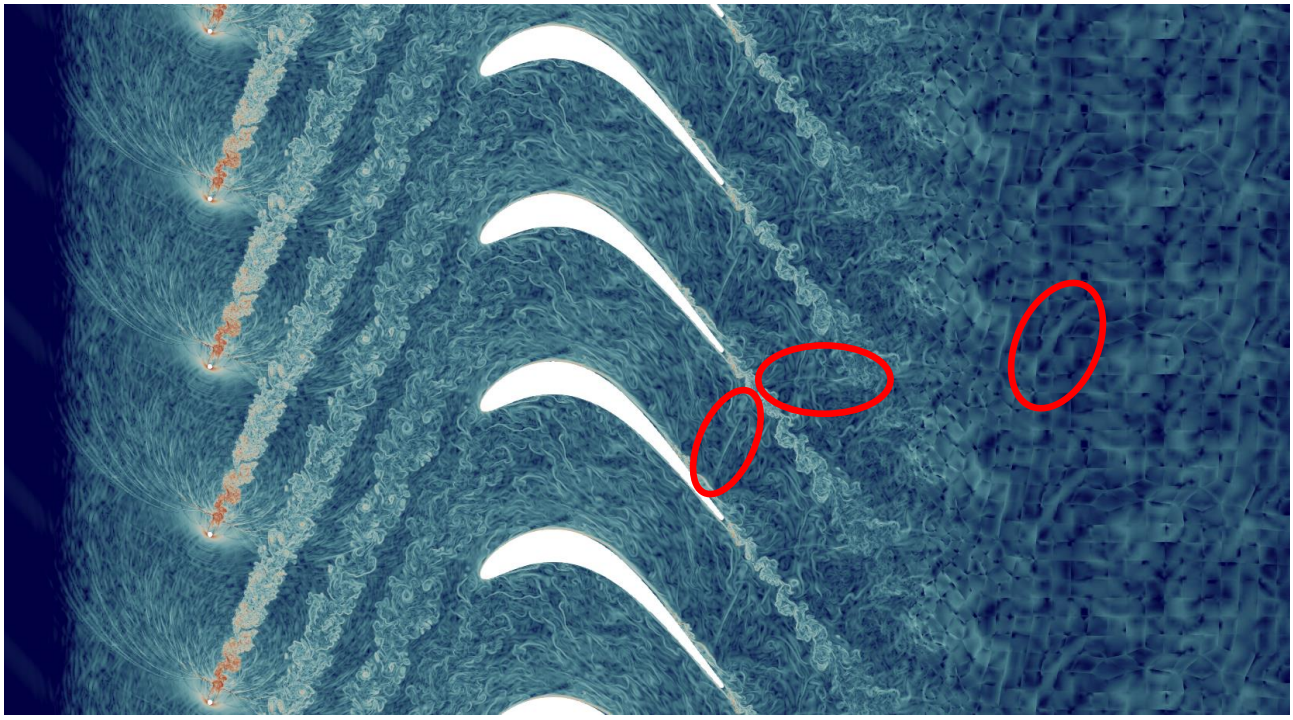

Figure 5.25: Schlieren on the complete computational domain without outlet sponge layer, t = 6.5014e-4s.

So, a sponge layer is added at the outlet of the blade domain, with the same parameters than the one at the inlet of the wake generator domain, see section 5.1.3, but inverted to damp the strong pressure waves going downstream. In that case, the expression of the penalty factor is

$$\sigma = 50000 \times (1 + \tanh(500 \times (x - 0.16354 + (g/2)))) \tag{5.5}$$

A visual observation of the direction of waves propagation confirmed that the outlet sponge layer indeed removed the waves going upstream. This confirmed that those waves were actually coming from spurious reflections on the outlet boundary and not from the wake of the blade as assumed initially.

5.3 Computation time decomposition

As introduced several times already, the computation time of such simulation is high with 4.4 days per convective time in the case of the two coupled domains. In general, after the transient solution, an unsteady turbulent solution is averaged in time during 10 convective times.
In this case with the incident wakes moving periodically with respect to the blade, time average must be applied for each fixed wake generator position which increases considerably the time of the averaging process. This is actually the precise reason why it has not been done in this work, for lack of time and tools to perform such expensive memory process.
Therefore, for such time expensive simulations, it is worth analysing the computation time to see which process is the most costly and if it can be optimized. For example, the tuning of the parameters of the Newton-GMRES algorithm such as the Jacobian recycling number (JRN) has a strong impact on the computation time. Indeed, Fig. 5.26 shows the time taken per time step for a last part of the simulation of the two coupled domains, from iteration 136000 to 137000. One can clearly see that each 250 time-steps, there is a peak in time consumption associated to that time-step. This is due to the restart saving file each 250 iterations. Then, the second line of time-steps that consume the most time is related to the Jacobian evaluation. Finally, the last small line close to the bottom are the times for the computation of the time-steps with Jacobian recycling. A zoom on the first 100 iterations is shown in Fig. 5.27 where the distinction is clear between the time-steps computed with and without Jacobian evaluation. The JRN is fixed to 10 here as the computation time for each time-step with Jacobian recycling is not increasing which indicates that the simulation is running smoothly.
Looking at those graphs, it is clear that the increase of JRN is highly advantageous to speed up the process. However, one should remain careful to still recompute the Jacobian regularly.
The usual value is a JRN of 5. The theoretical speed up with JRN from 5 to 10 is 11.6% and 6.55% from 10 to 20.
In this work, the lower update frequency was one Jacobian evaluation per 20 time-steps, until some increase in the number of required GMRES iterations per Newton iteration were noticed and the JRN decreased to 10 again. The speed up of 6.55% was considered to not worth the risk of introducing some problems afterwards. So, the speed up of 11.6% was considered sufficient while keeping the same number of GMRES iterations per Newton iteration.

An example of a simulation with a problem is shown in Fig. 5.28 and a zoom in Fig. 5.29. In that case, the problem was linked to the AV application as detailed in the previous section. In Fig. 5.28, it can be seen that the computation time is higher on average at all levels, with/without Jacobian evaluation and also for the restart saving file each 50 iterations. Also, for such simulation with complications, the computation time varied between time-steps which required a smaller JRN to ensure convergence and therefore an increased global computation time.

Increasing the time-step can also lead to great computational speed up. However, it is sometimes preferable to keep a smaller time-step.
When the simulation is running smoothly like the one in Fig. 5.26, increasing the time-step by 2 or 5 times is possible. However, a longer time-step increases the number of GMRES iterations and also Newton iterations as the new solution is further away than the last computed solution. This is also due to the fact that the matrix of the resulting system to solve is diagonally dominant the smaller the time-step. So, increasing the time-step two times does not lead to a computation time divided by 2.
Also, reducing the time-step allows to be closer to the exact solution.
In this work, the bigger time-step of 1e-7s was used for the p0 initialisation of the solution for the wake generator. After the transition to p3, reducing the time-step to 5e-8s and sometimes to 1e-8s was forced.

To conclude, this computation time decomposition can help to optimize the computation process, and also lead to early problem detection.
In the present work, this method has been used continuously with many changes of Jacobian recycling number and time-step to adapt to the whims of the solution.

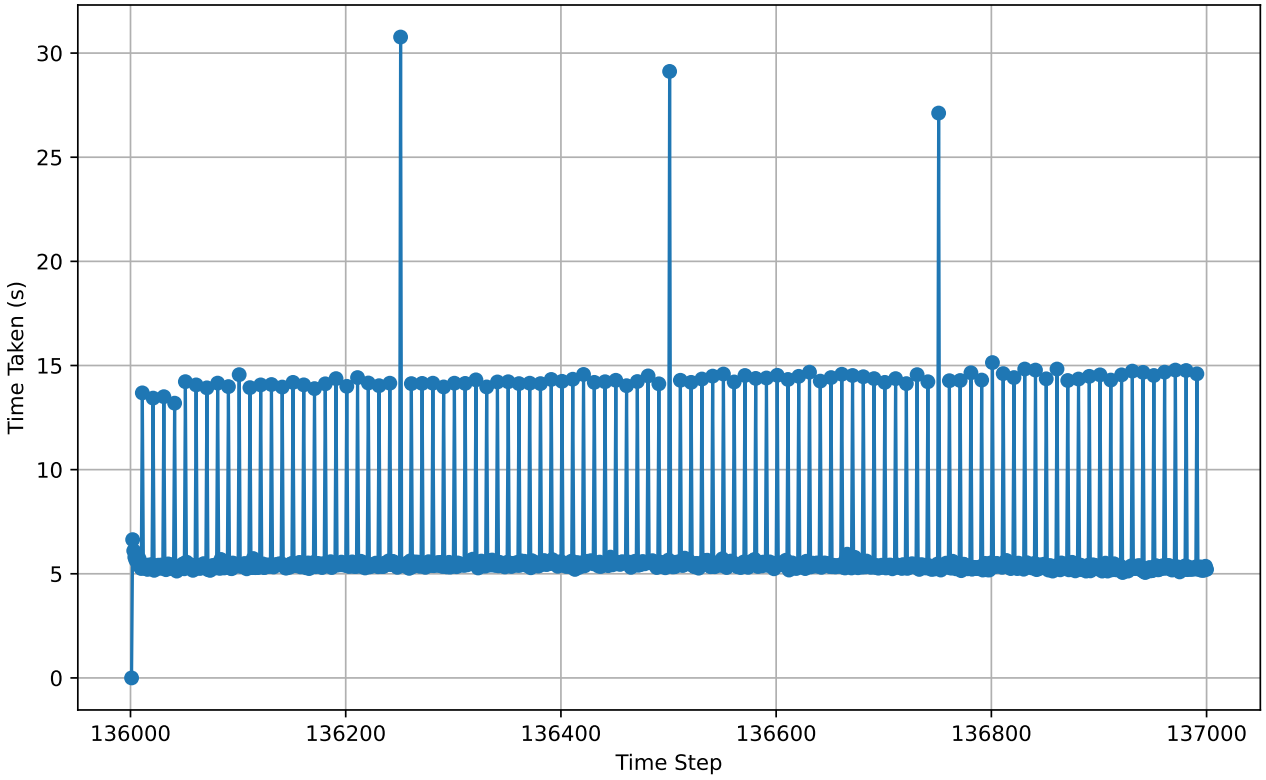

Figure 5.26: Computation time of each time-step of the simulation of the two domains coupled between iterations 136000 and 137000. Jacobian recycling number to 10.

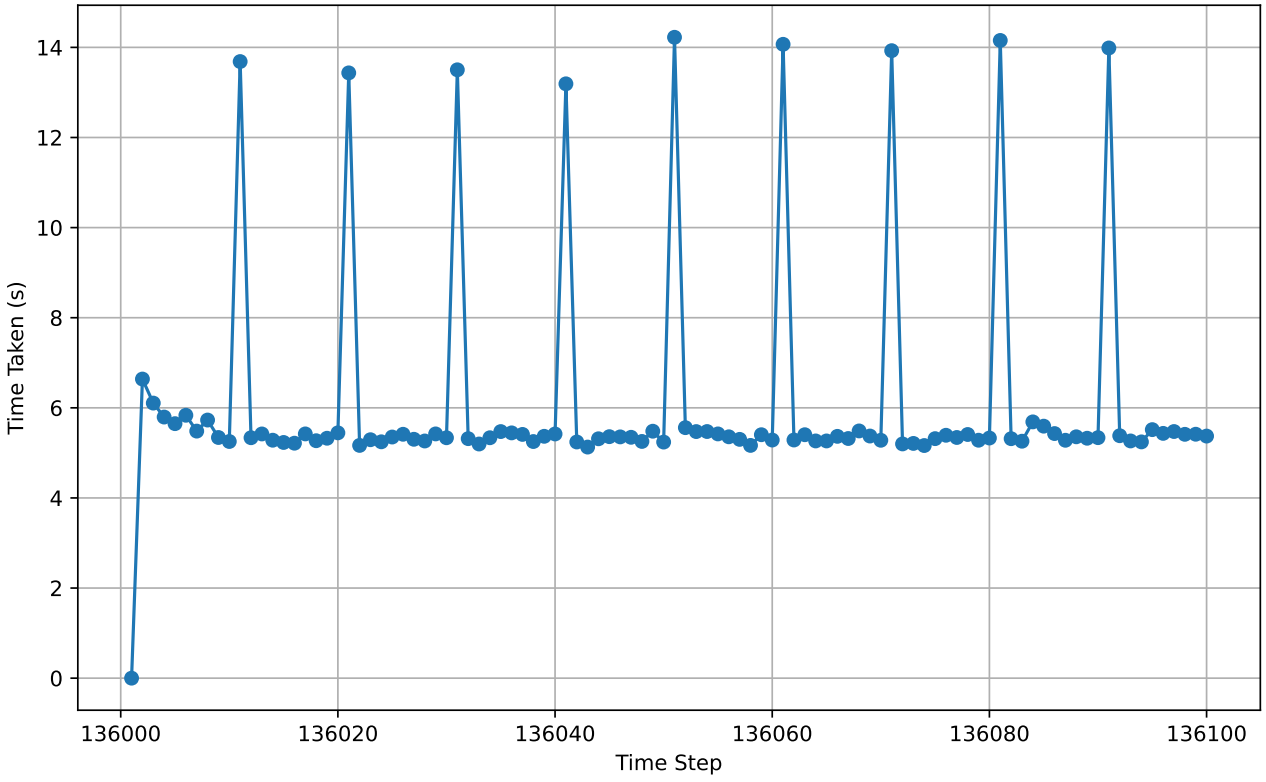

Figure 5.27: Computation time of each time-step of the simulation of the two coupled domains between iterations 136000 and 136100. Jacobian recycling number to 10.

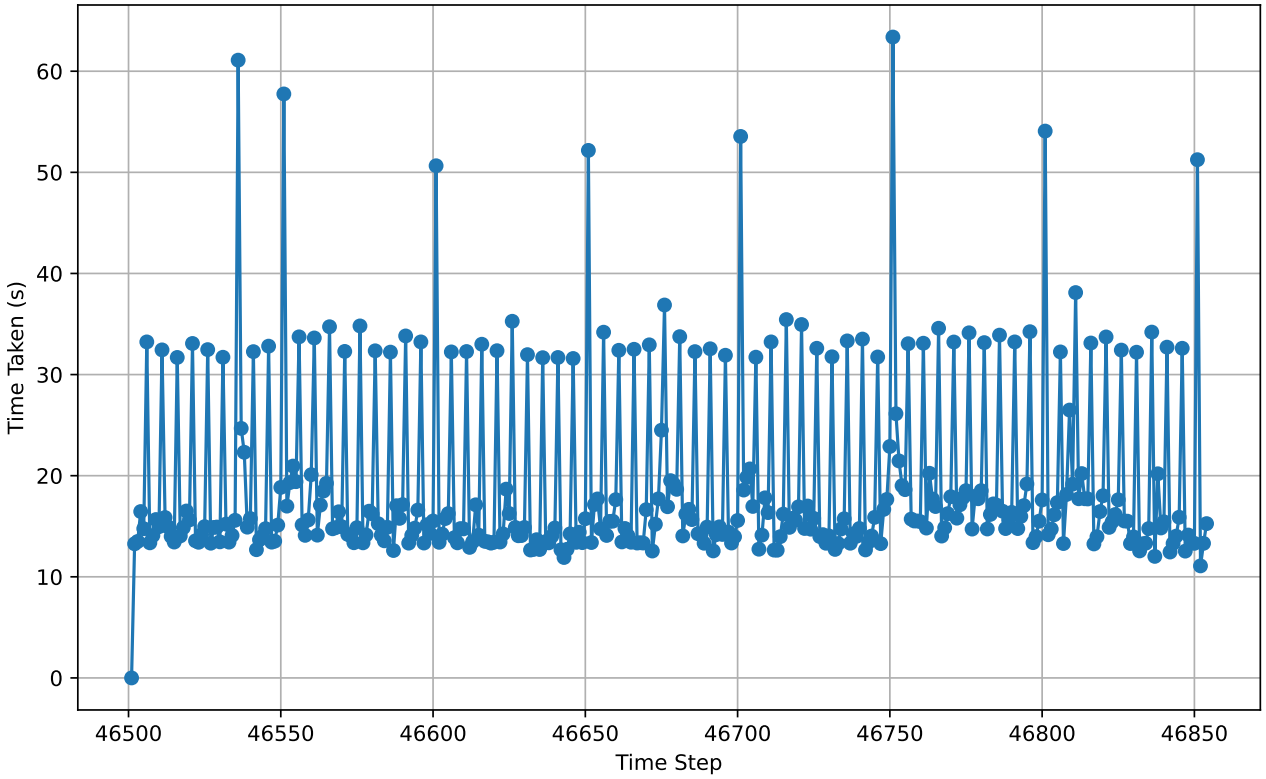

Figure 5.28: Computation time of each time-step of the simulation of the two coupled domains with the fifth mesh version and AV box, iteration 46500 until algorithm's failure. Jacobian recycling number to 5.

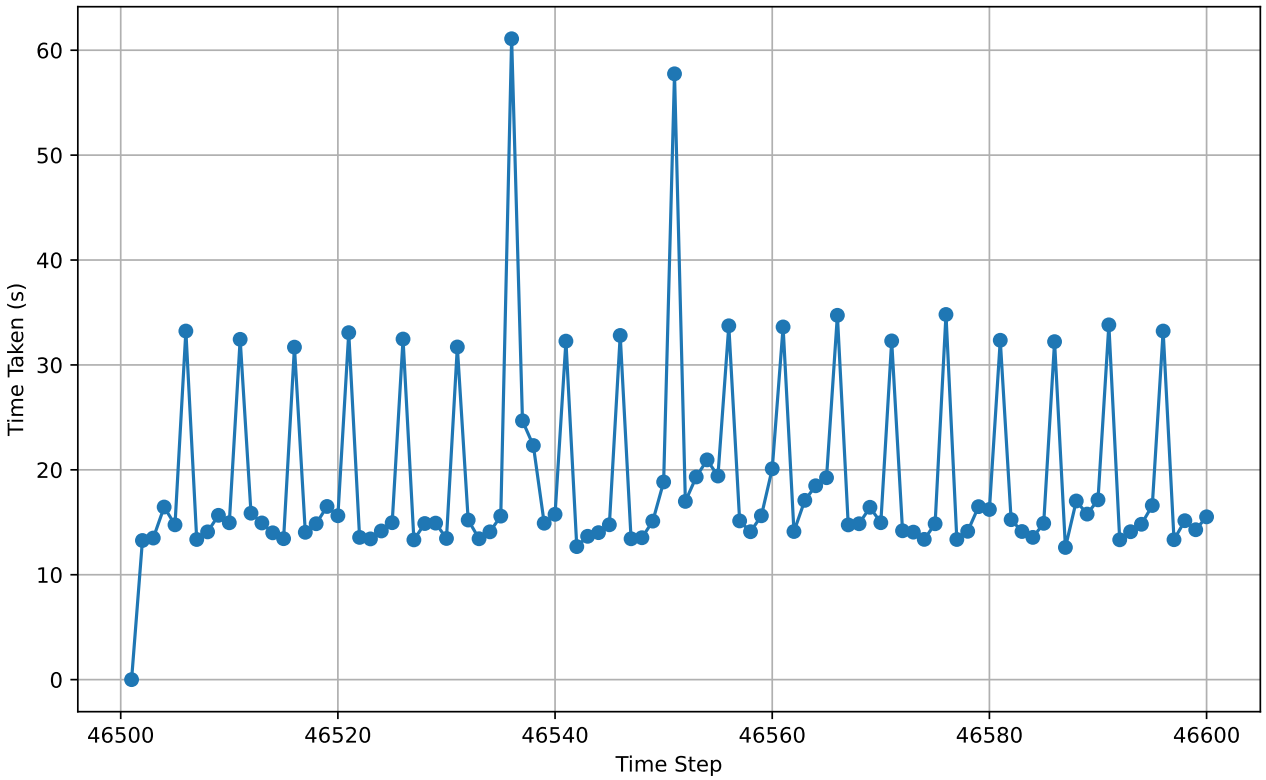

Figure 5.29: Computation time of each time-step of the simulation of the two coupled domains with the fifth mesh version and AV box, between iterations 46500 and 46600. Jacobian recycling number to 5.

6 Results

In this chapter, the results of the numerical simulations are presented. Those results are obtained from instantaneous and averaged flow variables, after the end of the transient phase described in the previous chapter.
First, the wake generator is analysed with a first part on the shock, a second part on the wake and a third part on the outlet flow angle.
In a second time, the coupled domains of the wake generator and the blade cascade are analysed, with a focus on the blade boundary layer followed by a more qualitative discussion on the rotor-stator interaction.

6.1 Wake generator

6.1.1 Shock analysis

As described in section 2.1.4, the flow regime around the cylinder of the wake generator is characterized by $Re_D \approx 2000$ and $M \approx 0.8$ and the flow shedding period is indeed about 1.64e-5s. The acceleration of the flow around the cylinder reaches $M = 2$ in certain locations, see Fig. 6.1. That regime is characterized by a shock interacting with the unsteady wake. On each side of the wake, because of the oscillating wake, the shock is alternating between lambda shock and normal shock: when the wake is turning to the right, a lambda shock forms on the right and a normal shock on the left, and vice-versa when the wake is turning to the left, see figures in Fig. 6.4.
This shock-wake interaction is the continuous source of acoustic waves propagating away in all directions. Some parts moving upstream are colliding with the branches of the shock where they are stopped until they reach the end of the branches, see Fig. 6.2 with the Schlieren showing the density variations.

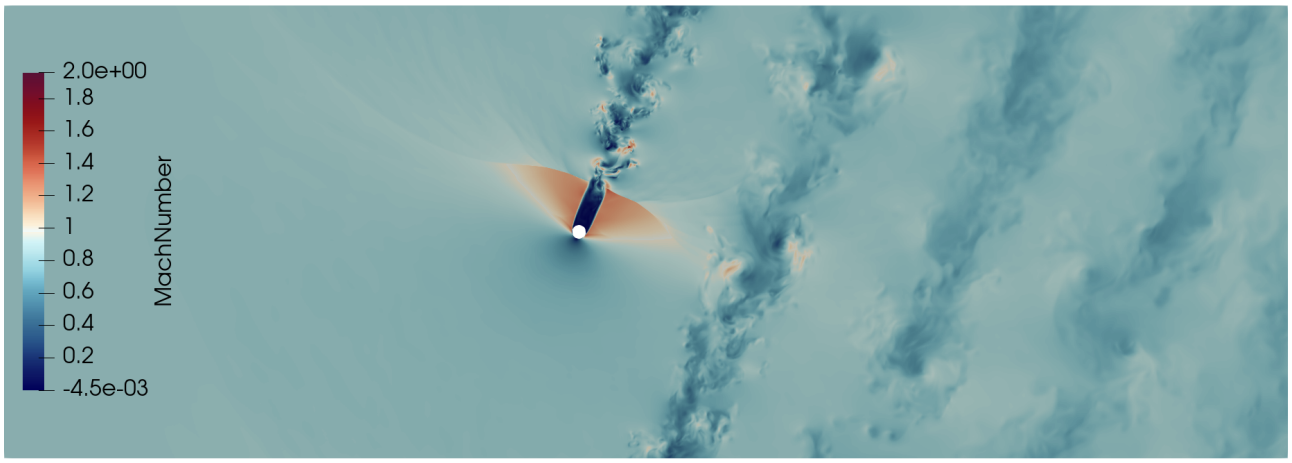

Figure 6.1: Relative Mach number of the wake generator.

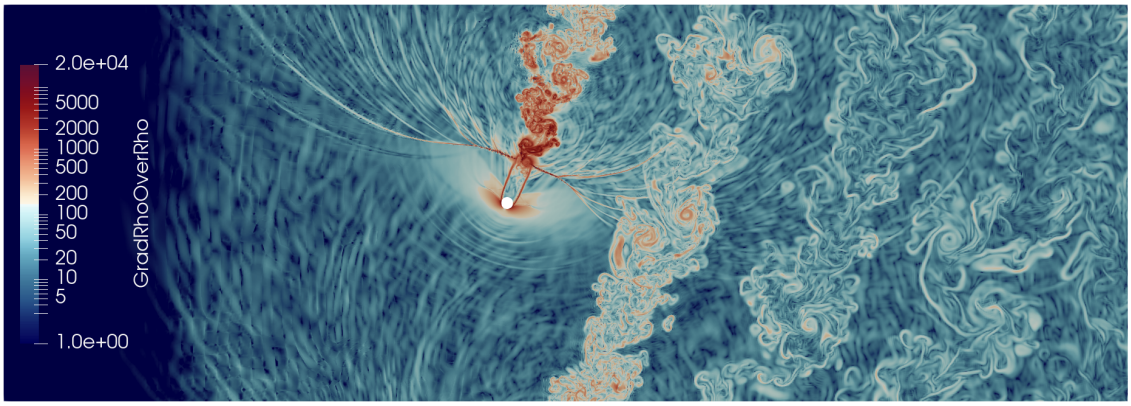

Figure 6.2: Schlieren of the wake generator.

In addition to the shock-wake interaction described above, the shock is oscillating between two positions: upstream (denoted as upper position) shown in Fig. 6.4a, Fig. 6.4e and Fig. 6.4i and downstream (denoted as lower position) shown in Fig. 6.4c and Fig. 6.4g. Those figures show the Mach number with the corresponding Schlieren on the right.
This shock motion identified during the transient phase of the wake generator forced the increase of the refinement region which led to a considerably higher number of mesh elements, see fourth mesh in section 5.1.1.

This oscillating upstream and downstream shock motion has not been found in the literature. An explanation to this could be that previous studies make use of turbulence models such as SST-DES in Bobenrieth Miserda and Leal [59], SST-RANS in Hoffmann and Weiss [32] or inviscid assumption such as in Kentzer [60]. In the present work, the high resolution of the shock region without AV thanks to the advantages of the DGM allows to capture the physics of the shock with a high fidelity. Also, an important aspect of this work is the translation of the cylinder with respect to the flow where in the literature in general, the cylinder is static. The cases where the cylinder is moving, in the literature, are related to the simulations of wake interaction in LPT. However, the rotating speed of the bars is much lower as introduced in section 3.3.1 such as in Li Xuejian et al. [11] where the speed of the bars is only 20 m/s.

From the available simulation time, some information can be retrieved about the periodicity of the shock oscillation. It appears that the upstream motion is faster than the downstream motion taking 1e-4s and 3.1e-4s respectively, as shown in Fig. 6.4.
A movie is made with all the saved time-steps that gives better insights on the situation: it seems that the shock stabilizes the wake which is slowly increasing its tail with reduced amplitude of oscillation, until a certain extend where the tail is too long leading to oscillations with larger amplitude until the shock is at its closest to the cylinder again.
At the upper position, the shock is stronger than in the lower position as shown in Fig. 6.3.
The distance of the shock from the cylinder is $4.5D$ at lower position and $2.5D$ at upper position with $D = 1$ mm, the cylinder diameter.

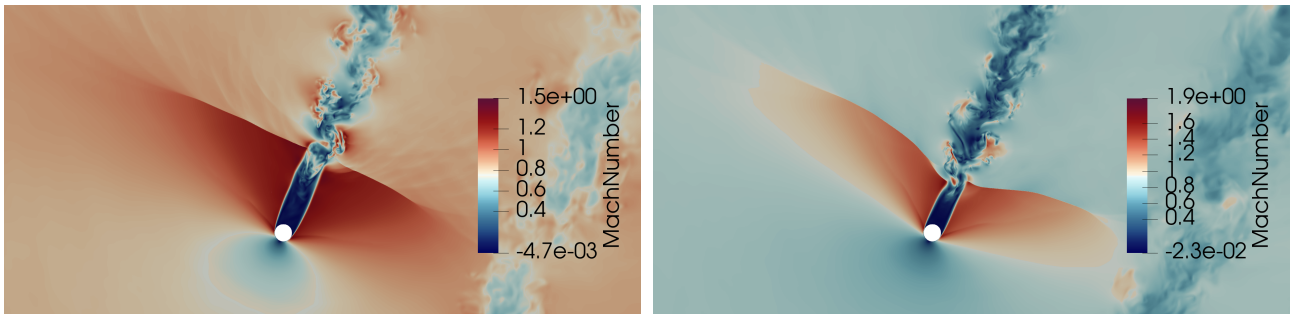

(a) Lower position, t=1.385e-3s.

(b) Upper position, t=1.485e-3s.

Figure 6.3: Mach number of the wake generator, zoom on the shock, at lower and upper positions.

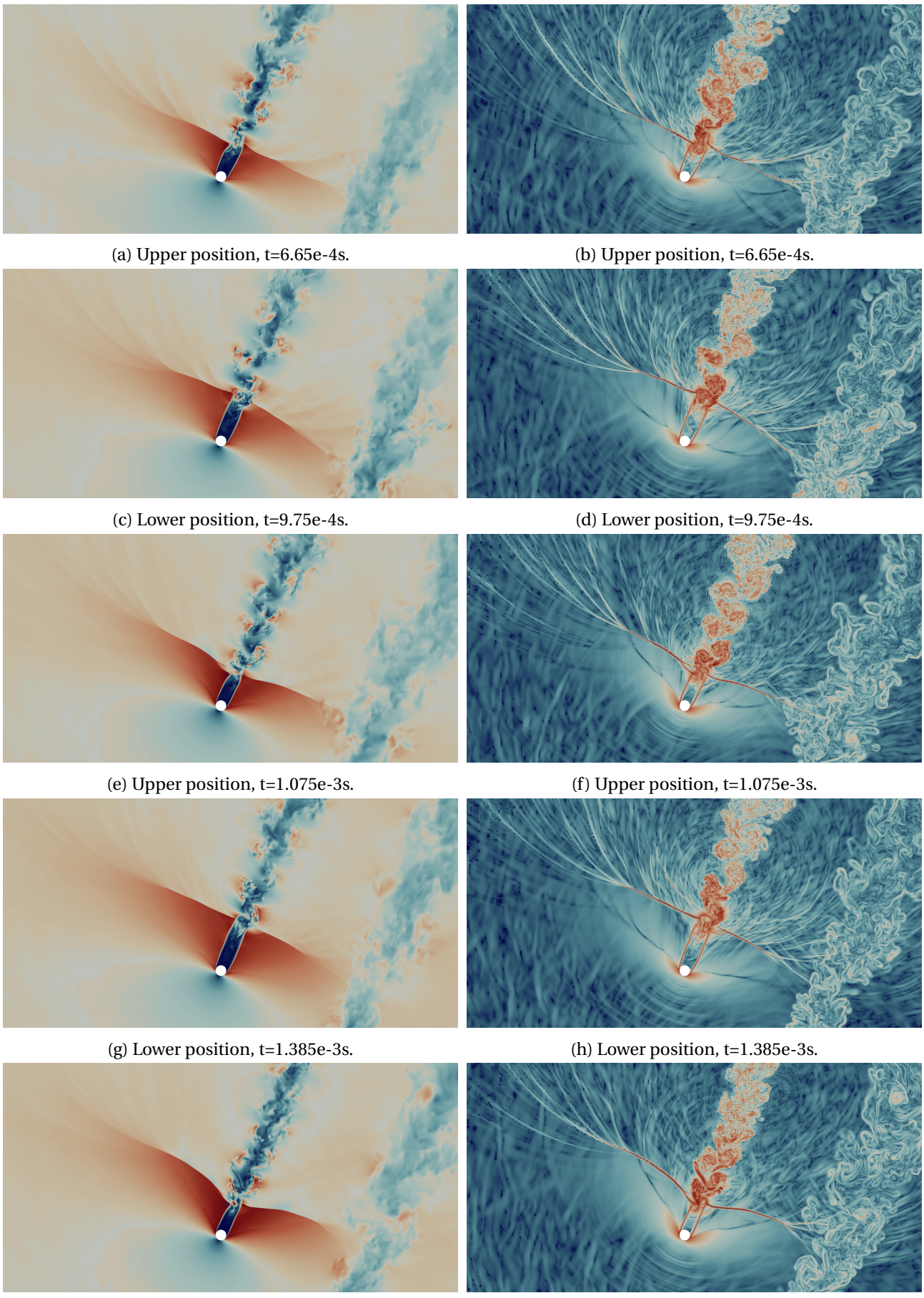

(a) Upper position, t=6.65e-4s.

(b) Upper position, t=6.65e-4s.

(c) Lower position, t=9.75e-4s.

(d) Lower position, t=9.75e-4s.

(e) Upper position, t=1.075e-3s.

(f) Upper position, t=1.075e-3s.

(g) Lower position, t=1.385e-3s.

(h) Lower position, t=1.385e-3s.

(i) Upper position, t=1.485e-3s.

(j) Upper position, t=1.485e-3s.

Figure 6.4: Mach number and Schlieren of the wake generator, zoom on the shock, at upper and lower positions.

6.1.2 Wake analysis

In this section, the wake generated by the rotating bar is analysed in details. This analysis is decomposed into six aspects of the wake. The first two aspects concern the influence of the AV on the wake and the validation of the span-wise width of the computational domain via the spatial correlations of the velocity. The last four aspects provide details on the total pressure defect, turbulent kinetic energy, turbulent intensity and Reynolds shear stress tensor.

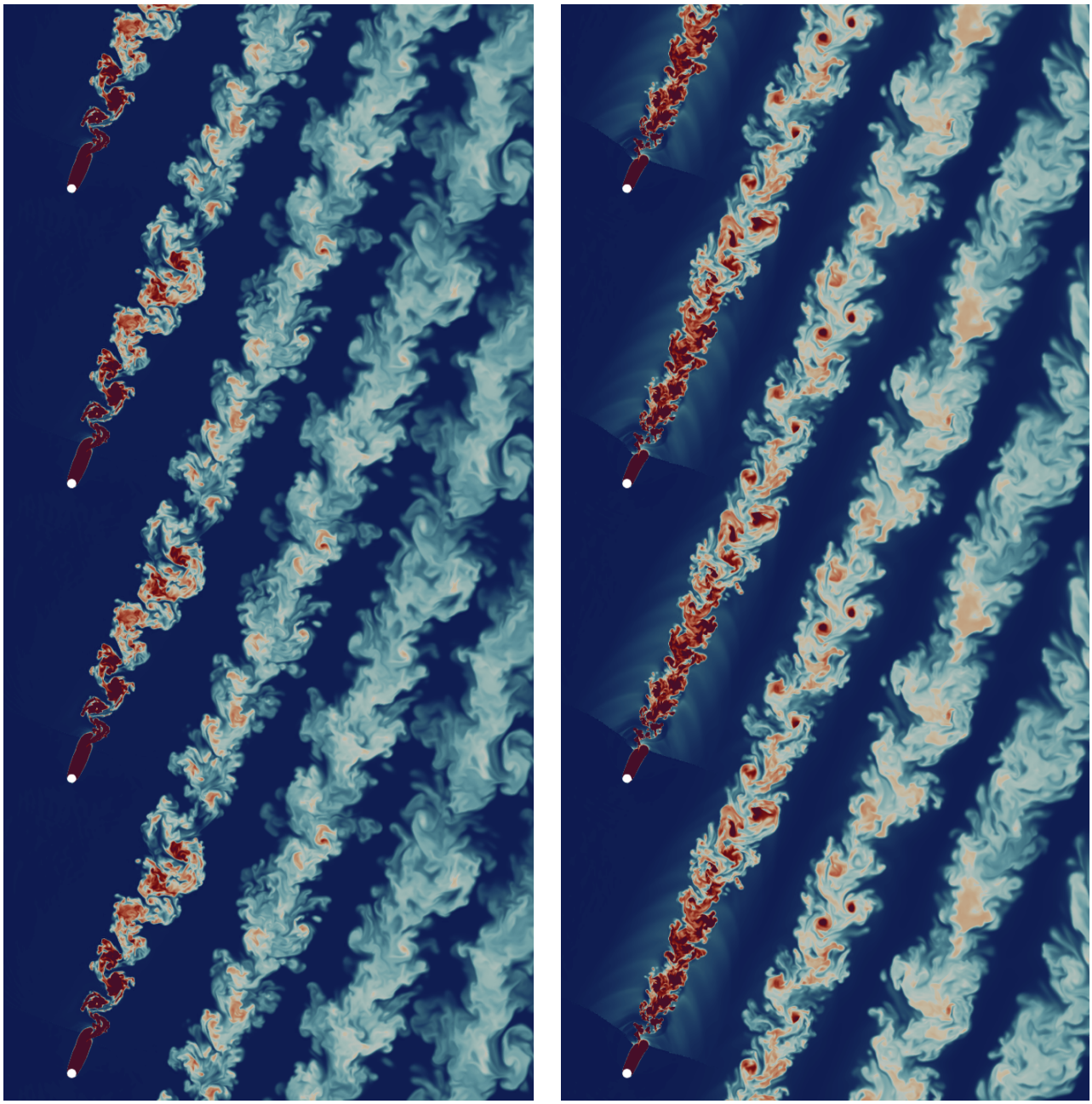

(a) With AV.

(b) Without AV.

Figure 6.5: Comparison of the entropy generated in the wake with and without artificial viscosity.

The data presented in this section are averages of the flow of the wake generator alone. This is possible as the probes are moving with the translating domain, following the vertical displacement of the wake. This is not the case if the probes are placed in the blade cascade domain where the periodic passage of the wake would force the use of a phase-averaging method. Here, no phase-average is needed which reduces the averaging period considerably. Moreover, the averaging process on the wake generator alone without the blade domain reduces the resource usage on Lucia from 30 nodes to 20. The convective time of the wake

generator alone is 1e-3s, see Eq. (4.4). To obtain averages of the flow during the conventional 10 convective times would require running the simulation for 100 days. Here, the averaging period is 20000 iterations of time-step = 1e-8s. This period have been obtained after 2 days of computations on Lucia. 20000 times 1e-8s corresponds to one period of the passing bar (pitch/$v_b \approx$ 2e-4s). Given this short calculation period, the data are presented for qualitative purposes and only used to estimate wake properties.

Influence of the AV

The comparison of the wake with and without AV can be done as the mesh elements size (5e-5m) in the most refined region are the same for the fifth to eighth versions of the mesh. The mesh changes from fifth version to eighth version concern small improvement such as the increase of the refined region at the extremity of the shock branches and in the start of the wake, see Fig. 5.23. The comparison is made between the wake with AV and without AV shown in Fig. 6.5a and Fig. 6.5b respectively. The first observation concerns the width of the wake that is thinner in the case without AV. The second observation is about the entropy generation from the shock which was not present at that intensity when AV was applied to the shock. The same entropy scaling is applied for both figures.

Correlations analysis

In the present and next subsections, the graphs are obtained from the local data captured by probes placed in the computational domain. Those probes are organized in a 3D grid. 8000 probes are used with 20 along the wake to capture its evolution with increasing distance from the cylinder, 20 perpendicular to the wake to capture the data along the width of the wake and 20 in the span-wise direction. The probes in the span-wise direction are used to make span-wise averages and also evaluate the spatial correlations of the velocity field in that direction to ensure that the thickness of the computational domain is adapted to the considered flow. This 3D grid of probes is defined using the option *GridAlongSpecifiedAxis* in ArgoDG. This grid definition takes into account the periodicity of the domain, making it easier to position the probes.
The following graphs in Fig. 6.6 show the velocity integral length scale and spatial correlations along the span-wise direction which is the unique homogeneous direction of the flow. At the span extremities, the spatial correlations are maximal as the flow is identical on both sides because of the imposed periodic boundaries.

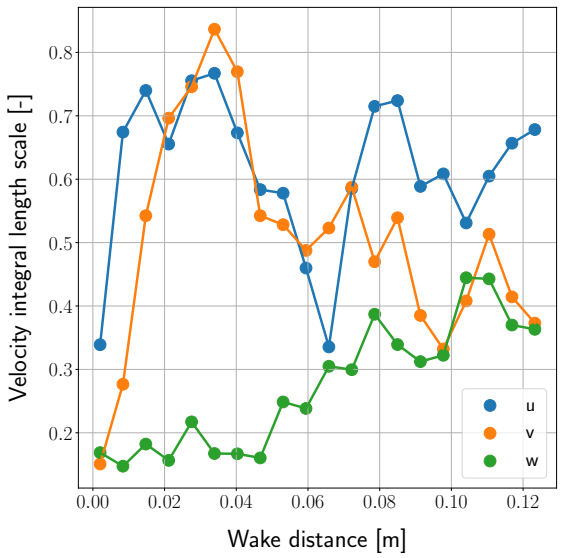

(a) Velocity integral length scale in the span-wise direction.

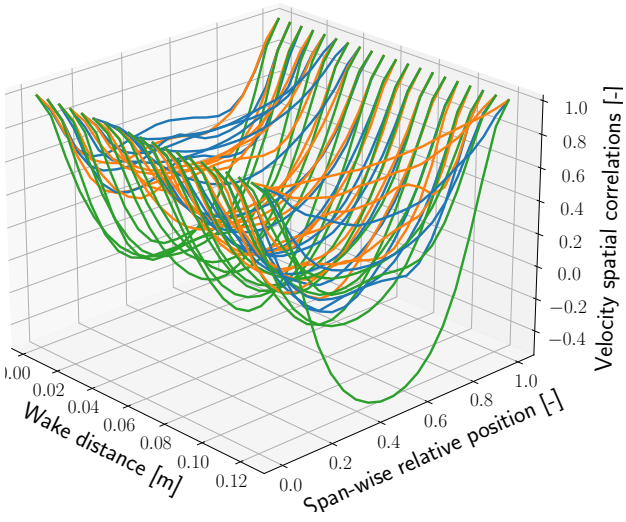

(b) Velocity spatial correlations.

Figure 6.6: Integral length scale and spatial correlations for each velocity component at wake center.

In the span center, the correlations are in general minimal leading to the definition of the integral length scale. The integral length scale is the distance over which the flow structures are correlated. In practice,

this distance should be smaller than the size of the span of the computational domain. The maximum value shown in Fig. 6.6a is 0.84 which means that the maximal correlation distance is 84% of half of the span. That means that the size of the span of 7% of the true chord is just large enough for the flow structures present in the simulation.

Total pressure defect

The total pressure defect caused by the passage of the rotating bar is shown in Fig. 6.7. The defect is maximal at the wake center and decreases with increasing distance from the bar located at (0,0,0).

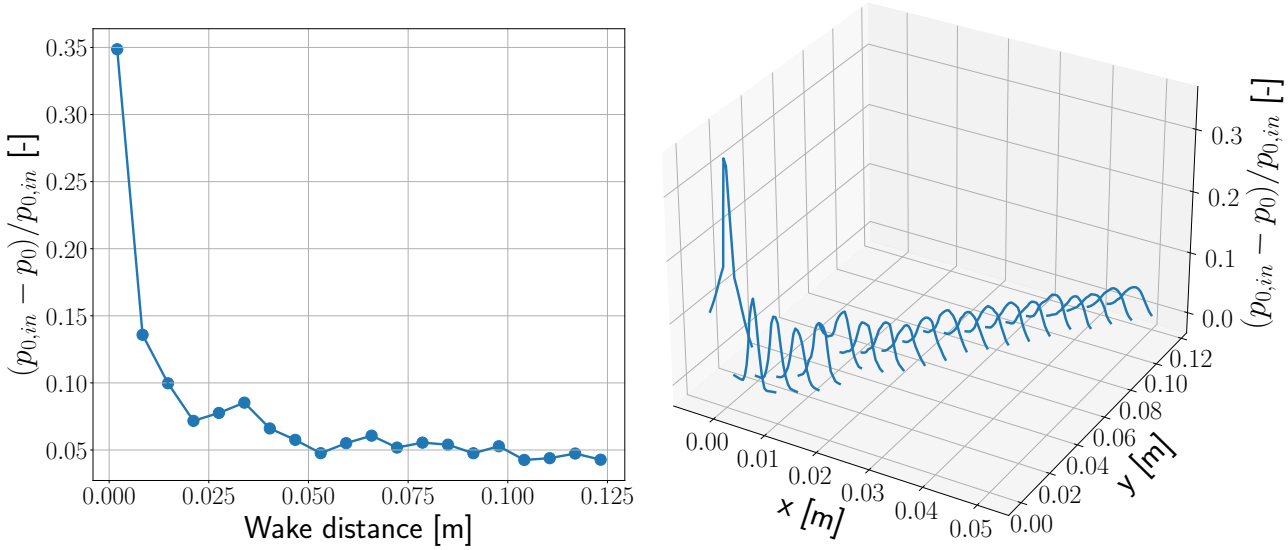

(a) Total pressure defect at the center of the wake.

(b) 3D view of the wake total pressure defect.

Figure 6.7: Total pressure defect in the wake. p_0 is the local absolute total pressure and $p_{0,\text{in}}$ the inlet total pressure.

Turbulent kinetic energy

The turbulent kinetic energy (TKE) in the wake generated by the translating bar is shown in Fig. 6.8. It is rapidly decaying with increasing distance from the bar. In this case, $U_{\text{is,out}}$ = 143.3 m/s is the outlet isentropic velocity for the wake generator, as defined in Eq. (2.5).

Turbulent intensity

The turbulent intensity (Tu) present in the wake and defined in Eq. (2.10) is shown in Fig. 6.9. The characteristic velocity U_∞ is chosen as $U_{\text{is,out}}$ because the interest is on the Tu that is entering the blade cascade domain and will interact with the blade boundary layer. At the outlet of the wake generator, Tu = 6.2% in the center of the wake. For comparison, the turbulence intensity generated by the turbulence grid placed in front of the wake generator in the wind tunnel to reproduce the turbulence present in real LPT conditions is 2.5%. The main difference being that the turbulence generated by the turbulence grid is uniform whereas the turbulence from the wake generator is localized in the wake, see Fig. 6.9b.

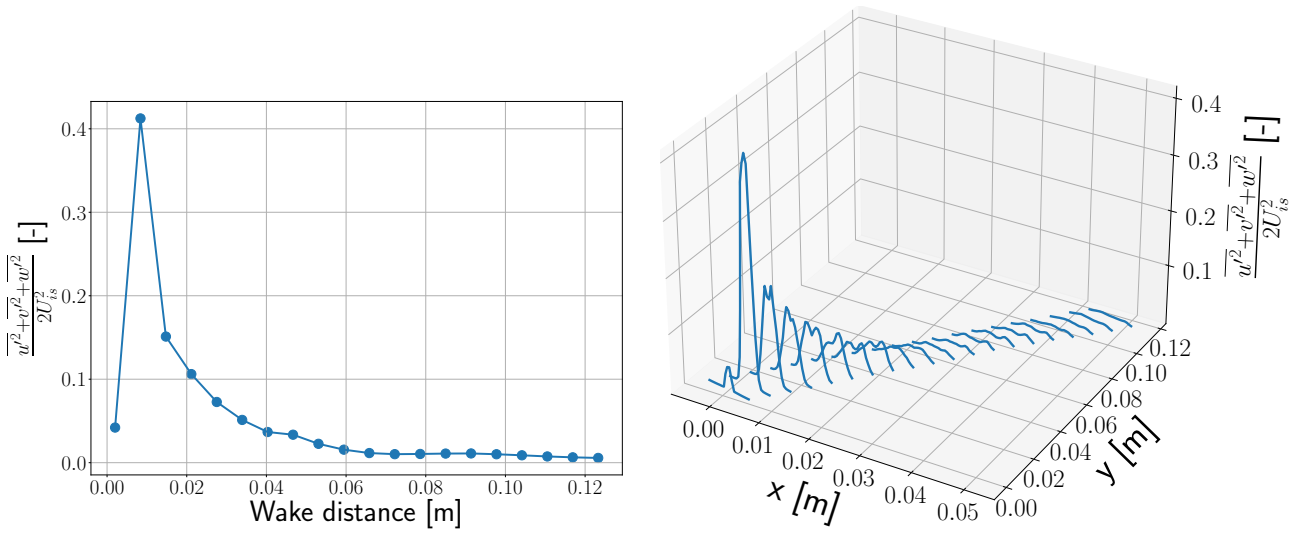

(a) Schlieren and AV superposed.

(b) Schlieren.

Figure 6.8: Simulation of the two domains coupled, zoomed at the start of the wake of the translating bar (t=3.6795e-4s). Schlieren on the left and Schlieren and AV superposed on the right.

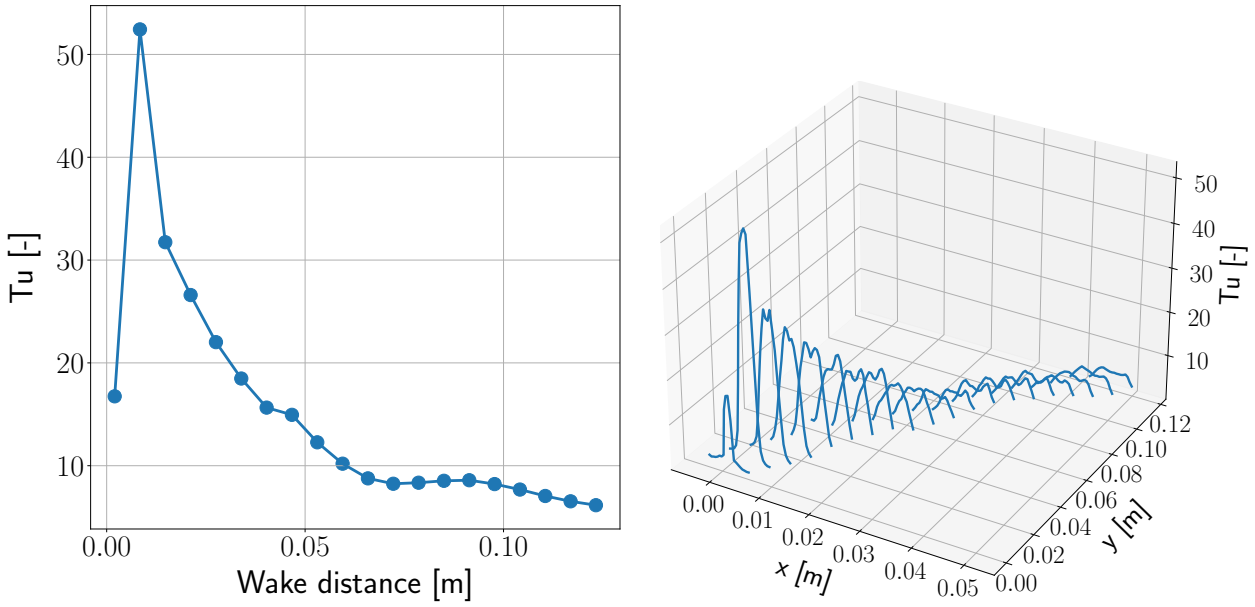

(a) Turbulent intensity at the wake center.

(b) 3D view of the wake turbulent intensity.

Figure 6.9: Turbulent intensity in the wake generated by the translating cylinder.

Reynolds shear stress

The following graphs in Fig. 6.10 show diagonal and off-diagonal components of the Reynolds shear stress tensor. Those velocity fluctuations components express the correlation between them, from low values if not correlated to high values, if highly correlated. The blue and orange curves show that the highest values are contained in the XY plane which can be explained by the development of von Karman vortex street in that plane. It can also be noticed that the decay of the turbulence is closely related to the spreading of the wake.

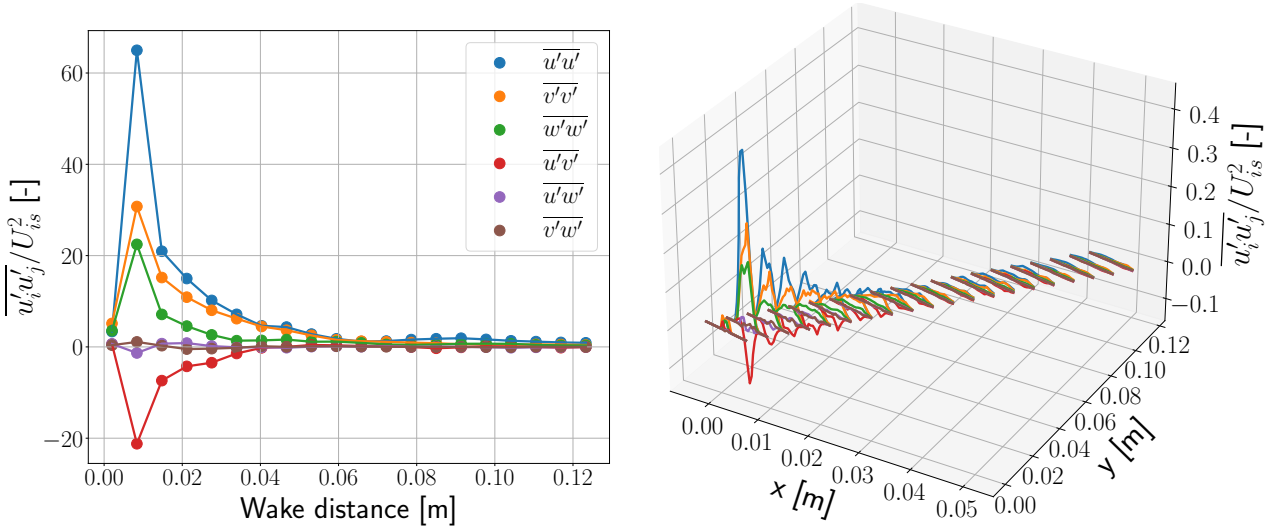

(a) Components of the Reynolds shear stress tensor along the wake.

(b) 3D view of the Reynolds shear stress tensor components in the wake.

Figure 6.10: Reynolds shear stress tensor components in the wake generated by the translating cylinder.

6.1.3 Outlet flow angle

The presence of the wake generator in the wind tunnel changes the direction of the global flow field. It is taken into account in the experimental campaign with the incidence angle adjustment, see section 3.3.1. From this numerical simulation, the flow angle at the outlet of the wake generator can be obtained. It is retrieved from probes located along the pitch at 1e-6m from the outlet. The span-averaged flow angle along the pitch is shown in Fig. 6.11.
The average value of the outlet flow angle along the pitch is 37.2° whereas it is 35.3° in the experimental campaign. Table 6.1 summarises the different values of the angle of the flow with the wake generator.
It is worth to emphasise that the outlet wake angle is obtained from the wake generator domain without the blade cascade downstream. The flow of the two coupled domains is slightly different from the one of the wake generator alone which can lead to differences in the actual numerical incidence angle. Phase-averages at the inlet of the blade cascade would give more exact information about the actual incidence angle.

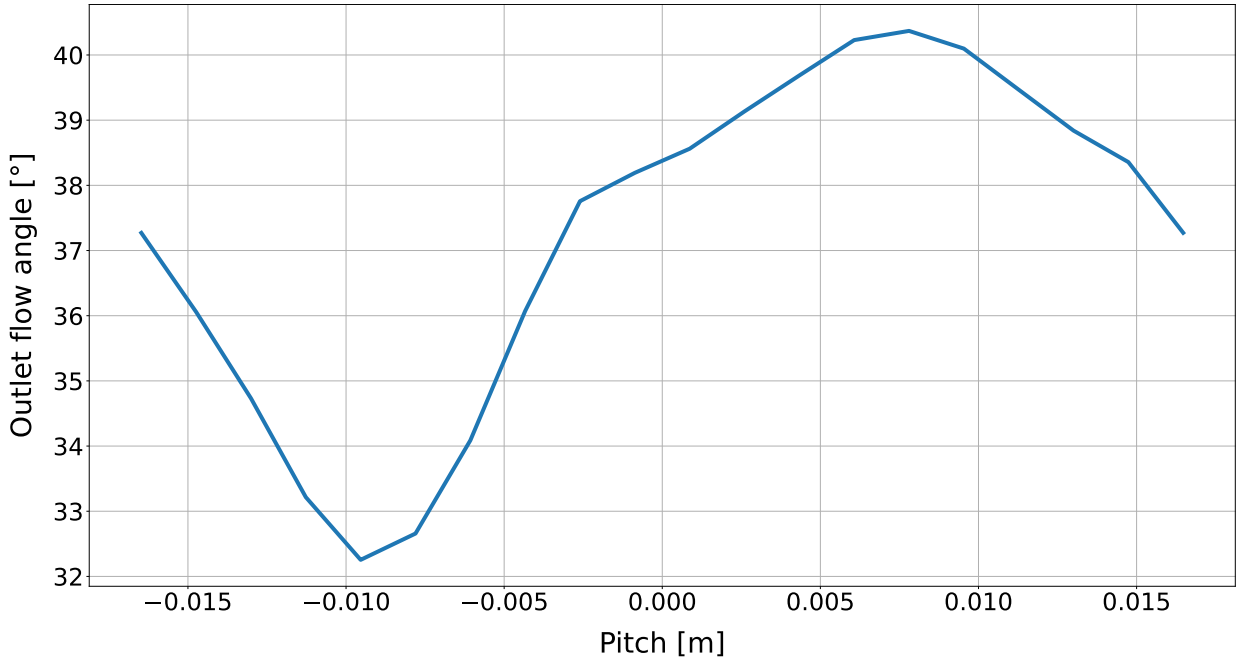

Figure 6.11: Flow angle along the pith of the wake generator outlet.

	Experimental	Numerical
Inlet flow angle	42.47°	42.47°
Outlet flow angle	35.3°	37.2°
Incidence angle	-2°	-0.1°

Table 6.1: Flow angles comparison between the experimental and numerical results.

6.2 Blade cascade with wake generator

The complete flow field of the two coupled domains is shown with the absolute Mach number in Fig. 6.12 and the Schlieren in Fig. 6.13.

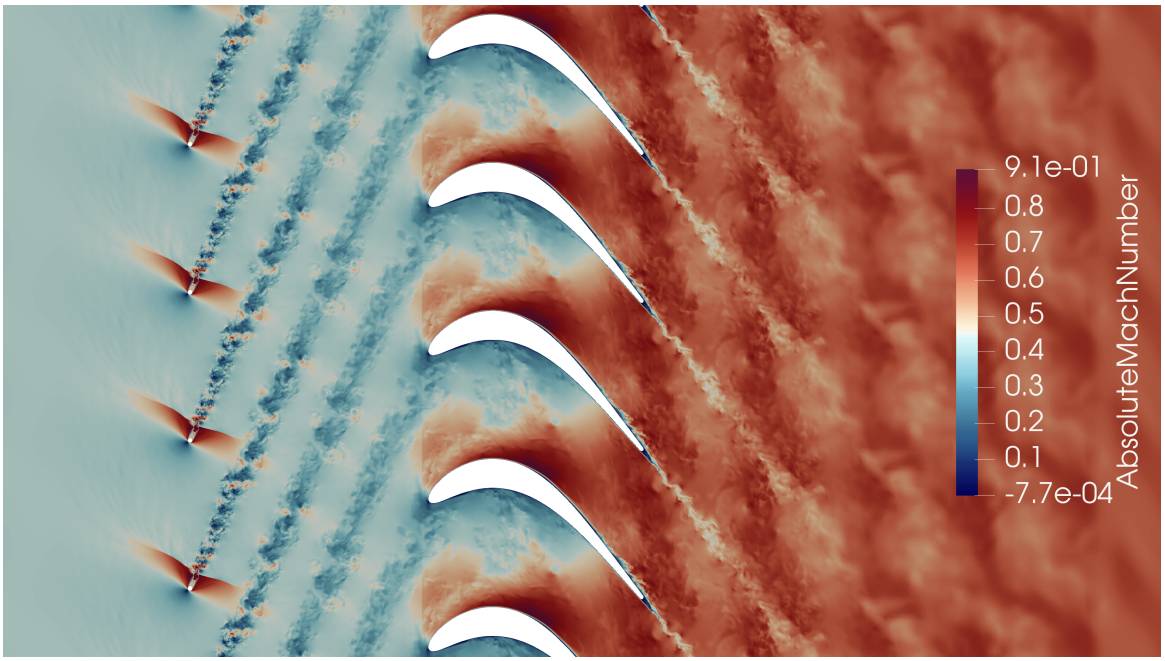

Figure 6.12: Absolute Mach number on the two coupled domains.

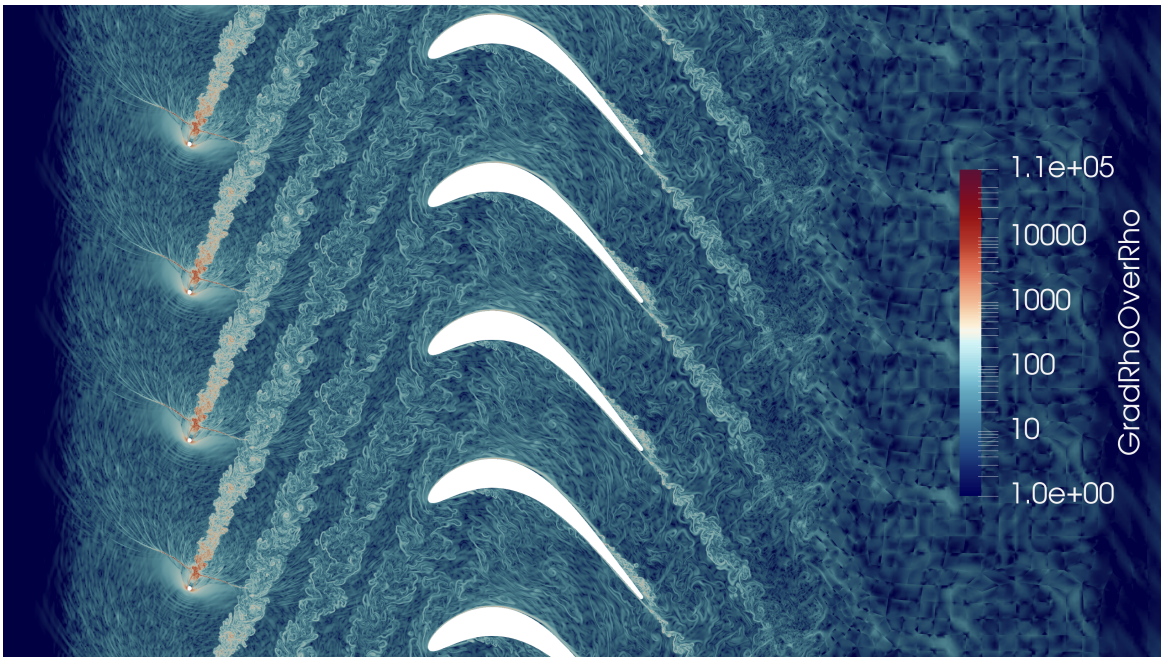

Figure 6.13: Schlieren on the two coupled domains.

6.2.1 Blade boundary layer

The passage of the wake is highlighted with the comparison between the simulations with and without wake generator, see Fig. 6.14 for the Schlieren and Fig. 6.15 for the entropy.
The first observation concerns the multiple acoustic waves travelling upstream in the case without wake generator in Fig. 6.14a. Those waves are spurious reflected waves on the outlet boundary and should not be present as explained in section 5.2.4. In the case with wake generator, the spurious reflections have not yet been completely eliminated.

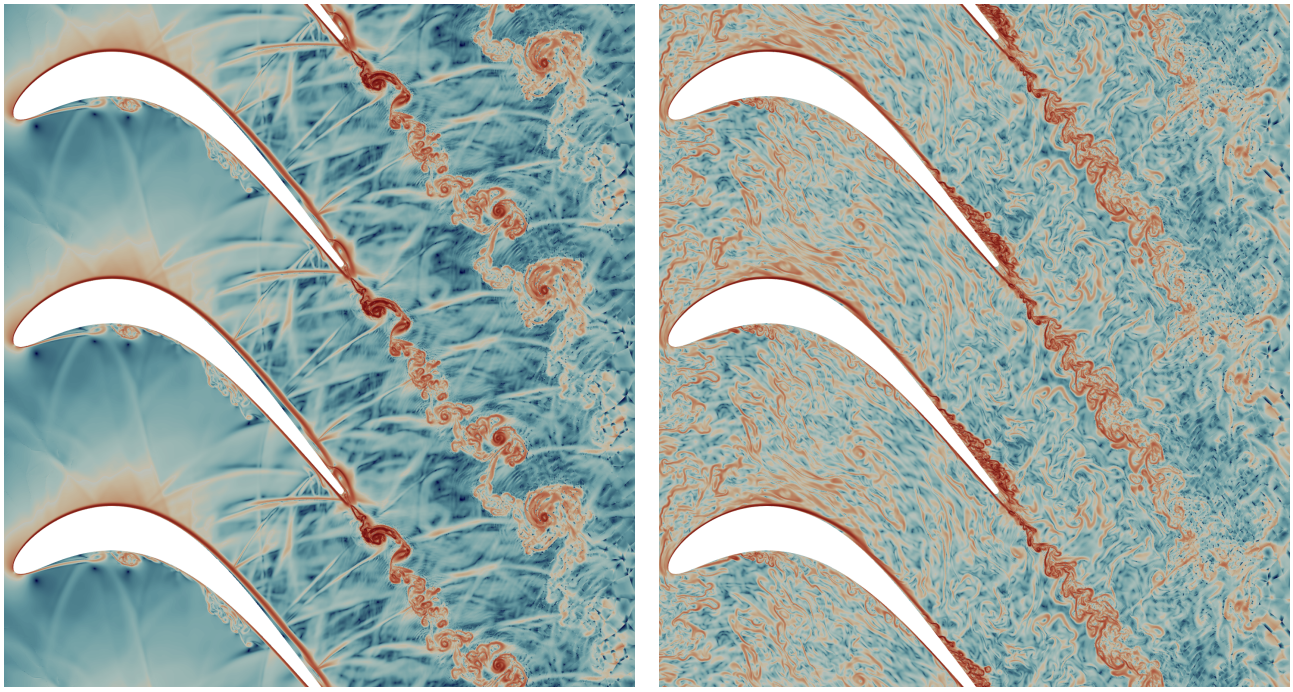

(a) Without wake generator.

(b) With wake generator.

Figure 6.14: Comparison of the blade wake with and without wake generator (Schlieren).

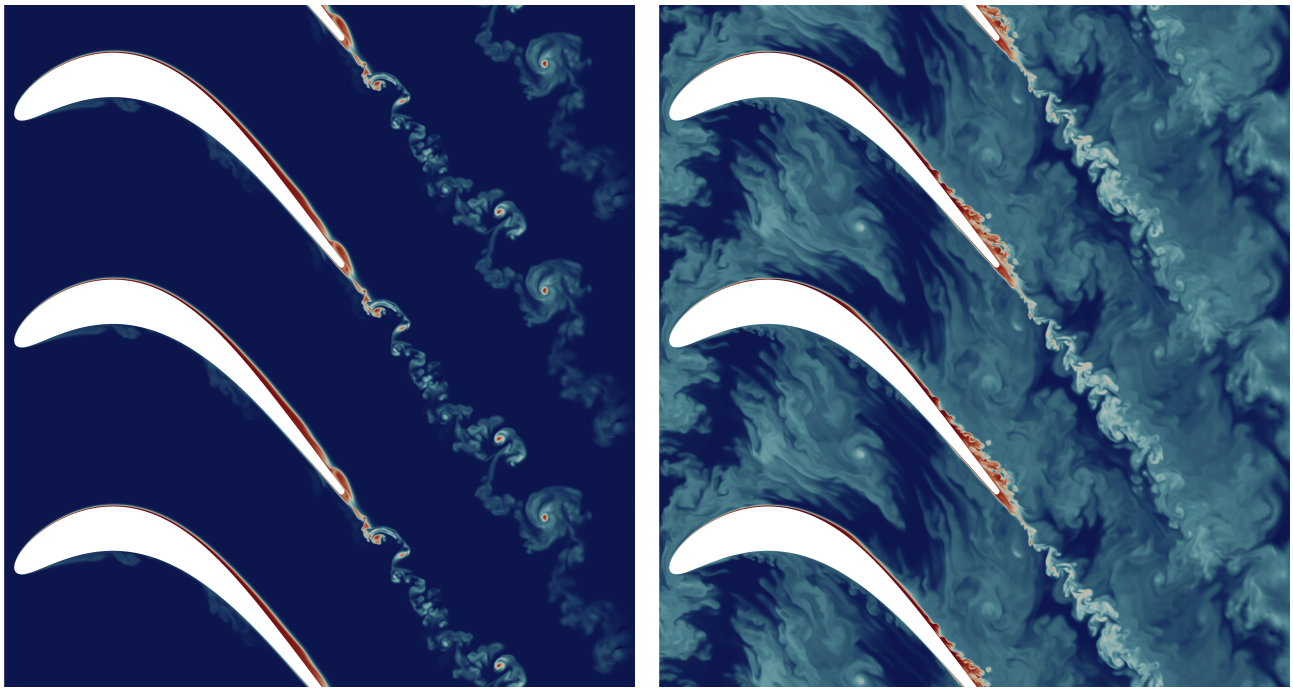

(a) Without wake generator.

(b) With wake generator.

Figure 6.15: Comparison of the blade wake with and without wake generator (entropy).

The precise location of the separation point is determined by the zero value of the skin friction coefficient $c_{f,s}$, see Eq. (2.12). Fig. 6.16 shows the space-time diagram of $c_{f,s}$ along the curvilinear length of the blade. The periodic passage of the wake is clearly visible on the suction side. This space-time diagram can be compared with the ones shown in Fig. 2.12. The present case corresponds to the one with the attached flow case. As described in [9], there is a succession of calmed and disturbed regions. The wake passage is beneficial when without wake, there is a large separation bubble on the suction side. Then, with the wake passage, the calmed region outweighs the detrimental effect of the disturbed regions.

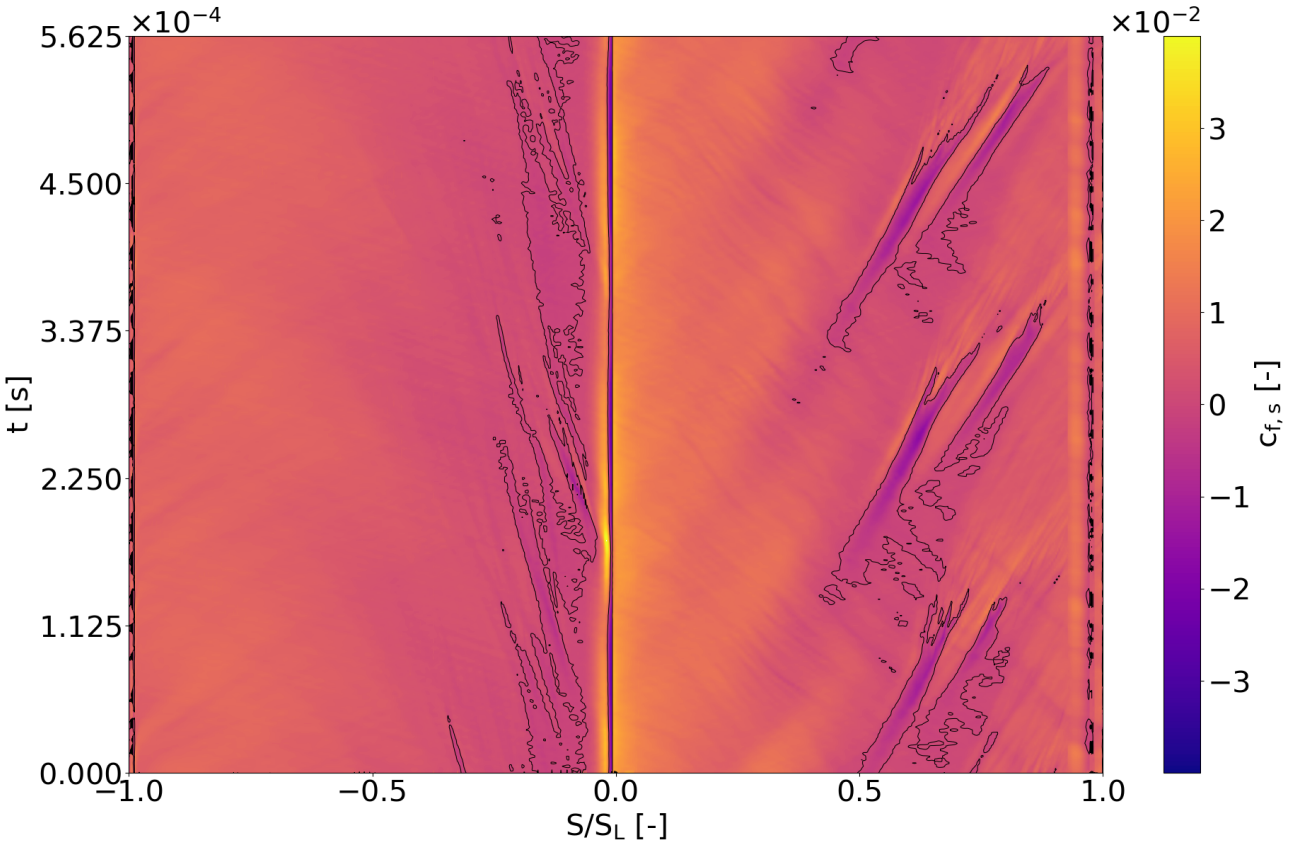

Figure 6.16: Space-time diagram of the span-averaged skin friction coefficient. The black lines are located at $c_{f,s} = 0$. The x-axis denotes the curvilinear length S of the blade normalized by the total length S_L. By convention the PS is on the left and the SS on the right, with the LE in the middle.

In Fig. 6.17 the momentum diffusive fluxes on the blade surface are shown with the entropy in the background. In blue, the regions where the flow is separating from the blade surface. As the wake passes, it interacts with the blade boundary layer as depicted in Fig. 2.11b.

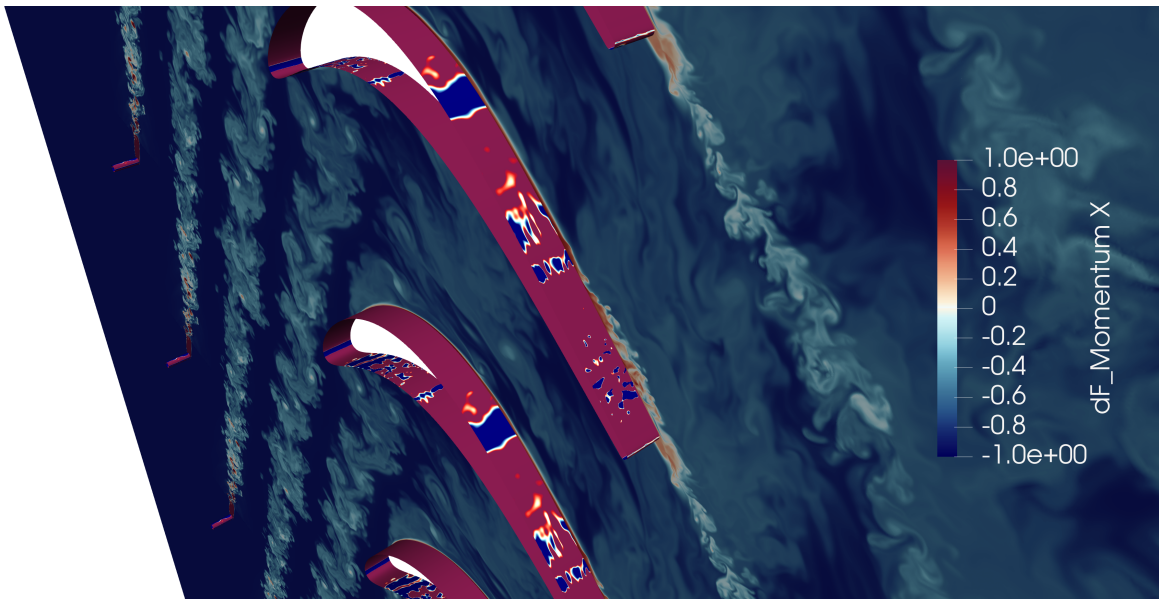

(a) Global time t = 9.4e-4s, time in Fig. 6.16: t = 0s.

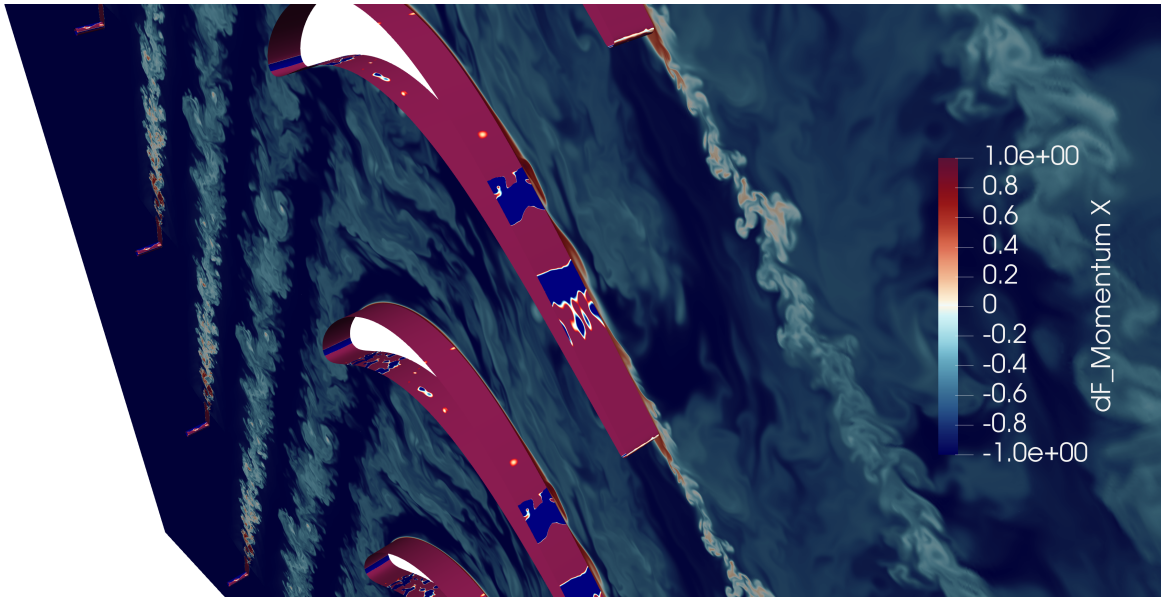

(b) Global time t = 1.22e-3s, time in Fig. 6.16: t = 2.8e-4s.

Figure 6.17: Instantaneous momentum diffusive flux in the x direction on the blade surface with entropy on the plane located at z = 0. Two different instants are shown. The global time corresponds to the time from the start of the coupling of the two domains. The other time is shown to situate the picture at the given time in Fig. 6.16.

6.2.2 Blade wake

Fig. 6.18 shows the comparison between the blade wake with and without wake generator. The blade wake with wake generator is more turbulent and narrower than the other one.

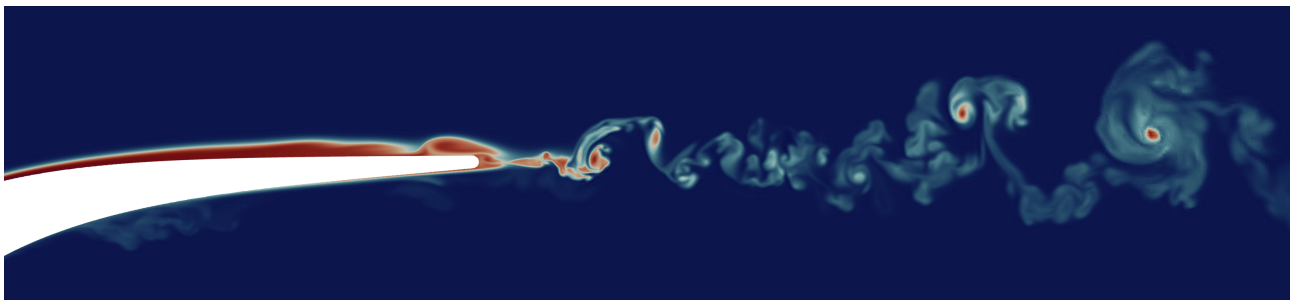

(a) Without wake generator.

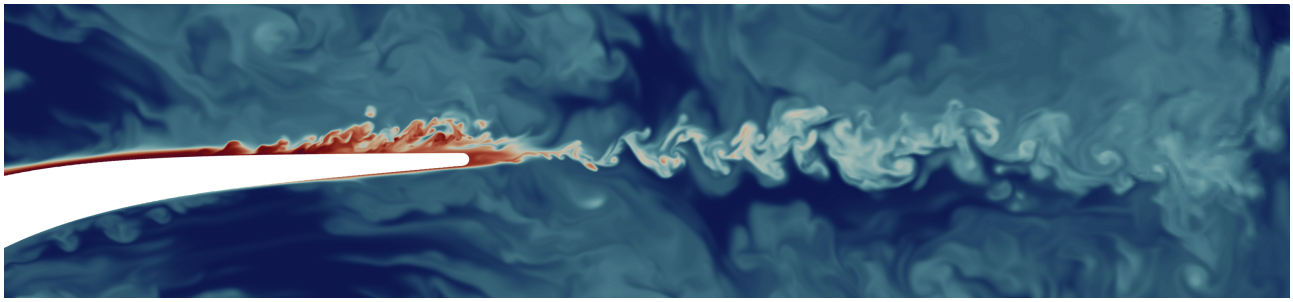

(b) With wake generator.

Figure 6.18: Comparison of the blade wake with and without wake generator.

6.3 Comparison with the CERFACS simulation

In the conference paper of 2023 January from Dombard [16], a similar simulation of rotor/stator interaction has been performed with the CERFACS using LES with a wall-adapting local eddy viscosity (WALE) sub-grid scale model.
The CERFACS uses 322M DOFs for the two domains coupled where 253M DOFs are used in the present work. However, the computational domain of the CERFACS takes two turbine passages instead of one. Moreover, the span-wise dimension is 2 pitches, which is 18 times wider than the span used in the present work (7% chord). That means that the computational domain of the CERFACS simulation is 36 times bigger with 322M DOFs. Thus, for the same size of computational domain, the CERFACS simulation uses about 9M DOFs where the present work uses 253M DOFs.
Also, in the present work, the mesh has been refined only in the regions of interest ie, in the vicinity of the cylinder and blade surfaces and the shock and wakes regions whereas no information is given about the mesh refinement procedure in CERFACS simulation.
So, the present solution is able to capture much more flow details, with the capture of a Nyquist scale 28 times smaller than for the CERFACS simulation. On the other hand, most of the increase of DOFs for the present simulation has been driven by the solver inability to manage the shock, what the CERFACS was able to do with much less DOFs per unit volume and no local mesh refinement adaptation.

6.4 Blade-like wake

As introduced in section 3.3.1, the hypothesis of reproducing a blade wake using a rotating bar is validated by multiple studies at low RPM [49], [50], [11]. In the present case however, the wakes are completely different as shown in Fig. 6.19. It results from the strong acceleration of the flow around the fast moving cylinder leading to a shock interacting with the wake.
In further DGM simulations, the use of a complete blade as wake generator instead of a cylinder should be explored. In fact, this idea has been applied by Greschner and Thiele [61] at M = 0.2. It is of course more challenging to use a real blade as wake generator in an experimental campaign where 3300 RPM must be reached.

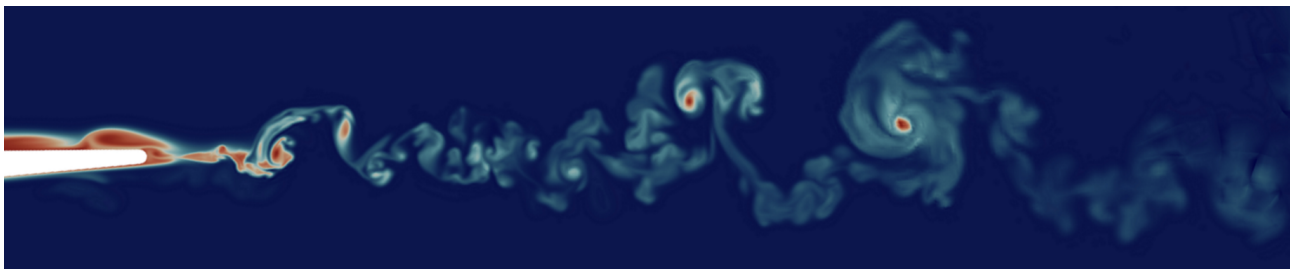

(a) Blade wake.

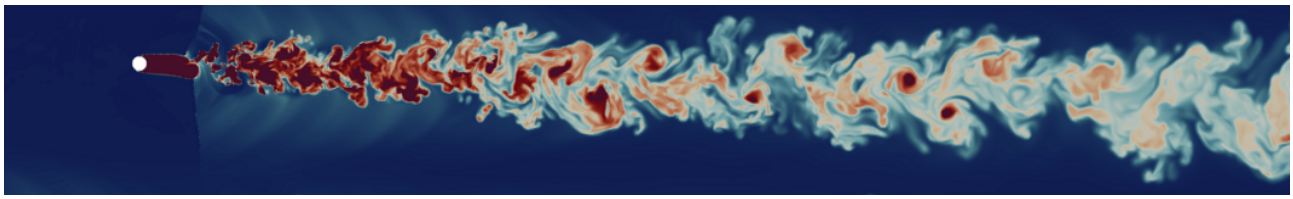

(b) Translating bar wake.

Figure 6.19: Comparison of the entropy generated in the wakes of the translating bar and the blade.

7 Conclusion

The main objective of this thesis was to show that the current version of ArgoDG is able to perform this kind of simulation combining the following properties:

- One static and one translating domains interacting through non matching connection.
- A highly refined mesh of 4M elements.
- A moving shock interacting with the cylinder wake, with and without a shock capturing method (AV).
- A strong transition from p0 to p3.
- A coupling of two domains whose solutions are initialized separately.

The second aspect of this thesis concerns the highlighting of some bugs encountered during the simulation and small improvements of the current software:

- Domain specification missing for the sponge layer and AV box (and Riemann solver).
- Explicit storage of the global time of the simulation for easier restart synchronization.
- A bug in the translation of the solution at the restart.
- A bug in the definition of the probes along a specified axis taking into account periodic boundary conditions defined in the opposite direction (already fixed).
- A bug in the application of the sponge layer slicing average at solution restart.

Additional aspects provided:

- Highlight of the differences between the wake generated by the rotating bars and the blade one suggesting an adjustment in the wake generator setup.
- Highlight of the motion of a shock attached to the wake of a cylinder.
- Quantitative analysis of the wake generator and qualitative analysis of the wake interaction with the blade boundary layer.
- Movies showing the time evolution of the flow.

Future aspects and improvements:

- Increase the span-wise distance of the computational domain to ensure zero spatial correlations at the span center.
- Time average during multiple convective times of the simulation with the wake generator alone.
- Deeper analysis of the shock behind the translating cylinder.
- Phase-time averages of the simulation on multiple convective times to obtain more quantitative results for the two domains coupled.
- Simulation of a moving blade instead of a moving bar for a more accurate wake generation. May be cheaper in term of computational cost as the shock may be softer requiring a less refined shock region.
- Other Mach numbers such as 0.9 and 0.95 could be tested.

Nomenclature

Acronyms

AMR Adaptative mesh refinement

API Application Programmer Interface

AV Artificial viscosity

BDF Backward differentiation formula

CERFACS Centre européen de recherche et de formation avancée en calcul scientifique

CPU Central Processing Unit

DGM Discontinuous Galerkin method

DOF Degree of freedom

FVM Finite volume method

GMRES Generalized minimal residual

JRN Jacobian recycling number

LE Leading edge

LPT Low pressure turbine

MPI Message Passing Interface

NSE Navier-Stokes equations

ROI Region of interest

RPM Rotations per minute

SLB Blade cascade inlet sponge layer

SLIN Inlet sponge layer

SLW Wake generator outlet sponge layer

$SPLEEN$ Secondary and Leakage flow effects in high-speed Low prEssurE turbiNes

TE Trailing edge

TG Turbulence grid

VKI Von Karman Institute

WG Wake generator

ZSL Z-shaped sponge layer

Physical quantities

α Inlet flow angle

$\beta_{\mathrm{m,in}}$ Inlet angle

$\beta_{\mathrm{m,out}}$ Outlet angle

Ω Rotating velocity

ζ Stagger angle

C AV smoothness

c True chord

c_{ax} Axial chord

g Pitch

H Span

k AV amplitude

M Mach number

o Throat opening

$p_{0,\mathrm{in}}$ Inlet total pressure

p_{out} Outlet static pressure

Ra Maximum roughness

Re Reynolds number

s_0 AV activation threshold

Str Strouhal number

t time

$T_{0,\mathrm{in}}$ Inlet total temperature

v_b Peripheral velocity

Bibliography

[1] J. Kurzke, "Fundamental differences between conventional and geared turbofans," Jan. 2009. DOI: 10.1115/GT2009-59745.

[2] A. America. (), [Online]. Available: https://aerospaceamerica.aiaa.org/features/high-gear/. (accessed: 11.08.2024).

[3] G. .-. G. Aviation. (), [Online]. Available: https://www.aerocontact.com/salon-aeronautique-virtuel/produit/550-moteur-ge9x. (accessed: 11.08.2024).

[4] E. M. Curtis, H. P. Hodson, M. R. Banieghbal, J. D. Denton, R. J. Howell, and N. W. Harvey, "Development of Blade Profiles for Low-Pressure Turbine Applications," *Journal of Turbomachinery*, vol. 119, no. 3, pp. 531–538, Jul. 1997, ISSN: 0889-504X. DOI: 10.1115/1.2841154. eprint: https://asmedigitalcollection.asme.org/turbomachinery/article-pdf/119/3/531/5631690/531_1.pdf. [Online]. Available: https://doi.org/10.1115/1.2841154.

[5] P. Stadtmüller, L. Fottner, and A. Fiala, "Experimental and numerical investigation of wake-induced transition on a highly loaded lp turbine at low reynolds numbers," May 2000. DOI: 10.1115/2000-GT-0269.

[6] X. QU, Y. ZHANG, X. LU, and J. ZHU, "Unsteady experimental and numerical investigation of aerodynamic performance in ultra-high-lift lpt," *Chinese Journal of Aeronautics*, vol. 33, no. 5, pp. 1421–1432, 2020, ISSN: 1000-9361. DOI: https://doi.org/10.1016/j.cja.2019.12.013. [Online]. Available: https://www.sciencedirect.com/science/article/pii/S1000936120300339.

[7] H. P. Hodson and W. N. Dawes, "On the Interpretation of Measured Profile Losses in Unsteady Wake-Turbine Blade Interaction Studies," *Journal of Turbomachinery*, vol. 120, no. 2, pp. 276–284, Apr. 1998, ISSN: 0889-504X. DOI: 10.1115/1.2841403. eprint: https://asmedigitalcollection.asme.org/turbomachinery/article-pdf/120/2/276/5840570/276_1.pdf. [Online]. Available: https://doi.org/10.1115/1.2841403.

[8] H. P. Hodson and R. G. Dominy, "The Off-Design Performance of a Low-Pressure Turbine Cascade," *Journal of Turbomachinery*, vol. 109, no. 2, pp. 201–209, Apr. 1987, ISSN: 0889-504X. DOI: 10.1115/1.3262086. eprint: https://asmedigitalcollection.asme.org/turbomachinery/article-pdf/109/2/201/5838947/201_1.pdf. [Online]. Available: https://doi.org/10.1115/1.3262086.

[9] H. P. Hodson and R. J. Howell, "The role of transition in high-lift low-pressure turbines for aeroengines," *Progress in Aerospace Sciences*, vol. 41, no. 6, pp. 419–454, 2005, ISSN: 0376-0421. DOI: https://doi.org/10.1016/j.paerosci.2005.08.001. [Online]. Available: https://www.sciencedirect.com/science/article/pii/S0376042105000825.

[10] H. P. Hodson and R. J. Howell, "Bladerow interactions, transition, and high-lift aerofoils in low-pressure turbines," *Annual Review of Fluid Mechanics*, vol. 37, no. Volume 37, 2005, pp. 71–98, 2005, ISSN: 1545-4479. DOI: https://doi.org/10.1146/annurev.fluid.37.061903.175511. [Online]. Available: https://www.annualreviews.org/content/journals/10.1146/annurev.fluid.37.061903.175511.

[11] X. Li, X. Fang, L. Cai, *et al.*, "Incidence adaptation to the influence of wake sweeps on the aerodynamic performance of a low-pressure turbine cascade," *Aerospace*, vol. 11, no. 7, 2024, ISSN: 2226-4310. DOI: 10.3390/aerospace11070569. [Online]. Available: https://www.mdpi.com/2226-4310/11/7/569.

[12] L. Simonassi, G. Lopes, and S. Lavagnoli, "Effects of periodic incoming wakes on the aerodynamics of a high-speed low-pressure turbine cascade," *International Journal of Turbomachinery, Propulsion and Power*, vol. 8, no. 3, 2023, ISSN: 2504-186X. DOI: 10.3390/ijtpp8030035. [Online]. Available: https://www.mdpi.com/2504-186X/8/3/35.

[13] *Numerical Simulation of a Highly Loaded LPT Cascade With Strong Suction Side Separation Under Periodically Unsteady Inflow Conditions*, vol. Volume 7: Turbomachinery, Parts A, B, and C, Turbo Expo: Power for Land, Sea, and Air, Jun. 2010, pp. 1163–1175. DOI: 10.1115/GT2010-22363. eprint: https://asmedigitalcollection.asme.org/GT/proceedings-pdf/GT2010/44021/1163/4718489/1163_1.pdf. [Online]. Available: https://doi.org/10.1115/GT2010-22363.

[14] W. Zhang and Z. Zou, "Large eddy simulations of periodic wake effects on boundary-layer transition of low-pressure turbine cascades," *AIP Advances*, vol. 13, no. 2, p. 025 128, Feb. 2023, ISSN: 2158-3226. DOI: 10.1063/5.0139787. eprint: https://pubs.aip.org/aip/adv/article-pdf/doi/10.1063/5.0139787/16755480/025128_1_online.pdf. [Online]. Available: https://doi.org/10.1063/5.0139787.

[15] V. Michelassi, J. G. Wissink, J. Frohlich, and W. Rodi, "Large-eddy simulation of flow around low-pressure turbine blade with incoming wakes," *AIAA Journal*, vol. 41, no. 11, pp. 2143–2156, 2003. DOI: 10.2514/2.6832. eprint: https://doi.org/10.2514/2.6832. [Online]. Available: https://doi.org/10.2514/2.6832.

[16] A. Boudin, J. Dombard, F. Duchaine, *et al.*, "Analysis of rotor/stator interactions in a high-speed low-pressure turbine cascade using large-eddy simulations.," Jan. 2023. DOI: 10.29008/ETC2023-257.

[17] A. Cassinelli, A. Mateo Gabín, F. Montomoli, P. Adami, R. Vázquez Díaz, and S. J. Sherwin, "Reynolds sensitivity of the wake passing effect on a lpt cascade using spectral/hp element methods," *International Journal of Turbomachinery, Propulsion and Power*, vol. 7, no. 1, 2022, ISSN: 2504-186X. DOI: 10.3390/ijtpp7010008. [Online]. Available: https://www.mdpi.com/2504-186X/7/1/8.

[18] M. Borbouse, "Boundary layer stability and shock interactions in a high-speed low pressure turbine cascade," Master's Thesis, University of Liège, 2023.

[19] S. Lavagnoli, G. Lopes, L. Simonassi, and A. F. M. Torre, *SPLEEN - High Speed Turbine Cascade – Test Case Database*, version v2, Zenodo, Nov. 2022. DOI: 10.5281/zenodo.7359401. [Online]. Available: https://doi.org/10.5281/zenodo.7359401.

[20] M. M. V., "Transition in open flow systems-a reassessment," *Bull. Am. Phys. Soc.*, vol. 39, p. 1882, 1994. [Online]. Available: https://cir.nii.ac.jp/crid/1573950400137520256.

[21] D. E., *Lecture notes in fluid mechanics*, 2020.

[22] H. K., *Lecture notes in design of turbomachines*, Nov. 2023.

[23] B. Bhandari and P. Yadav, *Cfd analysis of steady, inviscid flow in a converging-diverging (cd) nozzle*, Jun. 2020.

[24] C. Reynolds. "Astrophysical fluid dynamics, lecture 9 : Shocks." (), [Online]. Available: https://people.ast.cam.ac.uk/~vasily/Lectures/AFD_2021_Reynolds/AFDLecture09_10Feb2021.pdf. (accessed: 16.05.2024).

[25] M. L. Norman and K.-H. A. Winckler, "Supersonic jets," *Los Alamos Science*, vol. 12, no. 43, 1985. [Online]. Available: https://la-science.lanl.gov/lascience12.shtml.

[26] R. Groningen. "Chapter 7 shocks." (), [Online]. Available: https://www.astro.rug.nl/~weygaert/tim1publication/astrohydro2014/achterberg.ngsa.shockwaves.pdf. (accessed: 16.05.2024).

[27] T. U. of Texas at Austin. "Sound waves." (), [Online]. Available: https://farside.ph.utexas.edu/teaching/336L/Fluidhtml/node195.html. (accessed: 16.05.2024).

[28] NASA. "Normal shock waves." (), [Online]. Available: https://www.grc.nasa.gov/WWW/BGH/normal.html. (accessed: 16.05.2024).

[29] NPTEL. “Compressible flow: Normal shocks.” (), [Online]. Available: https://archive.nptel.ac.in/content/storage2/courses/112104118/lecture-41/41_1_normal_shocks.htm. (accessed: 16.05.2024).

[30] T. U. of Texas at Austin. “Normal shocks.” (), [Online]. Available: https://farside.ph.utexas.edu/teaching/336L/Fluidhtml/node199.html#s14.8. (accessed: 16.05.2024).

[31] Y. Modarres-Sadeghi, “Flow around a fixed cylinder,” in *Introduction to Fluid-Structure Interactions*. Cham: Springer International Publishing, 2021, pp. 5–22, ISBN: 978-3-030-85884-1. DOI: 10.1007/978-3-030-85884-1_2. [Online]. Available: https://doi.org/10.1007/978-3-030-85884-1_2.

[32] J. Hoffmann and D. A. Weiss, “Compressible and viscous effects in transonic planar flow around a circular cylinder—a numerical analysis based on a commercially available cfd tool,” *Fluids*, vol. 8, no. 6, 2023, ISSN: 2311-5521. DOI: 10.3390/fluids8060182. [Online]. Available: https://www.mdpi.com/2311-5521/8/6/182.

[33] J. D. Denton, “The 1993 IGTI Scholar Lecture: Loss Mechanisms in Turbomachines,” *Journal of Turbomachinery*, vol. 115, no. 4, pp. 621–656, Oct. 1993, ISSN: 0889-504X. DOI: 10.1115/1.2929299. eprint: https://asmedigitalcollection.asme.org/turbomachinery/article-pdf/115/4/621/5551769/621_1.pdf. [Online]. Available: https://doi.org/10.1115/1.2929299.

[34] J. Hourmouziadis, “Aerodynamic design of low pressure turbines,” in *Blading Design for Axial Turbomachines, AGARD Lecture Series*, vol. LS-167, ; 1989, pp. 8–40. [Online]. Available: https://www.tib.eu/de/suchen/id/tema%3ATEMAM89113529370.

[35] *The Transition Mechanism of Highly-Loaded LP Turbine Blades*, vol. Volume 5: Turbo Expo 2003, Parts A and B, Turbo Expo: Power for Land, Sea, and Air, Jun. 2003, pp. 779–788. DOI: 10.1115/GT2003-38304. eprint: https://asmedigitalcollection.asme.org/GT/proceedings-pdf/GT2003/36886/779/2590124/779_1.pdf. [Online]. Available: https://doi.org/10.1115/GT2003-38304.

[36] R. D. Stieger, “The effects of wakes on separating boundary layers in low pressure turbines,” Available at http://www-g.eng.cam.ac.uk/whittle/T106/T106A_cascade/T106A_cascade_publications/RStieger_PhD.pdf, PhD thesis, Cambridge University Engineering Department, Cambridge, Feb. 2002.

[37] K. Hillewaert, “Development of the discontinuous galerkin method for high-resolution, large scale cfd and acoustics in industrial geometries,” Ph.D. dissertation, Feb. 2013.

[38] A. M. Fernando and F. Q. Hu, “Dgm-fd: A finite difference scheme based on the discontinuous galerkin method applied to wave propagation,” *Journal of Computational Physics*, vol. 230, no. 12, pp. 4871–4898, 2011, ISSN: 0021-9991. DOI: https://doi.org/10.1016/j.jcp.2011.03.008. [Online]. Available: https://www.sciencedirect.com/science/article/pii/S0021999111001513.

[39] D. I. Ketcheson, R. J. LeVeque, and M. J. del Razo, *Riemann Problems and Jupyter Solutions*. Philadelphia, PA: Society for Industrial and Applied Mathematics, 2020. DOI: 10.1137/1.9781611976212. eprint: https://epubs.siam.org/doi/pdf/10.1137/1.9781611976212. [Online]. Available: https://epubs.siam.org/doi/abs/10.1137/1.9781611976212.

[40] X.-S. Li, X.-D. Ren, C.-W. Gu, and Y.-H. Li, “Shock-stable roe scheme combining entropy fix and rotated riemann solver,” *AIAA Journal*, vol. 58, no. 2, pp. 779–786, 2020. DOI: 10.2514/1.J058549. eprint: https://doi.org/10.2514/1.J058549. [Online]. Available: https://doi.org/10.2514/1.J058549.

[41] P. Roe, “The use of riemann problem in finite difference schemes,” in Jan. 2006, vol. 141, pp. 354–359, ISBN: 978-3-540-10694-4. DOI: 10.1007/3-540-10694-4_54.

[42] J.-M. Moschetta and J. Gressier, “A cure for the sonic point glitch,” *International Journal of Computational Fluid Dynamics*, vol. 13, Jan. 2000. DOI: 10.1080/10618560008940895.

[43] E. Süli and D. F. Mayers, *An Introduction to Numerical Analysis*. Cambridge University Press, 2003.

[44] Y. Saad and M. H. Schultz, “Gmres: A generalized minimal residual algorithm for solving nonsymmetric linear systems,” *SIAM Journal on Scientific and Statistical Computing*, vol. 7, no. 3, pp. 856–869, 1986. DOI: 10.1137/0907058. eprint: https://doi.org/10.1137/0907058. [Online]. Available: https://doi.org/10.1137/0907058.

[45] M. J. Zahr and P.-O. Persson, "Performance tuning of newton-gmres methods for discontinuous galerkin discretizations of the navier-stokes equations," in *21st AIAA Computational Fluid Dynamics Conference*. DOI: 10.2514/6.2013-2685. eprint: https://arc.aiaa.org/doi/pdf/10.2514/6.2013-2685. [Online]. Available: https://arc.aiaa.org/doi/abs/10.2514/6.2013-2685.

[46] R. S. Tuminaro, H. F. Walker, and J. N. Shadid, "On backtracking failure in newton–gmres methods with a demonstration for the navier–stokes equations," *Journal of Computational Physics*, vol. 180, no. 2, pp. 549–558, 2002, ISSN: 0021-9991. DOI: https://doi.org/10.1006/jcph.2002.7102. [Online]. Available: https://www.sciencedirect.com/science/article/pii/S0021999102971020.

[47] S. Lavagnoli, G. Lopes, L. Simonassi, and A. F. M. Torre, *SPLEEN - High Speed Turbine Cascade – Test Case Database*, version v3, Zenodo, Jun. 2023. DOI: 10.5281/zenodo.8075795. [Online]. Available: https://doi.org/10.5281/zenodo.8075795.

[48] S. Lavagnoli, G. Lopes, L. Simonassi, and A. F. M. Torre, *SPLEEN - High Speed Turbine Cascade – Test Case Database*, version v1, Zenodo, Oct. 2022. DOI: 10.5281/zenodo.7264762. [Online]. Available: https://doi.org/10.5281/zenodo.7264762.

[49] H. Pfeil and J. Eifler, "Turbulence characteristics behind rotating cylinder grids," *Forschung im Ingenieurwesen*, vol. 42, no. 1, pp. 27–32, Jan. 1976.

[50] V. Schulte and H. P. Hodson, "Unsteady Wake-Induced Boundary Layer Transition in High Lift LP Turbines," *Journal of Turbomachinery*, vol. 120, no. 1, pp. 28–35, Jan. 1998, ISSN: 0889-504X. DOI: 10.1115/1.2841384. eprint: https://asmedigitalcollection.asme.org/turbomachinery/article-pdf/120/1/28/5658266/28_1.pdf. [Online]. Available: https://doi.org/10.1115/1.2841384.

[51] L. Simonassi, G. F. Do Carmo Lopes, S. Gendebien, *et al.*, "An experimental test case for transonic low-pressure turbines - part i: Rig design, instrumentation and experimental methodology," English, in *Turbomachinery - Axial Flow Turbine Aerodynamics; Deposition, Erosion, Fouling, and Icing; Radial Turbomachinery Aerodynamics*, IGTI - International Gas Turbine Institute [GE], Rotterdam, Nld: American Society of Mechanical Engineers (ASME), 2022. DOI: 10.1115/GT2022-81566. [Online]. Available: https://asmedigitalcollection.asme.org/GT/proceedings-pdf/doi/10.1115/GT2022-81566/6936909/v10bt30a012-gt2022-81566.pdf.

[52] C. Geuzaine and J.-F. Remacle. (), [Online]. Available: https://gmsh.info/. (accessed: 2.07.2024).

[53] A. E. Mattsson and W. J. Rider, "Artificial viscosity: Back to basics.," Aug. 2013. [Online]. Available: https://www.osti.gov/biblio/1115027.

[54] P.-O. Persson and J. Peraire, "Sub-cell shock capturing for discontinuous galerkin methods," *AIAA paper*, vol. 2, Jan. 2006. DOI: 10.2514/6.2006-112.

[55] G. Barter and D. Darmofal, "Shock capturing with higher-order, pde-based artificial viscosity," *Collection of Technical Papers - 18th AIAA Computational Fluid Dynamics Conference*, vol. 1, Jun. 2007. DOI: 10.2514/6.2007-3823.

[56] E. Laughton, G. Tabor, and D. Moxey, "A comparison of interpolation techniques for non-conformal high-order discontinuous galerkin methods," *Computer Methods in Applied Mechanics and Engineering*, vol. 381, p. 113820, 2021, ISSN: 0045-7825. DOI: https://doi.org/10.1016/j.cma.2021.113820. [Online]. Available: https://www.sciencedirect.com/science/article/pii/S0045782521001560.

[57] CECI. (), [Online]. Available: https://www.ceci-hpc.be/clusters.html#lucia. (accessed: 16.05.2024).

[58] Paraview. (), [Online]. Available: https://docs.paraview.org/en/latest/index.html. (accessed: 15.08.2024).

[59] R. B. Miserda and R. Leal, "Numerical simulation of the unsteady aerodynamic forces over a circular cylinder in transonic flow," in *44th AIAA Aerospace Sciences Meeting and Exhibit*. DOI: 10.2514/6.2006-1408. eprint: https://arc.aiaa.org/doi/pdf/10.2514/6.2006-1408. [Online]. Available: https://arc.aiaa.org/doi/abs/10.2514/6.2006-1408.

[60] C. P. Kentzer, "Transonic flows past a circular cylinder," *Journal of Computational Physics*, vol. 6, no. 2, pp. 168–182, 1970, ISSN: 0021-9991. DOI: https://doi.org/10.1016/0021-9991(70)90019-7. [Online]. Available: https://www.sciencedirect.com/science/article/pii/0021999170900197.

[61] B. Greschner and F. Thiele, "Broadband noise analysis of a rotor-stator-cascade using wall modeled les simulation," in *18th AIAA/CEAS Aeroacoustics Conference (33rd AIAA Aeroacoustics Conference)*. DOI: 10.2514/6.2012-2308. eprint: https://arc.aiaa.org/doi/pdf/10.2514/6.2012-2308. [Online]. Available: https://arc.aiaa.org/doi/abs/10.2514/6.2012-2308.